FLEXIBLE MICROELECTRONICS FOR PREVENTING AND MANAGING VISION LOSS

By

Mohammad Hossein Mazaheri Kouhani

A DISSERTATION

Submitted to
Michigan State University
in partial fulfillment of the requirements
for the degree of

Electrical Engineering— Doctor of Philosophy

2020

ABSTRACT

FLEXIBLE MICROELECTRONICS FOR
PREVENTING AND MANAGING VISION LOSS

By

Mohammad Hossein Mazaheri Kouhani

In this thesis, we investigate and develop three flexible microelectronic technologies for managing glaucoma, slowing down neural degeneration and improving the delivery of bionic vision using visual prosthetic technologies. The first device focuses on monitoring intraocular pressure as a risk factor that is commonly known to induce blindness in glaucoma patients. The second device is designed and built to further facilitate the investigation of the hypothesis whether stimulating visual cortex with light slows down the degeneration of optic nerve pathways in the visual circuitry in the brains of animals and eventually be able to optimize the parameters and maximize the positive effects shown in earlier studies. The third project reports a successful attempt in improving a currently existing visual prosthetic implantable device made by a company called Second Sight Medical Products Inc. For the first project, we create a contact lens that incorporates a pressure sensor and sends out continuous data on the pressure of the eyes to external devices through a pair of goggles that communicates with the lens on the surface of the patient's eye. The second part of the thesis focuses on the development of a device that helps with investigating the effect of optogenetic stimulation on slowing down the degenerative processes in neural pathways that lead to loss of retinal cells and eventually blindness. Thirdly, we develop a new coating technology for the currently existing microelectrodes that some versions of them are currently commercially available for the

delivery of bionic vision directly through a flexible microelectrode array implanted on the visual cortex of humans. These three technologies described, developed and advanced in this thesis allow a multi-factorial approach to preventing vision loss and managing blindness caused by multitude of reasons including but not limited to glaucoma, macular degeneration, and retinitis pigmentosa. While the wearable contact lens can help monitoring the pressure in the eye round-the-clock, the cortical prosthetic devices using either light or electricity stimulate the visual cortex that can either slow down vision loss or reintroduce a new sensory domain called bionic vision for blind patients. We demonstrate proof of concept for the wearable pressure sensing contact lens by demonstrating the responsivity in *ex vivo* experiments on enucleated animal eyes and the eyes intact in post-mortem dog and rabbit heads. Next we show proof of concept for a wireless and miniaturized optogenetic stimulator device designed for experiments on mice. These micro-controlled light delivery systems are compact and low-cost allowing future experiments in vivo that can further demonstrate the efficacy of light delivery in battling and slowing down or perhaps stop vison loss caused by various degenerative and progressive neural diseases. Last but not the least, we advance a commercially existing visual prosthetic system and develop and incorporate new coating material for its electrical stimulation electrodes so that it can better deliver bionic vision to those patients who have already lost their vision.

This thesis is dedicated to Mom and Dad.
Thank you for always believing in me.

ACKNOWLEDGEMENTS

First and foremost, I would like to acknowledge and express appreciation for the supportive mentorship of Dr. Wen Li. Her technical guidance, generous advisory, and kind supervision not only directed me to continuously optimize my graduate experience but also lifted me up in multiple unforeseen challenges along the way and helped me grow stronger and wiser as a person as much as I developed professional expertise and leadership skills.

Secondly, I would want to offer my gratitude to my committee members: Dr. Arthur Weber, Dr. Premjeet Chahal and Dr. Mi Zhang for their support and suggestions during the progress of my PhD projects. In addition, I owe special thanks to Dr. Tim Hogan whom his excellent teaching at Cleanroom Procedures took my skill-set to a significantly higher level which helped me a lot with related technical skills.

Thirdly, I would like to express my utmost appreciation to Dr. Proyag Datta and Dr. Nick Talbot and Alexander Istomin for their mentorship, guidance, and support during my unforgettable internship program at Second Sight Medical Products Inc.

My sincere thanks also go to my colleagues at Microtechnology Lab: Dr. Wasif Khan, Dr. Xiaopeng Bi, Dr. Bin Fan, Yue Guo, Weiyang Yang and Yan Gong. I would also want to acknowledge other independent researchers Rui Luo, Jiajia Wu, Ryan Aridi, Hanaan Hayat,

Sina Parsnejad and Arman Tavakoli for their help, support, and contributions along the way. I would also love to thank our dear colleagues at Michigan State University, especially Dr. Baokang Bi from Keck Microfabrication Facility and Mr. Brian Wright from ECE shop for their suggestions, trainings, and kind help.

I have also received numerous guidance and support, both in technical and emotional support from my friends in and out of campus. Especially my dear friends and colleagues in the institute of quantitative sciences (IQ) at MSU with whom I worked along for three years and enjoyed the vibrant culture at this remarkable institution.

Finally, and most importantly, I would like to thank my family for always being there for me and encouraging me to pursue my passion and offering their support when I needed most.

TABLE OF CONTENTS

LIST OF TABLES

LIST OF FIGURES

CHAPTER 1

Vision Loss and Strategies in Management and Treatment

1.1 Vision

Vision is the most critical human sensory domain in creating the perception of the world. According to a national survey of 2,044 U.S. residents in 2016, most Americans across all ethnic and racial groups describe losing eyesight as having the greatest impact on their quality of life when compared against other outcomes such as loss of limb, memory, hearing or speech [1]. Among all eye diseases, glaucoma is the second leading cause of blindness worldwide and is expected to cause 11.2 million cases of irreversible blindness globally by 2020 [2]. It is a multifactorial and complex eye disease that is strongly associated with elevated intraocular pressure (IOP).

A major report published by World Health Organization (WHO) in 2017 estimates 253 million people live with vision impairment: 36 million are blind and 217 million have moderate to severe vision impairment. Ninety percent of those who are blind live in developing countries. [3] Visual impairment includes both low vision and blindness. Low vision is defined as visual acuity less than 20/60 but equal to or better than 20/60 in the better eye with the best possible correction, and blindness is defined as visual acuity less than 20/400 or a corresponding visual field of less than 20 degrees from the point of fixation in the better eye with the best possible correction. [4] Loss of vision disables the person to

read, identify their loved ones and reliably perform everyday activities like walking down the street, getting in and out of office, or reaching for a glass of water.

1.1.1 Glaucoma

The task of delivering nutrition and clearing off the byproducts of cell metabolism is carried out by an agent called aqueous humor. This aqueous humor is secreted by ciliary body in the eye, and its pathway begins from passing through the posterior chamber and flowing to the pupil circulating around the anterior chamber. This flow of humor enriches the cells of the avascular lens, corneal and trabecular mesh and eventually finds its way out through the collector channel. The outflow of the aqueous humor also occurs directly through the scleral tissue which is called uveoscleral outflow. Lymphatic vessels in the eye also play important indirect roles in the dynamics of aqueous humor.

Normal eye pressure ranges from 12-22 mmHg and beyond that range is considered ocular hypertension. High pressure alone does not cause glaucoma, however, it is the only significant risk factor that is modifiable to date [7]. Evidence shows that IOP reduction slows the onset and progression of glaucomatous damage in eyes with primary open angle glaucoma [8]. The pressure builds up due to an imbalance between inflow and outflow of aqueous humor in the anterior chamber of the eye.

The outflow of aqueous humor is mostly pressure dependent. Though, this dependency varies between the two main pathways of drainage. The trabecular meshwork is the sole pressure-dependent pathway when the IOP pressure is somewhere in the window of 10-35 mmHg. The trabecular pressure dependency within this range is quantified from 0.1 to 0.5 μL/min/mmHg. Within this normal pressure-window the uveoscleral outflow is surprisingly constant. However, when the pressure elevates above the 60mmHg or drops below 4mmHg the uveoscleral outflow significantly surges or descents, respectively [7].

The surge in IOP happens mainly due to increased resistance in the aqueous humor downstream pathways through trabecular meshwork. The cells in the extracellular trabecular matrix of the juxtacanalicular trabecular meshwork (JCT) and the inner walls of Schlemm's canal [8-9]. These cells acquire contractile myofibroblast phenotypes and their cytoskeleton and extracellular matrix undergo changes that stiffen their connective tissue. The exact source of these cellular changes are not known and the resistance remains present even after trabecular meshwork is removed. [10-11].

The other main outflow pathway of aqueous humor which is uveoscleral also undergoes changes that causes higher resistance. The strongest and main hypothesis in explaining this elevated resistance revolves around the limitations caused by ciliary muscles. Aging is the main factor that is shown correlated with the unwanted changes in the ciliary body [12-13]. These changes are mainly concern the physiological action of contraction and relaxation of

the ciliary muscle [14]. Table 1 shows some of the factors that contribute to the alterations in the uveoscleral outflow.

Table 1. Factors that contribute to alterations in uveoscleral outflow [5].

Uveoscleral outflow **decreases with**	Uveoscleral outflow **increases with**
Night	Prostaglandin analogs
Aging	Brimonidine – chronic effect
Ocular hypertension	Uncontrolled primary open-angle glaucoma
Exfoliation syndrome with normal IOP	Ocular inflammation
Exfoliation syndrome with high IOP	Cyclodialysis cleft

The Ocular Hypertension Treatment Study (OHTS) is a multicenter, forthcoming, randomized, and controlled clinical trial that studies more than 1800 research subjects, evaluating the safety and efficacy of medical treatment in preventing or delaying the onset of visual-field loss and/or optic nerve damage in patients with ocular hypertension who are at moderate risk for developing primary open-angle glaucoma (POAG). [15] Most of the patients who are studied have ocular hypertension but show no sign of optic nerve damage, but there are also those individuals with normal IOP who still suffer from optic nerve damage caused by glaucoma.

The OHTS presents that onset and progression of glaucoma is increased with higher levels of IOP and lower central corneal thickness (CCT). High pressure alone does not cause glaucoma; however, it is the only significant risk factor that is modifiable to date. [16] Other epidemiological studies and clinical trials have also shown that optimal control of IOP reduces the risk of optic nerve damage in the long term and slows down the disease

progression. [17-18] Therefore, lowering IOP in patients with ocular hypertension is the only intervention to date that is proven to decelerate the loss of vision caused by glaucoma.

A study funded by the National Eye Institute (NEI) have identified 133 genetic variants that predict with 75 percent accuracy an individual's risk for developing glaucoma which were also shown directly correlated with elevated IOP. [19] Thanks to this finding genetic tests could now identify high-risk individuals who would benefit from early interventions. "That level of accuracy is not perfect, but it's a significant improvement over our current ability to predict a person's risk for glaucoma," said the study's co-author Janey Wiggs, M.D., Ph.D., associate chief of ophthalmology clinical research at Massachusetts Eye and Ear, Boston.

In its early stages, glaucoma causes peripheral vision loss, which often progresses unnoticed. Knowing their genetic status, individuals at high-risk could have their eye pressure closely monitored and pressure-lowering therapies could be administered at the earliest stages of disease. "Substantial evidence shows that the earlier you treat people, the better they are going to do in terms of maintaining and preserving useful vision," Wiggs said. To identify the genetic variants, the researchers compared IOP readings and genotype data from 139,555 European participants. The data analysis revealed 133 genetic variants associated with the risk of elevated IOP among which 68 had not been previously linked to IOP. "Unexpectedly, we found an almost direct correlation between the magnitude of the genetic variants' effect on eye pressure and their effect on glaucoma risk. In other words,

IOP appears to be the overriding factor that determines whether someone develops glaucoma," Wiggs said. [19]

In America, it is estimated that the number of individuals with glaucoma will double from 3 million to 6 million by 2050. Glaucoma is ought to be ruled out as part of every regular eye examination, otherwise most of the glaucomatous patients remain unnoticed until some peripheral visions is already lost irreversibly. In America, today, fifty percent of affected individuals do not know they have glaucoma [20].

No precise and generic pathophysiology of elevated IOP in ocular hypertension is found yet. Particularly, in 10 percent to 33 percent of people with juvenile open angle glaucoma, myocilin gene mutations are detected [21] and determined to cause protein misfolding, clogging the trabecular meshwork cells and making them dysfunctional in their facility of aqueous humor outflow and eventually noticeable advancement of IOP. [22] Subsequently, IOP builds up due to an imbalance between inflow and outflow of aqueous humor in the anterior chamber of the eye.

There are two dominant theories in explaining the pathophysiological relationship between elevated IOP and optic nerve damage. One identifies the vascular dysfunction as the cause of ischemia to the optic nerve, and the other accounts the mechanical dysfunction via cribriform plate compression of the neuronal axons.

Roughly seventy to ninety percent of glaucomatous patients are open-angle glaucoma [23]. Differentiating open from closed angle glaucoma is essential from a therapeutic standpoint, because each form of the disease has unique management considerations and interventions.

1.1.2 Current strategies in managing glaucoma

Existing glaucoma management strategies do not typically employ wearable or implantable devices. They include annual surgeries in severe cases, gene therapy, and/or daily eye drops to decrease the production of the aqueous humor or enhance its drainage.

Usually the identification of a person with Glaucoma starts with a regular pressure reading in annual check-ups. Patients are not always lucky to feel pain or happen to have their IOP monitored on a regular annual eye test and become aware of their ocular hypertension. Most of the times patients do not notice their condition until they start to lose portions of their peripheral vision. It is very unfortunate that glaucoma is a silent illness that most of the times it does not show any sign until it has damaged a good amount of nerve cells in the back of the eye.

In clinical settings the gold standard for IOP measurement is Goldmann Applanation Tonometry (GAT). Tonometry in general is the procedure where a clinician measures the IOP of a patient. This is an evaluation for patients who are identified at risk for Glaucoma. The unit used in tonometry is usually millimeters of mercury (mmHg). In applanation

tonometry the IOP is interpreted from the force required to flatten (applanate) a constant area of the cornea based on the Imbert-Flick Law. [24] The Goldmann tonometer is the most widely used version of applanation tonometry. Because the probe contacts the cornea, an anesthetic, such as proxymetacaine, is dropped on to the surface of the eye.

Besides, there are multiple tonometry techniques that use other methods of IOP inference such as non-contact air-puff applanation, contour-matched piezoresistive sensor, or ballistic probes. They all offer various advantages and disadvantages relative to GAT, but none are as widely used. It is important to consider the effect of corneal thickness on tonometry measurements. Often, patients with thin corneas (less than 555 μm) show artificially low IOP readings. This is dangerous because if their actual IOP is higher than what their reading shows, they may be at risk for developing glaucoma and their doctor may not know that. Those patients with thicker corneas may show a higher reading of IOP than the true value of the pressure. This means their eye pressure is lower than thought, and a lower IOP means that risk for developing glaucoma is minimal. So, if they overconsume the prescribed drugs that they may not have needed as much to they are missing opportunities in reducing cost or might suffer from unnecessary side effects.

A pachymetry test is a simple, quick, and painless test to measure the thickness of cornea. With this information, the doctor can correct the IOP reading and conduct the right treatment for different individuals. The procedure takes about a minute to measure the corneal thickness on both eyes [25]. Pachymetry can be done using either ultrasonic or

optical methods. There are noncontact methods such as optical biometry or optical coherence tomography. There are also contact methods such as ultrasound and some other optical techniques such as confocal microscopy. Ultrasound methods are the most widely used method in modern times and optical methods were mostly used in earlier times.

There are also handheld devices for measuring IOP such as Tonopen® [26] which can be used for more frequent and portable measurements. They require temporary corneal anesthesia just like GAT, cost a few thousands of Dollars to purchase one and require trained professionals to perform the measurement.

One approach in managing Glaucoma is employing sensors to monitor the IOP and then control it either by enhancing the fluid drainage using micro shunts (stents) [27], or using eye drops that quickly reduce the production of the aqueous humor, therefore, decreasing its inflow, or in some cases also help reducing drainage.

Wearable or implantable IOP sensors can monitor eye pressure fluctuations throughout day and night and manage patients and their medications more precisely while they are in their routine schedule either at home or work. Patients can wear and remove a contact lens by themselves, use the reading glasses when they need to and attend to other life activities while the measurements are being done.

Depending on using an implant or wearable sensor, the pressure of the eye can be sensed using various strategies. Using encapsulated capacitor chambers, it is possible to measure absolute intraocular pressure relative to a sealed reference chamber. This technique usually requires implantation inside of the eye to benefit from its main advantage of measuring absolute pressure.

1.1.3 Implantable IOP sensors

One of the very early implantable sensors ever reported is an elastomer built in 1980 that wraps around the entire eye ball and changes its electrical resistance almost linearly with change in the diameter of the eye ball caused by IOP fluctuations. The device is tethered out of the eye and was only ever tested on a rabbit eye. [28]

This approach is not scalable for human subjects with functional eyes because it is highly invasive and does not offer the advantages that come with the following approaches such as capacitive, inductive and optical methods.

Another early report shows the proof of concept for a capacitive membrane with an isolated chamber that changes its capacitance due to the deflection on the membrane caused by the inside and outside pressure variance. Having a constant pressure inside by design, the change in the outside pressure (IOP) is what determines the change in capacitance. Their results show a total change of 1 pF for a 26 pF capacitor for IOP range between 10 to 70 mmHg. The sensor module is a passive RLC and communicates with the reader wirelessly

and was only tested further on a rabbit eye. [28] Another report in 2001 (Fraunhofer, IMS-Germany) incorporates the same variable-capacitor method into an application specific circuits (ASIC) that the change of capacitor changes the resonance frequency of an oscillator which further connects to a digital counter. [29]

Eye is an optical organ, and needless to say, allows light inside perfectly. Some groups have taken advantage of this and presented unpowered techniques that employ very small implantable devices that make them relatively minimal in their invasiveness. Chen et al. report a needle-based suture-less Bourdon tube that its pressure response is manifested by its mechanical conformation and its read visually. The tube deforms with the change in the pressure difference between the internal encapsulated chamber and the external ambient pressure. This deformation is visualized with the movement of the pointing tip at the free end of the tube. That movement is linearly related to the pressure difference. The efficacy of the device is tested on several porcine eyes before eventually inserted into a rabbit eye. [30] They achieve an approximate resolution of 3.56 mmHg with a device smaller than $4mm^3$. Another optical micro implant is reported by [31] in which a nanodot array is placed inside an optical cavity on top of a circular thin layer of black silicon with a total diameter of 1mm. Using a Zeiss SL-30 slit lamp they demonstrate an optical readout distance of 12 cm, which is a record in the longest distance a change in IOP can be determined from.

One other optical approach is investigated by researchers at University of Wisconsin where they attach a micro-fabricated silicon diffraction-grating-array onto the choroidal tissue in

the back of the eye and monitor the slight changes in the color of the gratings caused by the subtle strain in the choroid. This attempt is based on a hypothesis that there is a correlation between glaucoma and presbyopia (the age-related loss of accommodation due to their increasing inelasticity at the ciliary body) [32]. They actually only test their proposed design in a bench setup that consists of a PDMS membrane that mimics the choroidal tissue of the eye and camera, beam splitter, and an objective lens. They change the back-pressure to move the membrane by regulating the amount of water underneath it. This causes the membrane to provide the necessary strain needed for testing the grating sensor. The period and duty cycle of the grating patterns are 580 nm and 50%, respectively and the area of each array is 20×20μm^2. Their characterizations do not yet quantify the strain as much and is mainly qualitatively proving the concept. [33]

Another research group have presented two devices that one is purely capacitive sensing and the other one combines both inductive and capacitive sensing. The first one only deploys a variable capacitor and the other in which the movable membrane varies both a capacitor and an inductor. Both models present a high pressure sensitivity of 7000 ppm/mmHg with smaller than 1 mmHg of resolution. A six-month animal study verifies the *in vivo* bio-efficacy and bio-stability of this implant in an intraocular environment with no surgical or postoperative complications. They suggest two locations for implanting their sensor; one is pars plana and the other is iris [34]. Another design is realized with the same research group with a larger and flexible coil based on membrane-based variable capacitor. In their unique design, an iris anchor is achieved using a tampered retractor that hooks to

the iris strata. This enables minimally invasive device fixation inside the eye. Their device functions at a resonance frequency of 350 MHz with a 2cm sensing distance in air and a pressure sensitivity of 455 ppm/mmHg and a responsivity of 160 kHz/mmHg with a projected pressure accuracy of 2.5 mmHg in practical IOP monitoring. [35]

A higher sophisticated approach is taken by researchers at University of Michigan (U-M) in realizing an integrated microsystem containing a solar cell, thin film Lithium battery, MEMS capacitive sensor, and integrated ASIC all-together sealed in one biocompatible glass housing. Their system measures IOP every 15 minutes. Their capacitance-to-digital converter yields a resolution of 0.5 mmHg. IOP data is stored into a 4kb static random-access memory (SRAM) that can store 3 days of data at once. Their microprocessor is potentially capable of performing Digital Signal Processing (DSP) or compression to extend the storage capacity to over 1 week. The user reads the IOP data by bringing an external device adjacent to their eye. [36]

Altering the location at which a pressure sensor can sit in the eye, researchers at Purdue University suggest a circular curved-surface composite membrane that sits in the anterior chamber which its variable capacitance is detected by an ASIC. Even though they propose a full design, however, their progress ends at measuring the capacitive pressure sensitivity of a single cavity with two contact pads, an MMR probe station and the Agilent 4284A LCR meter. Their results show a 3.3 fF/mmHg per capacitor unit area (mm^2) with a smaller sensing area of 300×300 μm^2. Their sensor is meant for a rat eye, therefore, they suggest a

curved design to be able to fit the entire system inside a rat eye. The corresponding radius of curvature of the anterior chamber is calculated as 4mm. [37]

Similar ocular location is chosen by researchers at MSU [38] in placing a capacitive membrane-based sensor accompanied by an inductor for passive wireless communication. Their device outperforms many similar competitors in the telemetry range by having their coil dimensions increased to more than 15mm in outer diameter and three wide turns. They have also created an on-chip integrated variable capacitor that does the pressure sensing. Their fabrication method employs a fold-and-bond method. They characterize their device in saline, deionized water and air and show a 28mm maximum telemetry range inside water with a 156 kHz/mmHg pressure sensitivity.

A group at University of Washington in Seattle are inspired by a group of commercially available implants called capsular tension rings (CTR). CTR implants began their introduction to the ophthalmic markets in early 2000s to help patients who undergo various cataract complications. These implants mainly help the circular expansion and stabilization of the capsular bag in the eye. They also provide safer intraocular lens (IOL) centration in the eyes suffering from zonular dehiscence and in some cases they reduce the risk of capsular fibrosis. [39] Their sensor design consists of an RF chip, an off-the-shelf pressure sensor (E1.3N, microFAB Bremen GmbH, Germany) and an antenna assembled on a printed circuit board. The device is powered at 2.716 GHz from a distance of 1-2 cm and their flexible antenna can withstand up to 33.4 kPa without any electrical disconnection.

Their characterization results show a 16.66 Hz per mmHg sensitivity. Their prototype is at its very early stages and is not integrated with an actual CTR and the corresponding miniaturized circuits. [39]

Another team at Purdue University takes up an approach inspired by vitrectomy and inserts a needle into a site called Pars Plana. Their transponder consists of three parts, a 30-gauge needle that penetrates the sclera and creates direct access of the aqueous humor with a capacitive pressure sensor, and a planar coil that serves as an antenna. Even though multiple surgical and technical complications occurred in their *in vivo* tests, they achieve a 15 KHz/mmHg of responsivity with about a 1mmHg of resolution in their *in vitro* tests. Further on, they present a good biocompatibility and acceptable inflammatory response with a one month implantation in a rabbit eye. [40]

Similar approach is taken by another team in California (Caltech & USC) by placing a capacitive pressure sensor outside of the eye near Pars Plana and connecting them to the internal chamber using a cannula. They have used a commercially available pressure sensor (STMicroelectronics LPS25H) that sends out digital data and communicates with a custom-designed 65-nm CMOS chip that consists a power management circuitry receiving wireless power at 915 MHz, a data telemetry unit and a serial I2C interface for communication with the sensor. They claim their Parylene-on-oil encapsulation achieves more than 4 times the sensing element stability along a 4 times longer period of time comparing with the

previously reported IOP sensors (>2 mmHg drift in one month versus 0.5 mmHg drift in four months). [41]

Among devices that have been commercialized, the efficacy of a capacitive sensor implant called EYEMATE® is studied for one year in four patients and is reported to be well-tolerated by patients despite early postoperative inflammation and it enabled them to perform self-tonometry at home by following a set of instructions [42]. The sensor is encapsulated inside silicone rubber and is made of eight pressure-sensitive capacitors and a planar and circular micro-coil antenna for passive data communication. The capacitors gauge the pressure along with a temperature sensor for compensation. A hand-held device records, digitizes and displays results. The patient has to hold the reader in front of their eyes. The company obtained CE approval for their implant in mid-2017.

The main disadvantage with implantable devices is the implantation itself. It requires surgery which limits the use of the system to the small group of patients who undergo other surgeries for other purposes such as cataract. Other drawbacks include packaging issues with leakage that can cause uncontrollable inaccuracy, poor biocompatibility of most conventional materials which can cause postoperative inflammation, toxicity, and biofouling which can significantly degrade the performance over time. [42]

1.1.4 Wearable IOP sensors

Wearable sensors, in the contrary, are promising approaches for monitoring health markers and monitor physiological signals for all individuals regardless of their severity of symptoms or the type of their treatments. They can also be used by healthy individuals for research studies. Therefore, commercially speaking, implantable devices have a much longer developmental path to get the necessary approvals for commercialization and they suffer from very small market size comparing with the wearable sensors with millions of potential users.

One of the very earliest contact lenses, incorporates a wire in its peripheral edge integrated with two different types of transducers. One, with semiconductor and the other with foil transducer. These tethered contact lenses were instrumented and tested on rabbit eyes back in 1974. Their technique observes the deformation in the angle where the cornea joins the sclera. Their attempt is based on the hypothesis that this area carries the largest deformations with change in IOP. They rely on a theoretical value of 0.02 to 0.016 radians per mmHg of IOP change for pressures in the range of 10 to 45 mm. They used two different types of semiconductor and one type of foil strain gauge with resistances ranging from 330 Ω to 960 Ω. The output of their Pixie semiconductor gauge is measured and shown to be linear over a range of 20 mm to 57 mm with a slope of about 0.08 Ω/mmHg. [43]

For almost three decades, apart from a number of patents with minimal design information shared, no significant attempt was reported in integrating contact lenses with sensors. In

2011, Laukhin et. al. in Catalonia, Spain place a piezoresistive polymeric sensing film centered inside a soft contact lens and wired to a portable device that collects, processes and sends out data via Bluetooth to a computer. They achieve a range of 0.5 to 1.5 Ω/mmHg for their sensitivity depending on whether the contact lens is protected or not. The one which was protected by a hard contact lens showed a lower sensitivity. The base radius of their lenses is 8.8 mm. [44]

Later on, Tseng et al. propose the idea of a single turn planar coil that sits inside a contact lens and changes its diameter with a change in IOP. Their development is limited with solely sensing an inductor's value being tested wired to the reading instruments and their proposing RFIC for wireless communication is not implemented yet. [45]

Another Contact Lens Sensor (CLS) that employs a capacitive sensing element is reported by [46]. They use standard commercially available HEMA and cast a 200μm-thick layer of contact lens and place an RFID chip with an antenna and a capacitive circular ring that changes the distance between its two plates when the curvature of the cornea changes due to pressure change. They report a reading distance of 1cm under 26.5 dBm incident RF power at 920 MHz and achieve a pressure sensitivity of 4.4 fF/mmHg.

A thin contact lens made of elastomeric materials is a suitable carrier for ocular sensors. Given the right casting curvature and proper materials they can conform to the cornea very well and present good permeability for air and tear molecules. Multiple sensors are

developed inside a contact lens employing various sensing mechanisms such as strain gauge using piezo-resistive materials, variable capacitive or inductive elements. SENSIMED Triggerfish® (Lausanne, Switzerland) is a CLS that incorporates an embedded micro-sensor that responds to spontaneous circumferential changes at the corneoscleral junction and transmits the data with a coil antenna to an external reader coil that is placed around the eye cavity using adhesive fabric. The reader coil is wired to a pocket-size signal processing and storage unit. The efficacy of this device is studied and compared with Tonopen® pressure readings on twenty patients undergoing laparoscopic colorectal resections and results show a poor correlation between the data obtained by the two measurement units. [47].

Both of the above CLS solutions involve a chip in the sensor circuit that adds complexity and cost to the overall system. In our solution we eliminate the use of electronic chips and use basic RLC components. Variable capacitors as mentioned earlier usually suffer from leakage and unwanted baseline shift. We eliminate the use of variable capacitors to address that issue and instead propose a variable inductor as the sensing element integrated with constant capacitor. The wavy serpentine morphology of the coil introduces stretchability and therefore change of its radius corresponds to the change of the central corneal curvature.

1.2 Slowing Down Vision Loss with Optogenetic Stimulation

The progressive degeneration of retinal ganglion cells (RGCs) and their axons is one of the commonly observed processes in glaucomatous patients. This optic neuropathy is shown to slow down by treating the central visual pathway (CVP) with long-term positive effects. As shown in Fig. 1 one of the treatments that have been shown effective in enhancing endogenous levels of trophic factors in CVP is combining optogenetic stimulation with brain-derived neurotrophic factor (BDNF) treatment [48]. These early studies open new horizons in acknowledging the possibilities of treating glaucoma beyond just treating the eye alone and/or simply using biochemical drugs. Such approaches in treating degenerative vision loss demands novel devices with small form factor that can be used to wirelessly stimulate the visual cortices of mice in various behavioral experiments to further study the various factors and parameters in optimizing such treatments before one day they can be employed in human beings.

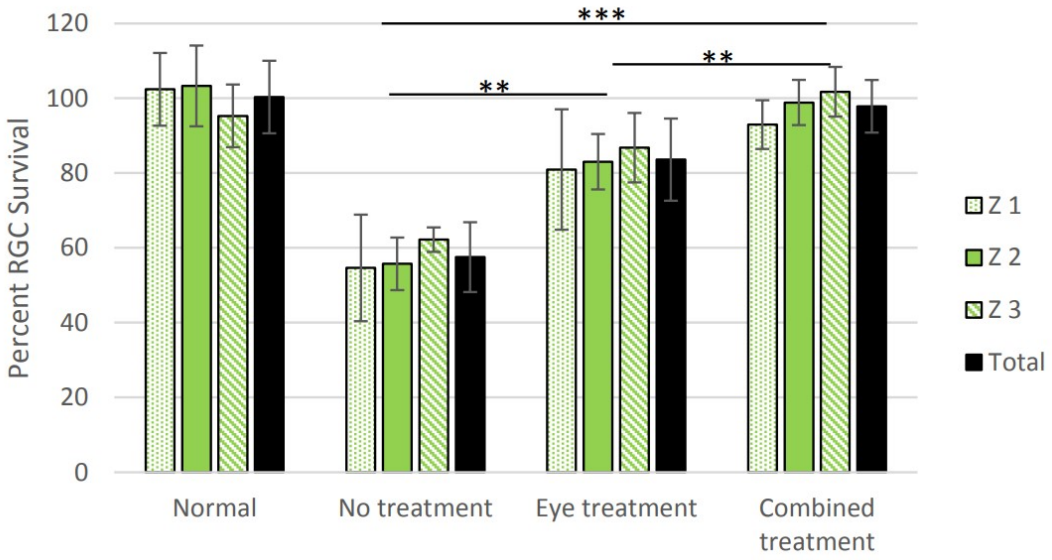

Figure 1. Comparing the survival of ganglion cells in retinas of animals who received different treatments within 9 days post-application. The combined treatment of optogenetic stimulation and BDNF treatment shows superior results compared with no treatment and the BDNF treatment alone. These data are derived from nerve crush and not elevated IOP [48].

Optogenetics is a technique that enables manipulating single-cell activities in genetically modified living organisms [49-51]. However, the light-delivery systems are yet limiting behavioral experiments on freely moving animals. Current optical systems either use tethered optic fibers which limit the comfort and freedom of the animal [52-54] or in case of LED several attempts present bulky solutions that most of the device is out of the animal's head [55-59]. Some smaller designs that can be fully implanted require near-range inductive power delivery at MHz carrier frequencies, which significantly limits the range in which the animal can freely move around [60]. In case the frequency range is higher the animal can get further within a couple centimeters but still has to be inside a small cage which still does not free the animal and is very expensive to be constructed. The high

operating frequency also increases the risk of over-exposure of electromagnetic radiation to nerve tissue, resulting in microwave-induced heating [61]. The electrical current delivery is also limited comparing with battery-powered systems and there are other potential issues with orientation and polarization while working with RF power harvesting techniques.

In this thesis we present an attempt at creating an implantable device that would leave only two pin clips out of the animal's head holding onto a replaceable coin battery. The entire circuitry is packaged inside a Simblee chip and 3 analog output pins are used to drive a microscale LED (μLED). Commercially available μLEDs are utilized, which are more affordable and accessible compared to monolithically fabricated LEDs presented in [62]. Chapter 3 describes the details of this project.

1.3 Bionic Vision: A Reality

Once the prevention and slowing down vision loss techniques and strategies fail as in most cases, vision loss is inevitable and patients with degenerative diseases go blind eventually. For a long time in history, it was utterly a science fiction story to talk about curing blindness or restoring sight for even partial amounts. However, today there are multiple approaches available that have shown proof in reversing the loss of sight emitting light at end of the tunnel for millions of patients who never experienced sight or have been living in darkness for decades.

Retinitis pigmentosa (RP) causes loss of photoreceptors which leads to blindness. RP has an estimated prevalence of 1 in 4000 worldwide [63]. However, information can be

reintroduced to the remaining functional retinal neurons using electrical stimulation. The stimulating electrodes are categorized into four major types based on the anatomical location they are implanted in the back of the eye. If the electrode array is placed on top of the retinal ganglion cells it is called *epiretinal* electrodes. If they are placed between choroidal tissue and retinal tissue they are called *subretinal*. If they are placed between the sclera and choroid they are called *suprachoroidal* and if they are inside sclera they are named as *intrascleral* electrodes. The implant communicates with the external wearable and/or desktop equipment using either tethered or wireless communication.

1.3.1 Visual prosthetic implants

One of the most successful commercialized devices in addressing visual impairments is the Argus II made by Second Sight Medical Products Inc. (Los Angeles, California). The device is an epiretinal prosthesis system that is developed to restore partial vision to patients that suffer from blindness caused by RP or outer retinal degenerations.

The surgically implantable part of the system consists of a 60- electrode array and a receiver coil. There is a video camera in user's glasses that transmits information wirelessly to the implant that sits in their eye. They can see black and white low-resolution imagery that works well for high contrast views in daylight. This gives them a general sense of their surroundings. The system allows them greater independence in their daily life. Most recipients can perform basic activities better with the implant than without it. Many others can locate lights and windows, follow lines in a crosswalk, or avoid running into things as

they walked. Some can sort laundry or determine where other people are located in a room, and about half of them are able to read very large letters- about 9 inches high.

The implant is currently offered at the University of Michigan Kellogg Eye Center, one of 13 major centers across the US to offer the implant. It costs $150,000 for a unit plus the cost of surgery and patient training. A number of private insurers and Medicaid cover the cost. It is expected to work for hundreds of thousands of people.

A five-year long study on safety and performance of the Argus II in a clinical trial paved the way for this product to be given regulatory approval in the European Economic Area (CE Mark) in 2011 and in the United States (FDA) in 2013. In twenty four out of the thirty patients the implant remained in place and remained functioning. One adverse event was experienced after the third year. Patients performed significantly better with the implant ON rather than OFF on all their visual function tests and functional visions tasks including square localization, direction of motion, and grating visual acuity [64].

As of 2018, the subretinal implant called Alpha AMS has a CE Mark and may seek FDA approval in the United States soon. The system is created by a company named Retina Implant AG with headquarters in Reutlingen, Germany. This device can mimic the functionality of the degenerated rods and cones to some extent by stimulating the outer

retinal tissue electrically. Then, information is transmitted to the visual cortex of the brain through the optic nerve which can then generate visual images. The image is initially generated by a light sensor chip which is 3.2 x 4 mm in size with a height of 70 µm equipped with 1600 photodiodes, which convert the incident light into electrical signal. Then, this signal is amplified and relayed through electrodes to the retinal signal processing layers of the patient which are still functional. From there, the signal follows the natural optical path through the optic nerve and radiations into visual cortex, where information is interpreted, and visual images are constructed. [65] Placing the implant under the retina, enables the patient to move their eyes naturally. There is no special camera needed to take pictures outside the eye as in The Argus II.

It is important to note that The Argus II implant communicates with the external equipment in the glasses wirelessly with a coil. This makes the system more sophisticated and costlier, however, reduces the surgical failure rate and minimizes post-surgery complications. However, Alpha AMS and the other suprachoroidal implant wire their ocular implants to the outside through a subdermal path which simplifies the system but creates considerable risk of serious adverse effects.

One study, published in March 2018 [66], assesses the efficacy of Alpha AMS for partial restoration of vision in end-stage RP. They implant the device into the worse-seeing eye of 6 patients with no useful perception of light vision. The implant improved visual

performance in 5 out of 6 participants and exhibited ongoing function for up to two years. The improvement includes better light perception, enhanced light localization, and superior grating detections. However, implantation surgery remains challenging for this implant which required frequent post-surgery repairs for some individuals.

Another subretinal array is developed at Stanford University and may enter clinical testing soon. This system is a near infrared (NIR) wireless array with a corresponding head-worn imaging system, in which photovoltaic pixels convert pulses of light into pulsed electrical current and stimulate the nearby inner retinal neurons. In this strategy images are projected onto the implant with NIR light by means of a display near the eye (video goggles). In their latest study stimulation thresholds, dynamic range, frequency dependence and contrast sensitivity of the prosthetic vision of anesthetized animals were assessed by recording the waveforms of electrical stimulation on the cornea using conventional electro-retinogram (ERG) electrodes [67].

There are two other bionic implants that are in the middle of their clinical feasibility tests. These approaches being developed in Australia and Japan place electrode arrays in the suprachoroidal and intra-scleral regions in the back of the eye. One of the main benefits of implanting the electrodes in these regions rather than epiretinal and subretinal regions is that the surgical placement is less technically challenging and does not breach the retinal tissue, however the electrodes are further away from retinal ganglion cells. Therefore, they

require more electrical current for stimulation [68]. Both of these systems use tethered communication between the implant and the central processing unit through a subdural wire.

Bionic Vision Australia surgically implant their electrode array in between the firm fibrous sclera and the outer retina/choroid in an eye of three human subjects who suffer from end-stage RP. Presenting their data in [69] coupled with a twelve-month post-operative efficacy data they show that their surgical procedure is safe, the position is stable, the device is able to provide percepts in all three subjects, and the implant remains tolerated and functional over the course of twelve-month trial period.

In a one year study, the Japanese group investigates the stability of their intra-scleral prosthesis and study the effects of the adverse events, and the efficacy of the system. Results show that their 49-channel suprachoroidal-transretinal stimulation (STS) prosthesis that was implanted for 1 year in the scleral pocket (under the parafoveal area) of 3 patients can elicit phosphenes in all patients with advanced RP for the entire 1 year without any major complication. The results of localization tests and table tests were significantly better with the prosthesis turned on than turned off in patient No. 3. The deviations of the walking tests were smaller with the prosthesis turned on than off in patient No. 2 and No. 3 at multiple times after the implantation. [70]

Future bionic implants and next versions of the Argus series, are going towards having more and smaller electrodes. That, however, does not linearly increase the resolution. For example, The Alpha AMS has 25 times more electrodes than the Argus II and yet its highest observed resolution is only 1.5 times better than the Argus II, rather than 6.5 times as it might be expected. [70] Higher safety and durability need to be improved in all of the implants discussed for long-term prosthesis. Higher levels of miniaturization and employing more durable and biocompatible materials are some of the ways to achieve this goal.

There is another category of interventional restoration techniques that involve implantation of micro electrodes onto visual cortex stimulating directly with the signals received from the wearable video camera after processing. Since they bypass the eye all together and also the majority of neural circuits between the eye and the visual cortex that are usually damaged due to various forms of diseases, they can potentially cure all types of blindness including diabetic retinopathy, glaucoma, optic nerve disease and eye injury. Its market size is estimated to be 50x the market size of patients blinded by RP (Addressed by implantable bionic eyes). Orion™ Cortical Visual Prosthesis developed by Second Sight is one of the leading products in this category which is currently under clinical feasibility testing on six human subjects at Ronald Reagan University of California in Los Angeles (UCLA) Medical Center and Baylor College of Medicine.

1.3.2 Enhancing flexible microelectrode array technology

As incredibly complex as it may be to understand how brain works, with collective cooperation and global collaboration humans have uncovered remarkable insight into molecular and electrochemical mechanisms that govern central nervous system. The neuroscience and neuroprosthetics community demand ever-increasing density of electrodes with more channels in the important mission of expanding the communication bandwidth between the two complex worlds of living neurons and electronic computers. Besides, simultaneous somatodendritic patch clamp recordings and two-photon imaging has recently shown that exclusive disjunction (XOR) operation is performed in human dendritic cells [71]. Exclusive disjunction is a logical operation that outputs true only when inputs differ. These findings are strong evidence for not only it is highly desirable to speak with and listen to each neuron separately with thousands of channels but also it can be advantageous to tap and modulate multiple points on a single neuron and treat them beyond singular units of summation and multiplexion. This possibility requires compact microelectrode arrays (<10μm) with lesser pitch (<5μm). This would allow placing thousands of individually controlled channels in a series of ultra-small penetrating microelectrode arrays with high aspect ratio (>2mm) providing ultra-high-bandwidth direct brain-computer-interface for neural modulation including both recording and stimulation.

Conductive polymers present mechanical flexibility, outstanding biocompatibility, remarkable electrical properties and, most of all, cellular agreement. However, for long-term chronic applications they fall short in their electrochemical endurance and mechanical adhesion to their base substrate materials. Multiple electrochemical approaches have been investigated to improve the adherence of Poly(3,4-ethylenedioxythiophene) (PEDOT) onto their underlying metallic thin films.

In this chapter we introduce the work done by the author during their internship at Second Sight Medical Products Inc. In this work, an electrochemical treatment of platinum microelectrodes with diazonium salt is incorporated as an electrochemical adhesion promoter for PEDOT and it is further combined with using the highly microporous geometry of platinum-grey; a technology developed by Second Sight medical Products Inc. (SSMP). The intertwined mechanical integration of Pt-Grey and PEDOT together with the covalent binding agency of diazonium salt provide an unprecedented long-term stability of more than 100 days while providing 70x enhancement to the electrical performance of the microelectrode arrays. We show that a typical PEDOT coating (1μm) alone offers 130x improvement to the electrical capacitance of the interface while it degrades in less than thirty days when coated on bare platinum with only diazonium salt for adherence. We also show that that the microporous Pt-Grey coating (8μm) typically offers 35x improvement to the electrical capacitance of the interface while it has stability for more than a decade in human subjects. We combine the two coating technologies and achieve a composite coating that offers 70x improvement to the interfacial capacitive impedance while it lasts

more than 100 days before it starts to show significant loss of performance and remains functional for more than 450 days. For demonstrating the long-term stability we conducted in vitro experiment under electrical stimulation using a biphasic square wave at 120 Hz and a peak value of 105 μA inside phosphate-buffered saline (PBS) at 37°C for 452 of days.

In this chapter, the author suggests and investigates microporous platinum-grey as an underlying thin film substrate for promoting the integration of PEDOT adhesion. Furthermore, diazonium salt is electrografted on Pt-Grey which yields a covalent bond between Pt-Grey and PEDOT on a molecular level [72]. Eventually, the unique hybrid advantages of PEDOT:Diaz:Pt-Grey composite is presented in attaining supreme electrical characteristics while remaining unchanged for long periods of time under standard round-the-clock electrical stimulation in vitro. This is the very first time the mechanical integration of microporous material is combined with the electrochemical benefits of using diazonium salt in creating a hybrid composite that demonstrates long-standing strong adhesion between PEDOT and inorganic microelectrodes such as Pt. The major significance of this report is highlighting the benefits of considering microporous solid state coating technologies [73-79] as substrate materials for conductive materials while incorporating electrochemical adhesion promotion strategies such as diazonium salt. Chapter 4 describes this project in detail which was conducted during an internship at SSMP as part of this thesis.

CHAPTER 2

Wireless, Passive Strain Sensor in Contact Lens for Continuous Non-Invasive Self-Monitoring of Intraocular Pressure

2.1 Introduction

After cataract, glaucoma is the second leading cause of blindness worldwide and real-time monitoring of intraocular pressure (IOP) is of great demand. In this chapter, we present a wireless, passive sensor sitting inside a customized, planar and circular doughnut-shaped contact-lens capable of continuous monitoring of change in the curvature of cornea caused by IOP fluctuations. The sensor consists of a constant capacitor and a variable inductor in form of a stretchable, closed-loop, serpentine wire that serves as both the sensor and the antenna. Results show a pressure responsivity of 523 kHz per 1% axial strain on a pressurized Polydimethylsiloxane membrane and 44 kHz per 1 mmHg of change in IOP of a canine eye. The main sources of this difference in performance include the imperfect conformity of contact lens on the cornea, the completely different mechanical characteristics of the eye tissue itself compared with a PDMS membrane, and also the poor coupling of our contact lens to the absolute values of strain in cornea.

Furthermore, the sensors are tested for stability and showed unvaried characteristics after repeated cycles and parasitic movements. Predictable influences of temperature and humidity on sensor response are also verified experimentally, which can be canceled out

using real-time calibration with temperature and humidity sensors to integrate with a reader device. The design reported here has numerous advantages, such as design simplicity, component reliability, high responsivity, and low cost, thereby opening up potential opportunities for the translation of this non-invasive, continuous IOP monitoring technique into clinical applications. Initially, we developed an implanted version of the variable inductor with an on-chip SMT capacitor soldered to the ends of the wavy serpentine wire. We implanted the device under a flap of sclera right at the corneoscleral junction and reported a pressure sensitivity of 57 KHz per mmHg [80].

Later on, we designed and advanced a non-invasive wearable CLS that is made of a doughnut shaped thin polymer film that has the role of the contact lens that conforms onto the cornea and holds the stretchable sensor inside of it. This sensor is a stretchable coil that is coupled with a constant capacitor. The capacitor is fabricated along the coil using microfabrication techniques. The sensor comprises thin film metal layers made of gold, titanium, and copper for conductive layers and the dielectric layer between the capacitor plates are made of Parylene-C. The entire sensor is packaged using Parylene-C which makes it a standalone biocompatible sensor that can be used not only on cornea for glaucoma patients but for many other biomedical applications that detecting deformation, change in strain, or monitoring morphology is desired. A set of reader coils integrated inside an electronic pair of glasses can communicate with the contact lens and transmit the change of pressure to a mobile phone via Bluetooth. The data can be used in profiling patients

remotely on a long-term basis. The patient can also take actions accordingly, whether to use eye drops, contact professionals, or schedule appointments.

2.2 Materials and Methods

2.2.1 Principles of operation and design

Our sensor is designed based on passive electromagnetic telemetry [81-85] which does not require an internal power source as seen in active sensors. The sensor device operates as an RLC resonator circuit (Fig. 2) including a capacitor (C), an inductor (L), and a resistor (R) in a passive fashion. Change in either one or two of these three elements can be detected by reading a shift in the resonance frequency of the resonant tank. When deformed under different IOPs, our device has a constant capacitance, a significant change in the inductance, and negligible change in the resistance, resulting in a shift in the resonance frequency as depicted in the equation below.

$$f_{res} = \frac{1}{2\pi}\sqrt{\frac{1}{L_s C_s} - \frac{R_S^2}{L_s^2}} \Rightarrow f_{res} \cong \frac{1}{2\pi}\sqrt{\frac{1}{L_s C_s}} \quad \text{(I)}$$

V_{SG}: Signal Generator Voltage Source
R_G: Signal Generator Internal Resistor
R_m: Measurement Resistor
Z_r: Reader Coil Impedance (Inductive)
L_s: Sensor Variable Inductor
C_s: Sensor Constant Capacitor
R_s: Sensor Parasitic Resistor
f_{res}: Resonance Frequency

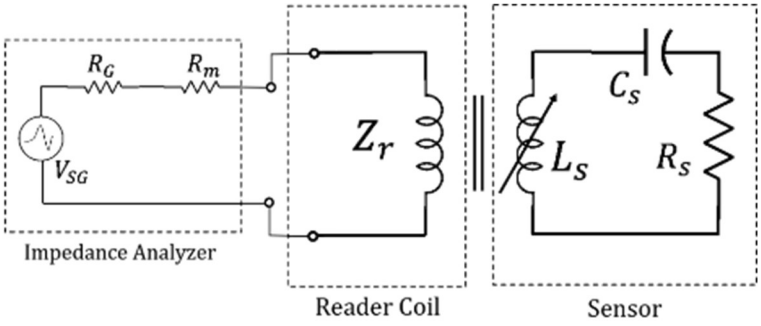

Figure 2. Circuit model for the continuous IOP monitoring system.

The capacitor is modeled as a fixed, double plate capacitor, and the capacitance (C) can be estimated using the following equation for ideal double plate capacitors:

$$C = \varepsilon_0 \varepsilon_r \left(\frac{A}{t}\right) \quad \text{(II)}$$

where ε_r is the relative permittivity of the dielectric material, ε_0 is the vacuum permittivity, A is the overlapping area between the capacitor plates, and t is the thickness of the dielectric material or the separation between the plates of the capacitor. Based on Perry's approximate formula [86] the theoretical strain-sensitive inductance (L) can be calculated using Equation III:

$$L = \frac{4\pi n^2 a^2}{0.2317a + 0.44\, b + 0.39\, c} \quad \text{(III)}$$

where n is the number of turns of the coil, a is the mean radius of the coil, b is the width of the rectangular-cross-section wire that the coil is made of, c is the thickness of the same wire. When the serpentine wire stretches, the shrinkage or expansion of the coil varies the mean radius and causes a proportional change in the value of inductance, leading to an upshift or downshift of the resonant frequency.

The relationship between the resonance frequency and the inductance of the device can be observed by plugging experimental data into numerical analysis of the inductance of the device. Using this technique we would be able to calculate the total range at which resonance frequency may shift for a given device with specific geometry. Based on the experiment shown in Fig. 3 we can derive an aerial sensitivity for this particular device with

its particular diameter, geometry and dimensions that ends up being 0.54 MHz/mm2. Having this value that is obtained experimentally we can find the total frequency range on which this device can be shifting its resonance frequency. To do that, we need to calculate the range at which the area of the device changes when it expands.

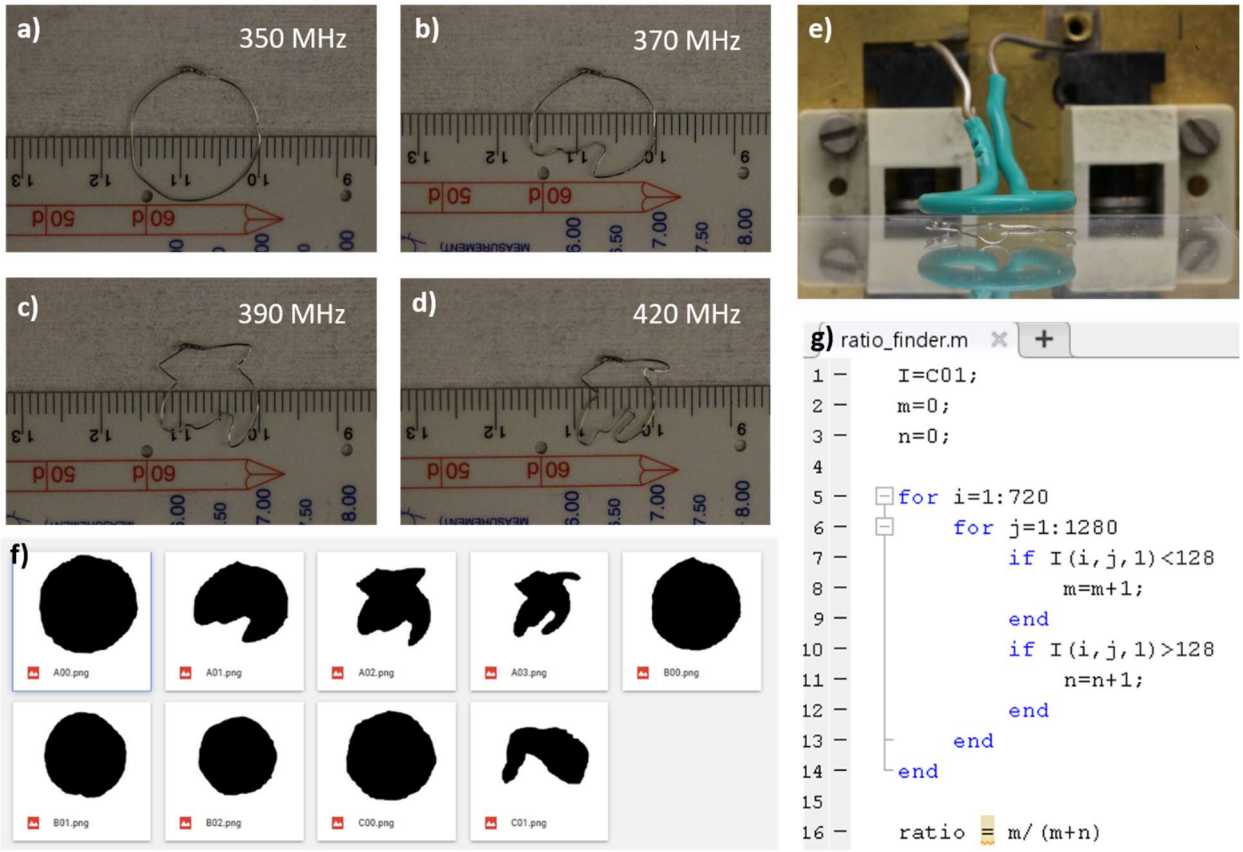

Figure 3. The various shapes that a discrete devices were turned into for validation of the theory by experiment. a) The initial state of the discrete devices and its corresponding resonance frequency at 350 MHz. b) The devices with a new shape yielding a resonance frequency of 370 MHz. c) Another shaped that the same original device were turned into and its corresponding resonance frequency at 390 MHz. d) The smallest area that the devices were turned into corresponding to the highest resonance frequency of 420 MHz. e) The front-view of the reader coil and its orientation with respect to the discrete device under test. f) The various shapes and their imported images into Matlab for finding the exact area of each shape of the same device. g) The code we wrote that takes in the top-view image of the discrete device in its specific shape and find out the exact area relative to the original area of the device.

Fig. 4 shows the inner area of the device at rest, its area while it's expanded to a full circle, and its total length which remains constant throughout the entire increase or decrease of its diameter and change of its shape. Indeed, device fails mechanically before it can reach its maximum geometrical capacity in enlarging its diameter. Therefore, here we are only looking at the geometrical limit which can never really be reached using rigid materials and solid state conducting materials. However, if another version of device is designed and fabricated using liquid metal or various conductive hydrogels, it may be practically possible to reach these geometrical limits and expand the sensing range of one particular device.

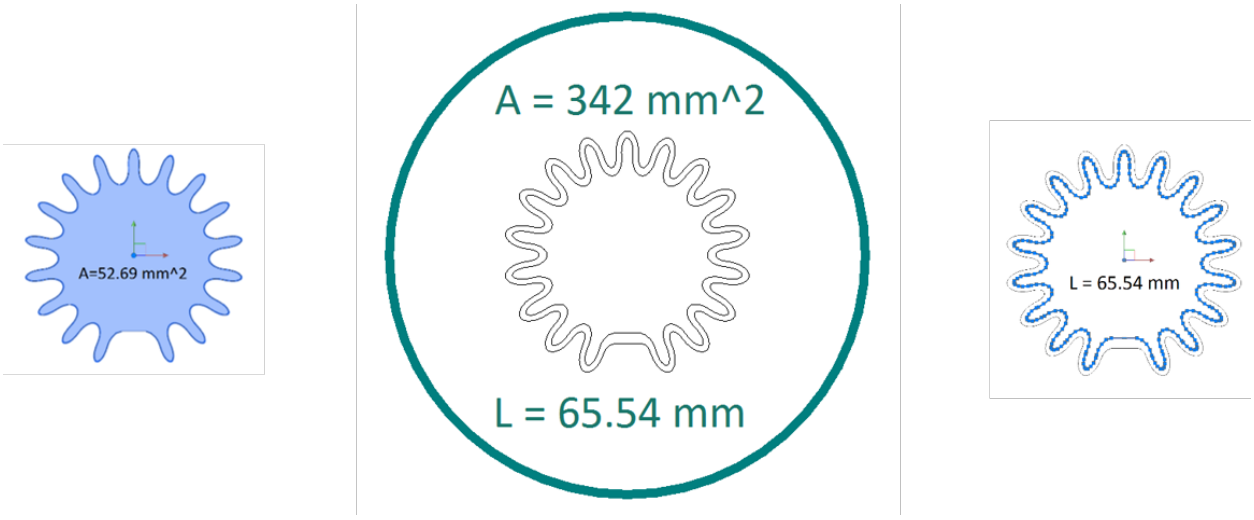

Figure 4. The IOP device and its constant length while its area changes from its original shape at rest to large areas until it changes to a full circle. These extremes show an increasing limit of shift in frequency that device can show at its most theoretical extremes.

Fig. 5 shows the two scenarios at which the area of a device changes. First scenario that is shown in Fig. 5-a shows one device with constant length that changes its morphology which

leads to a change to its two-dimensional top-view area. This change in its effective inner area yields to a change in its resonance frequency based on equations (II) and (IV). Fig. 5-b, however, shows the second episode of this experiment that we reduce the area of each device by decreasing its length and yet retaining the circular shape. This second episode shows a sharper slope of the change in resonance frequency due to change in area. That is because the length of the inductor itself is included in equation (IV) in addition to the area itself.

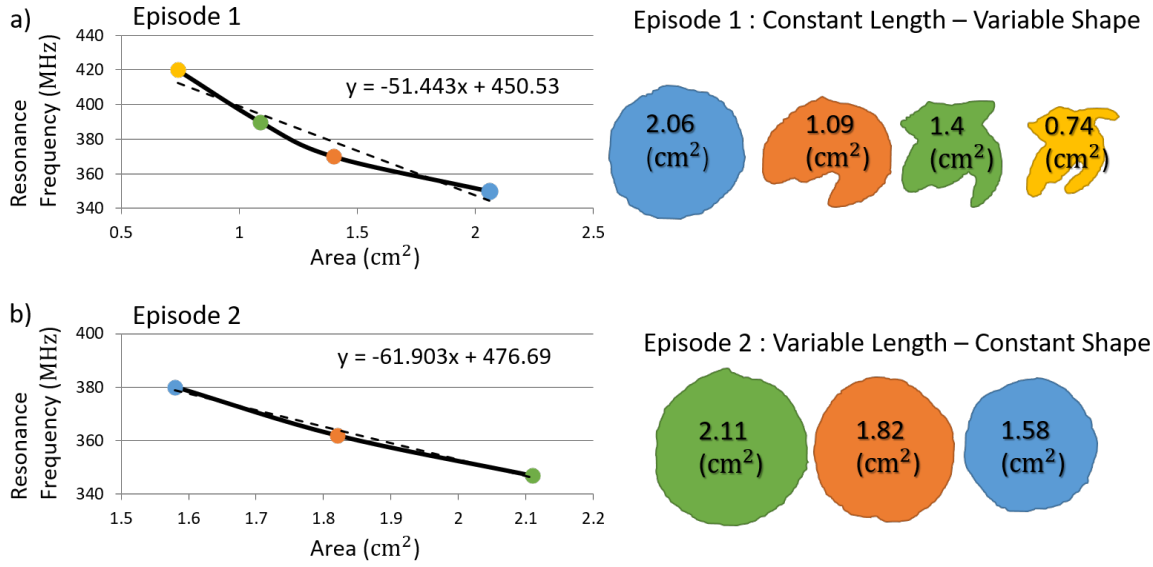

Figure 5. The relationship between the change in the area of discrete devices and the change in their resonance frequency. a) The results for the case of a device that only changes its shape while it retains its length b) The results for the case that three different devices are compared with similar shapes but different length and area.

The effect of the resistance can be neglected when the parasitic resistance is low. The following equation shows the overall resistance (R) across the serpentine wire:

$$R = \rho \frac{l}{A} \quad \text{(IV)}$$

where ρ is the electrical resistivity of the material, l is the length of the serpentine wire, A is the area of the cross section of the serpentine wire. Therefore, the material and the device geometry must be carefully designed such that the resistance of the wires is low enough to be negligible. In this case, the resonator is in the underdamped mode. The low resistance also enables high quality factor (Eq. V) which sets the fundamental limit for the detectable range of the resonance peak. With a central resonance frequency of 350MHz and typical inductance of 50nH and resistance of 15Ω, our final design show a typical value quality factor of 10.9.

$$Q = 2\pi f_{res} \frac{L}{R} \quad \text{(V)}$$

In order to obtain an accurate model of the coil and its expansion we mathematically modeled the circular serpentine wire with a polar equation as follows:

$$r(\theta) = p + q\left(\sin(n\theta)^4 - \frac{1}{2}\right) \quad \text{(VI)}$$

p is the total radius of the serpentine circular coil, q is amplitude of the oscillation of the serpentine waves and n is the number of oscillations (n=18 in this case). The total circumference of the curve (the length of the wire) is given by the polar arc length formula:

$$\text{Length} = \int_{\theta=0}^{2\pi} \sqrt{r^2 + \left(\frac{dr}{d\theta}\right)^2}\, d\theta \quad \text{(VII)}$$

Then, we calculate this integral numerically and find the enclosed area of the coil using the following polar area formula:

$$\text{Area} = \int_{\theta=0}^{2\pi} \frac{1}{2} r^2 d\theta \quad \text{(VIII)}$$

In our program executed inside Mathworks Matlab R2018b, we started with a given wire with fixed length and constant number of geometrical oscillations but flexible values for p and q. We numerically, then investigated how p and q change under various percentile changes in the enclosed area corresponding to our experimental values as shown in Table 2. Eventually, the four chosen areas corresponding to the four experimental measured data points are imported as CSV files into AutoCAD 2016 as a curve, turned into complete 3D structures and then imported into COMSOL Multiphysics 5.4.0.346 for deriving their electrical inductance.

2.2.2 Axial strain

Using a cantilever beam model [87] the sensor responsivity is also presented in the form of strain as follows:

$$\varepsilon = 100 \times \frac{R_2 - R_1}{R_2} \quad \text{(IX)}$$

where ε represents the axial strain in terms of percentage, R_1 denotes the radius of curvature of the PDMS membrane at rest (zero strain), and R_2 indicates the radius of curvature of the PDMS membrane at which the corneal strain is measured at. Fig. 6 depicts the model that relates the absolute value of the axial strain of a beam into its bending radius of curvature and the thickness of the beam. Though, in our case, by looking at the gradient of the strain in terms of percentage, the effect of the thickness is out of the equation.

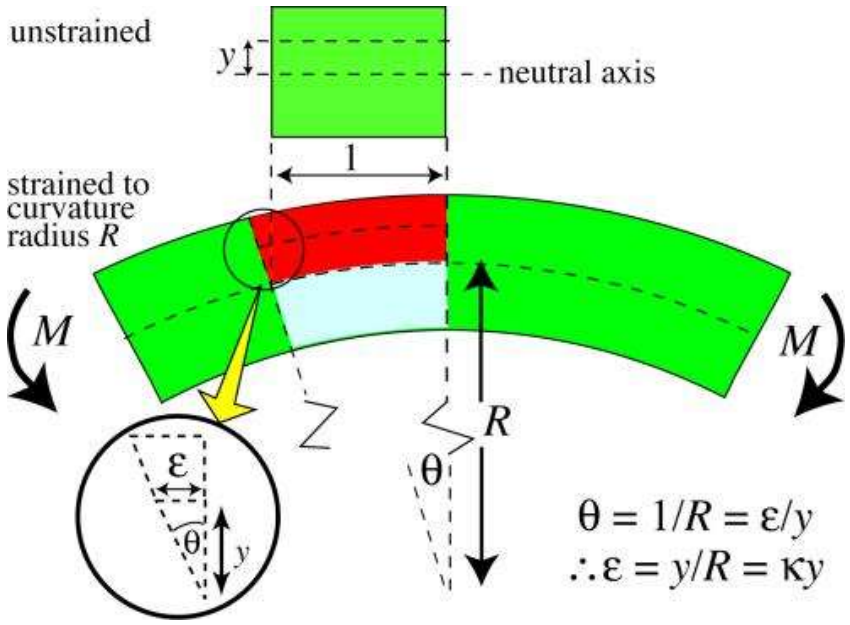

Figure 6. Relationship between the axial strain, ε, and the ratio y/R [87].

2.2.3 Sensor materials

A silicon substrate is used as a temporary carrier substrate for device microfabrication because it has reasonably good adherence with Parylene C. Parylene C serves as the structure and packaging material of the device because of its excellent biocompatibility (ISO 10993 & USP Class VI), mechanical flexibility (<200% elongation-to-break), optical transparency (<70% transmittance after 300nm), low moisture/gas permeability (water vapor transmission rate of 0.08 g·mm/m^2/day), and conformal coating using room-temperature chemical vapor deposition (CVD) [88]. Parylene C also is used as a dielectric layer of the microfabricated integrated capacitor due to its good dielectric strength (6,800

V/mil) [88]. The contact lens is made of polydimethylsiloxane (PDMS) which enables good stretchability and biocompatibility. For the main conductive material, gold is the material of choice because of its high biocompatibility and corrosion resistance. Copper is used as a sacrificial material to mask the packaging Parylene C in the plasma etching steps, and is completely removed from the final device to avoid toxic copper residuals in the ocular environment. A thin layer of titanium is used as an intermediate layer to improve the adhesion between the thin film layers of Parylene C and gold.

2.2.4 Sensor fabrication process

First, a 4-inch silicon wafer is coated with 4 μm Parylene C (PDS 2010 Labcoter® 2, Specialty Coating Systems) (Fig. 7-1). Then a layer of 20 nm titanium and 500 nm gold is thermally evaporated (Auto 306 Thermal Evaporator, Edward) on the wafer and patterned using ultra-violet (UV) photolithography to form the serpentine metal wire and the bottom plate of the capacitor (Fig. 7-2). After that, the wafer is coated with a 2 μm layer of Parylene C and a subsequent 20 nm of titanium and 150 nm gold (Fig. 7-3). This metal layer is patterned to form the top plate of the capacitor. A via is etched through metal using wet chemical etching (Fig. 7-4) and then through Parylene C using oxygen plasma with a photoresist mask (Fig. 7-5) to gain access to the first metal layer. The oxygen plasma etching is performed in a reactive ion etcher (RIE-1701, Nordson March) with a radio frequency (RF) power of 200 Watt and processing pressure of 150 mTorr. After that, the third metal layer of 350 nm gold is deposited onto the wafer which electrically connects the first and second

metal layers through the Parylene via (Fig. 7-6). The top plate of the capacitor is formed by UV photolithography and chemical etching with a photoresist mask (Fig. 7-7). The third layer of 4-μm-thick Parylene C is deposited on the wafer for packaging the entire device (Fig. 7-8). Then a 200-nm-thick copper layer is thermally evaporated (Fig. 7-9) and patterned (Fig. 7-10) to mask and protect the desired areas during the subsequent Parylene C etching in RIE (Fig. 7-11). After the surrounding unwanted Parylene C is etched off, the copper mask is removed and devices are released from the silicon substrate using minimal nudge by a tweezer inside water (Fig. 7-12). Prior to testing, the devices are rinsed with acetone, isopropyl alcohol, and deionized (DI) water to remove photoresist and metallic residuals.

After the devices are released from the silicon substrate, a cast molding method is used to integrate the Parylene encapsulated sensor inside a doughnut-shaped PDMS contact lens (Fig. 7-13). Two plastic molds with concave and convex profiles that match the eye curvature are used. During the process, PDMS is prepared by mixing the curing agent and PDMS monomers (Sylgard 184, Dow Corning) in a ratio of 1:8. After the sensor is placed on the dome-shaped convex cap, the mixed PDMS is poured into the bottom concave mold. The top convex mold is aligned and pressed into the concave mold, and the thin gap between the molds defines the desired thickness of the PDMS contact lens, which is about 180 μm. The lens then is baked on a hotplate at 50°C for two hours until the PDMS is completely cured. After the central area of the lens is removed using a circular puncher,

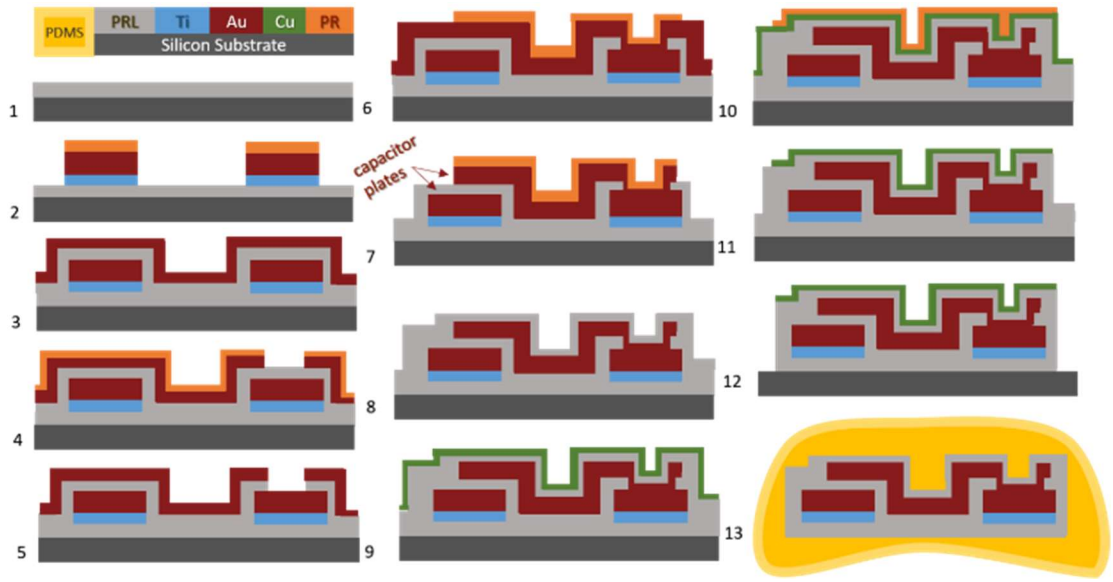

Figure 7. Fabrication step: 1) Deposition of Parylene C. 2) Patterning the deposited first metal layer. 3) Depositing the second Parylene-C layer. 4) Patterning the second metal layer. 5) Etching the Parylene-C away through the open via. 6) Depositing the third metal layer. 7) Wet etching the third metal layer. 8) Depositing the third Parylene-C layer. 9) Depositing the fourth masking metal layer. 10) Photolithography for patterning the masking metal. 11) Wet etching the fourth metal layer. 12) Dry etching Parylene-C. 13) Placing the released devices within the doughnut-shaped contact lens during the PDMS molding process.

the doughnut-shaped contact lens is released from the mold carefully with the sensor encapsulated inside the PDMS, and ready for device testing.

2.2.5 Major fabrication cost: gold

One of the major costs associated with fabricating the stretchable sensors is the materials used. Perhaps, the costs associated with manufacturing can vary significantly depending on the market, equipment, methods of fabrication and/or automation strategies. However, the least variable cost that maybe least prone to change is the materials. Among them the use of gold is the main materials that creates the bulk of the device and costs most per gram. On a typical 3-inch wafer we deposit a total of 800nm in three different steps/layers.

Our deposition technique of choice is physical thermal evaporation. At the time of fabrication (December, 2018) 24k gold were sold $65 per gram. With our largest diameter of sensor design on a 3-inch wafer we obtained 26 devices (given a 100% yield). Therefore, the cost associated with gold per device ended up at nearly $4.5. Fig. 8 shows the process flow of gold coins turning into stretchable pressure sensors.

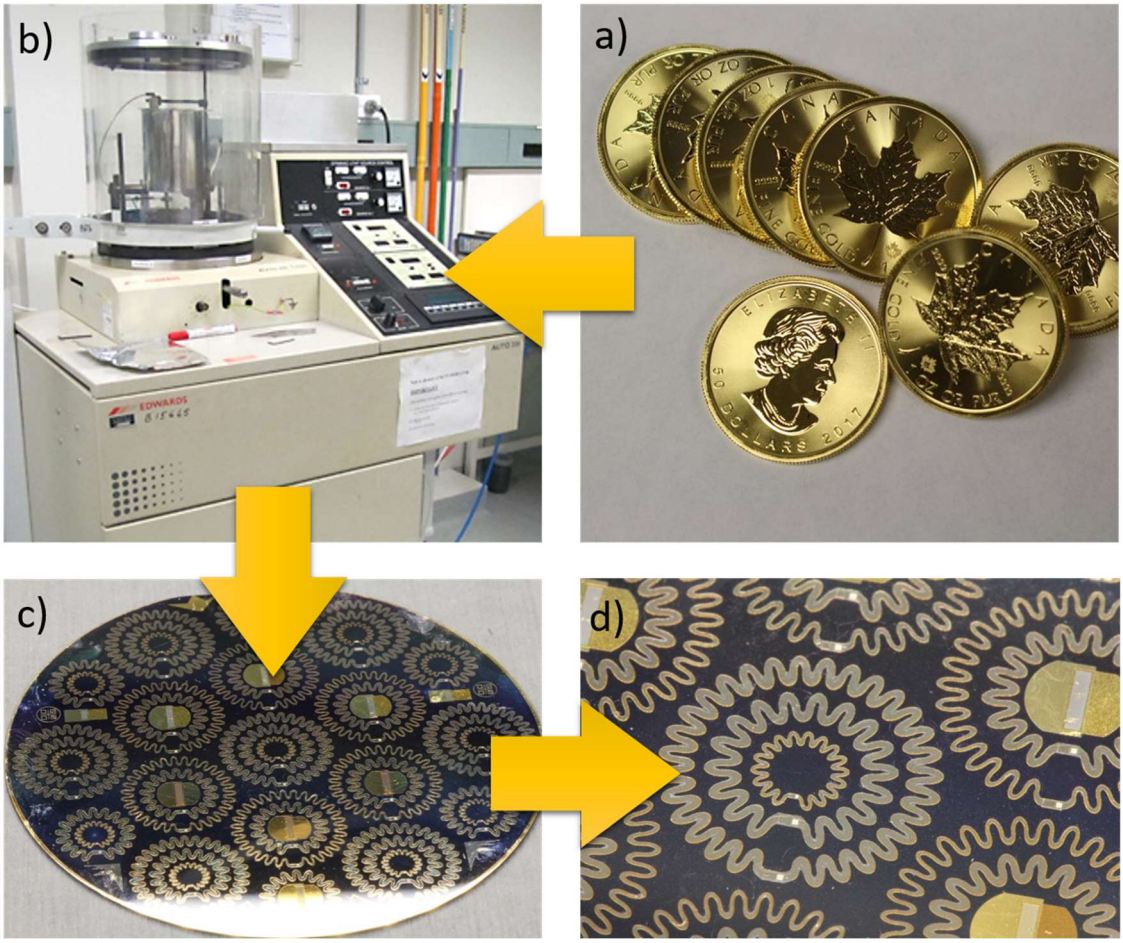

Figure 8- The process in which 24k gold turns into pressure sensors. a) 24k gold coins purchased for $65 per gram (Dec. 2018). b) Physical vapor deposition of gold onto 3-inch wafers inside clean-room. c) The largest of all diameters among our various sensor designs which yields to 13 devices per wafer. d) A closer view of the devices on wafer.

2.2.6 Sensor characterization in a controlled pressure chamber

The capacitance and the breakdown voltage of the microfabricated Parylene-based capacitor are measured using a 4280A 1 MHz C Meter/C-V Plotter (Hewlett Packard) during a high voltage cyclic voltammetry up to 500 V generated using a Keithley high voltage source meter. The DC parasitic resistance is measured using a digital multimeter (VC890C, Victor). To evaluate the strain sensing performance of the device prior to the PDMS encapsulation, a bench-top setup was constructed which consists of a pressurized air chamber sealed by a top deformable PDMS membrane. The chamber is connected to a syringe from the bottom, which controls the volume of air through a syringe pump. During the infusion cycle of the pump, the pressure inside the chamber is raised and pushes the membrane up, which causes the sensor to expand. As a result, the coil diameter increases, corresponding to an increase in the inductance value and a decrease in the resonant frequency of the RLC circuit. Computer simulations using COMSOL Multiphysics 5.4.0.346 are shown in the last row of Table 2 and they depict the consistent increase in the inductance values from the resting state towards expansion. During the refill cycle of the pump, the pressure inside the system goes down, and the membrane collapses and regains its radius of curvature. This reduces the radius of the coil, resulting in a decrease in the inductance and therefore an upshift of the sensor resonant frequency. The frequency response of the sensor is measured by coupling the sensor coil to an external coil antenna that is connected to an RF impedance analyzer (HP 4191A, Hewlett Packard), and the chamber pressure is simultaneously measured using a pressure gauge (Traceable Pressure

Meter, Control Company). Fig. 9 shows the overall setup for the controlled pressure chamber experiment.

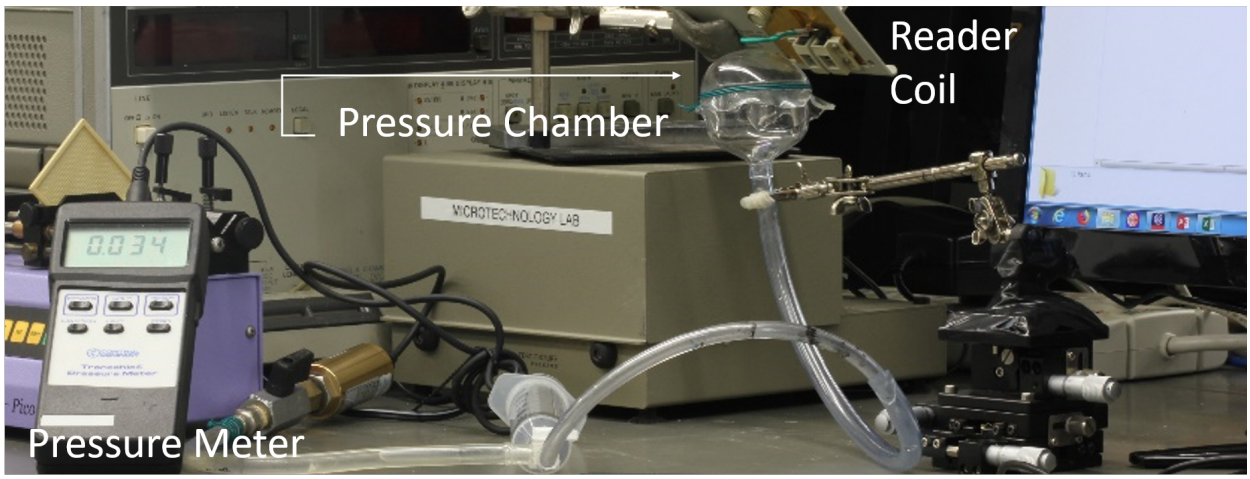

Figure 9. The Overall setup for the controlled pressure chamber experiment on the sensor inside PDMS membrane.

2.2.7 Ex vivo characterization on canine eye

An ex vivo experiment was performed to validate the functionality of the doughnut-shaped PDMS contact lens sensor on a canine eye. In this case, a micro-syringe (gauge number: 23s) was used to inject saline into the anterior chamber of the eye in order to elevate the IOP, and refilled to remove saline from the eye and thus reduce the pressure. The actual IOP was measured using a pressure gauge that was connected to the micro-syringe. Similar to the bench-top setup, a single-loop reader coil was placed in close proximity to the sensor coil in order to detect the pressure-dependent frequency response of the sensor. The canine eye was retained in the orbit in the fully-isolated head with intact bones, tissues, and hair

to better mimic the in vivo environment. Fig. 10 shows the placement of the doughnut-shaped contact lens on the eye of a decapitated post-mortem dog.

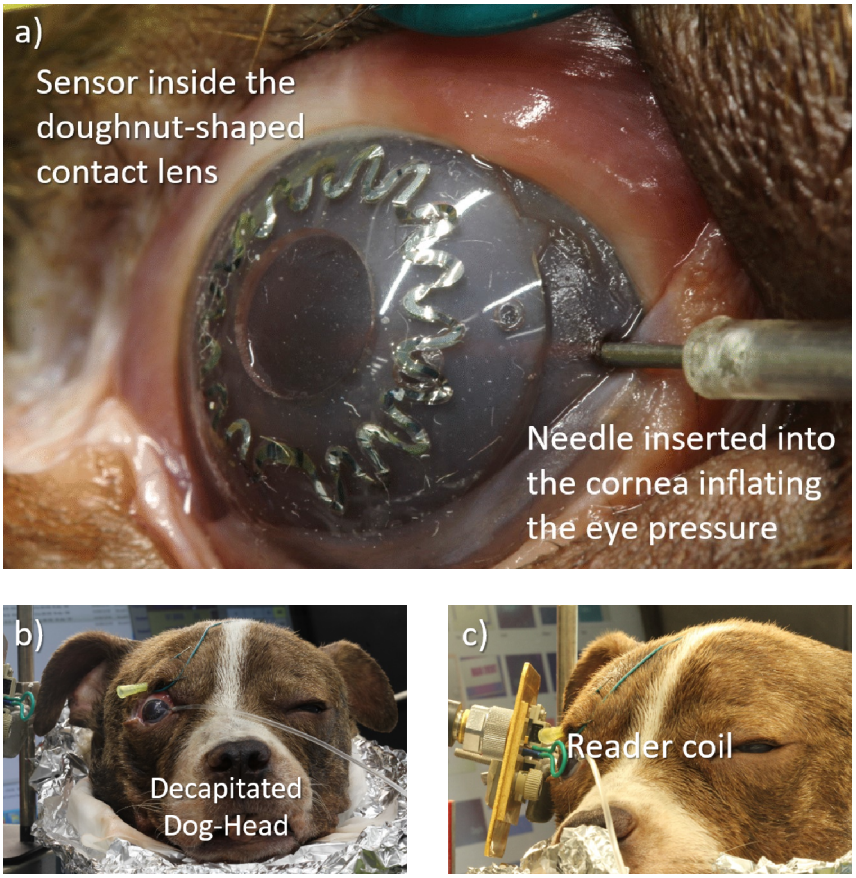

Figure 10. The setup for experimenting the ex vivo functionality of the contact lens on a dog's eye. a) The close-view of the eye and the needle that inflates the cornea with PBS. b) The front-view of the dog-head and its orientation with regard to the reader coil and inflating tubes. c) The side-view of the dog-head and its close placement next to the reader coil attached to the impedance analyzer pad.

2.2.8 Testing the humidity and temperature effect

Devices were tested inside a closed chamber on hot plate for testing their dependence on change in humidity and temperature. To conduct this experiment we used a commercial digital humidity and temperature sensor and sealed it inside a 200mL beaker next to the

device. The beaker was filled with DI water at the bottom so that raising the temperature of the hot plate would begin to raise the temperature of the steam inside the sealed beaker while it also increases the relative humidity. The setup is depicted in Fig. 11.

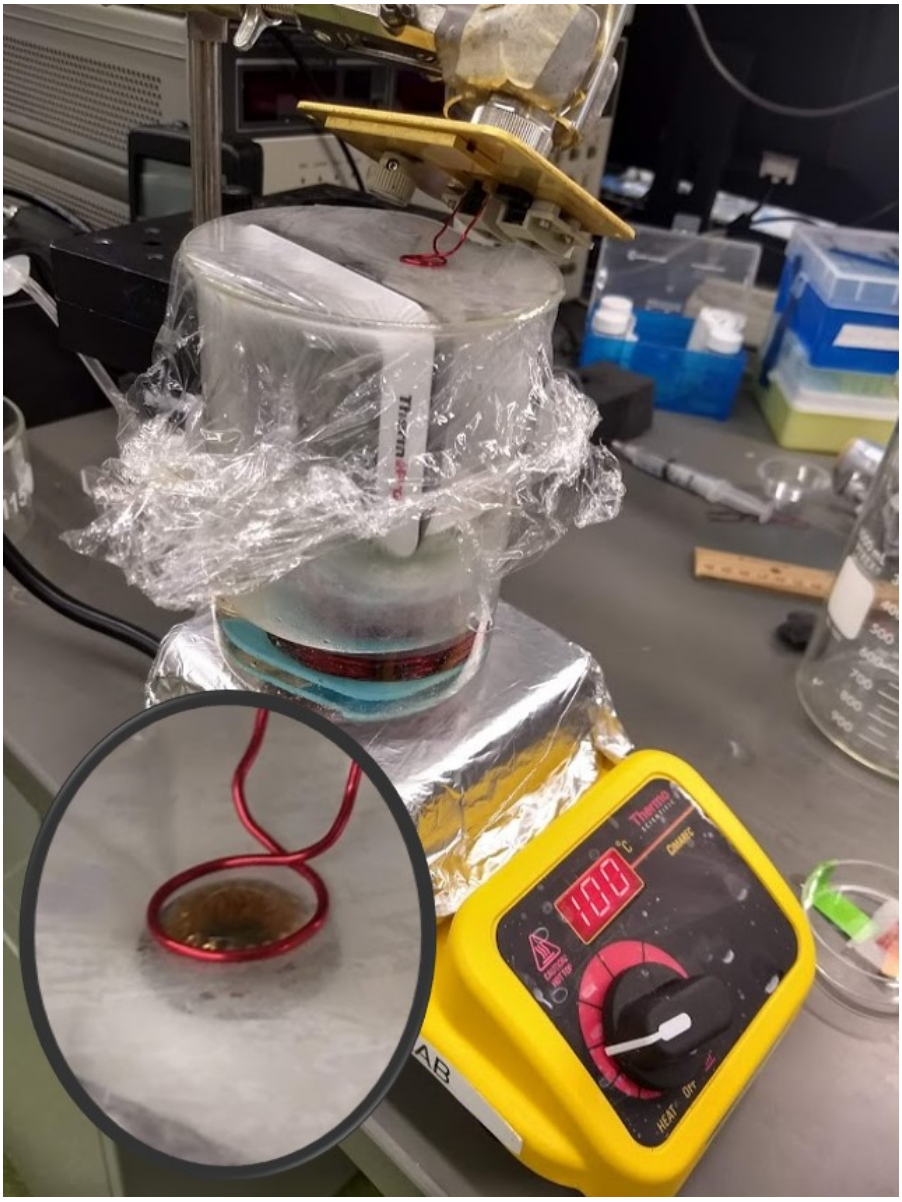

Figure 11. The experiment in which the effect of humidity and temperature were studied on the shift in the baseline of the sensor's response. The zoomed-in view shows the device on top of the beaker underneath the sealing plastic wrap, while the reader-coil is sitting outside the sealed environment and reads the resonance frequency.

The above setup worked well in controlling the relative humidity but the temperature was not controlled as well, therefore, we decided to separate the two parameters for better control and created another setup separately for testing the effect of temperature on the device's resonance frequency. Fig. 12 shows the setup for testing the effect of temperature at a constant humidity. The exact temperature of the device was recorded using a laser thermometer.

Figure 12. The testing setup for observing the effect of change temperature on the baseline resonance frequency of the device at a constant relative humidity.

2.2.9 Rethinking the design: improving responsivity and conformity

To investigate other polymers, hydroxyethyl methacrylate (HEMA) is one strong candidate as a targeted material to be tested as the mechanical support (contact lens) replacing PDMS for the betterment of permeability and user comfort. Earlier we discussed an article [46] that presented capacitive circular plates to harvest mechanical strain on the cornea. In that project they use HEMA as the polymer of choice for their soft contact lens. They claim it improves edge configuration, compliance, and comfort for the user. We plan on trying out this process and material for our contact lens integration with sensor and compare the results with PDMS devices.

We conducted an incorporation of the pressure sensor inside a much thinner contact lens made out of HEMA. This case is a whole, complete contact lens and does not have a hole punched in the center of the lens that was shown previously. The results show promising response while being tested on a rabbit eye *ex vivo.* Fig. 13 shows the setup, the device on a decapitated rabbit eye while it is pressurized using a syringe and a needle inserted into the cornea. Results show impressive improvement compared with the doughnut-shaped lens that were previously tested on decapitated dog eye. This significant improvement can be justified mostly with the much thinner lens that is conforming well to the rabbit eye and responds to the changes in the curvature of the cornea of the rabbit eye. It can also be due to the responsivity of the rabbit eye we use in this experiment compared with the dog eye. It is not possible to quantify these changes at this point and what we can control is the device, its flexibility and conformity to the eye under test. Ideally a comparison of the

different devices on similar eyes can be done for better comparing and separating the elements for further development.

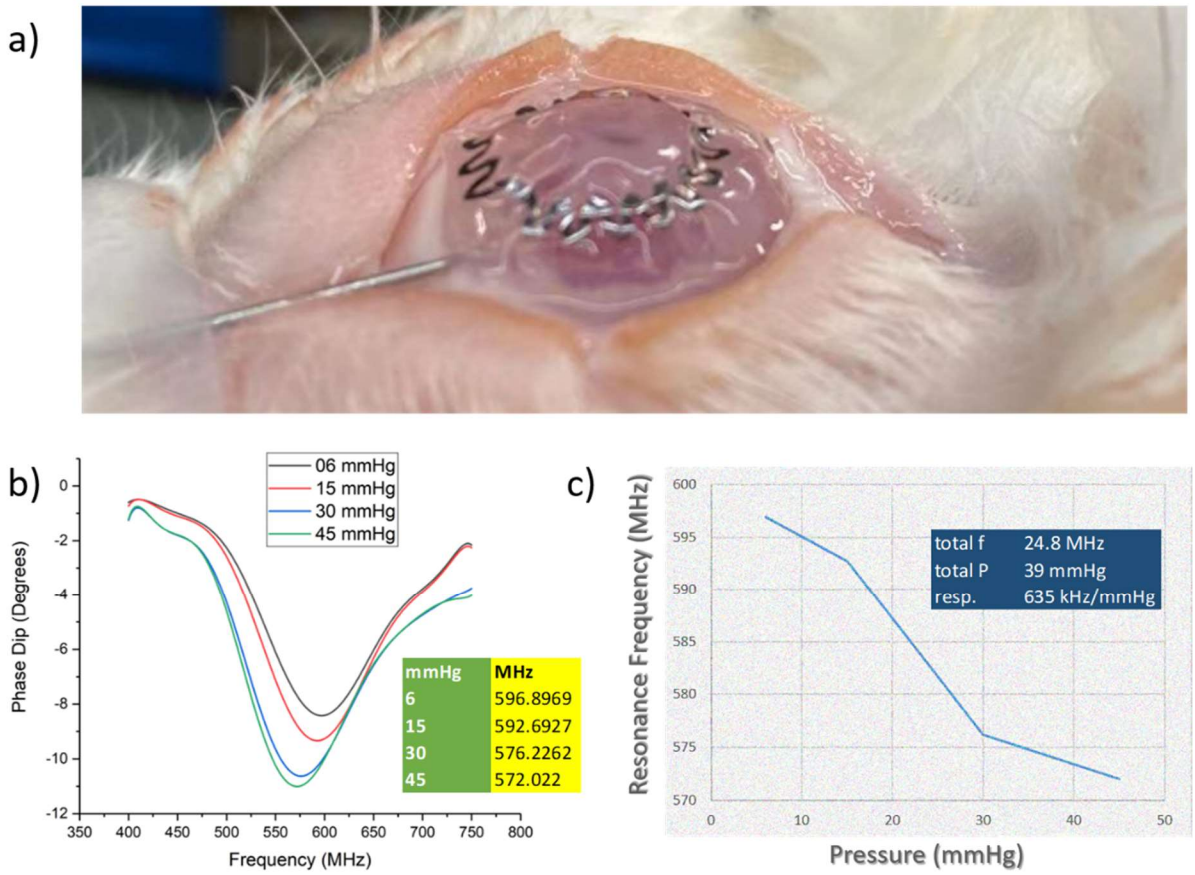

Figure 13. Test setup and results for ultra-thin HEMA lens with pressure sensor inside. a) side-view of the *ex vivo* experiment on rabbit eye. b) The resonance frequency of the device at different eye pressure points and the corresponding frequency shift. c) The shift in resonance frequency with respect to the applied eye pressure during the experiment.

2.2.10 Fabrication and testing of devices with different geometries

Eyes differ in size and the location at which maximum strain occurs changes. Therefore, for maintaining maximum harvest of the strain that can result in maximum sensitivity if the overall sensor demands an adaptation of the original size of the sensor to the change

in the size of the eye. Ideally, one might expect a personalized scanning procedure performed on each individual eye prior to device fabrication in order to obtain precise geometrical profile and design accordingly. However, that level of precision could be a concern at commercialization stages which is beyond the scope of this dissertation and for practical reasons here we exercise a couple different sizes of sensors. In order to place the sensor closer to the corneoscleral junction we are planning to make at least one or two larger sizes of devices and characterize them and compare the results. We project that the sensitivity of the larger devices will also be significantly higher. The masks used for the smaller (Design-E) and bigger (Design-F) devices are juxtaposed in Fig. 14. Each of them shows a stacked view of 4 masks on top of each other corresponding to 4 different photolithography steps in their microfabrication.

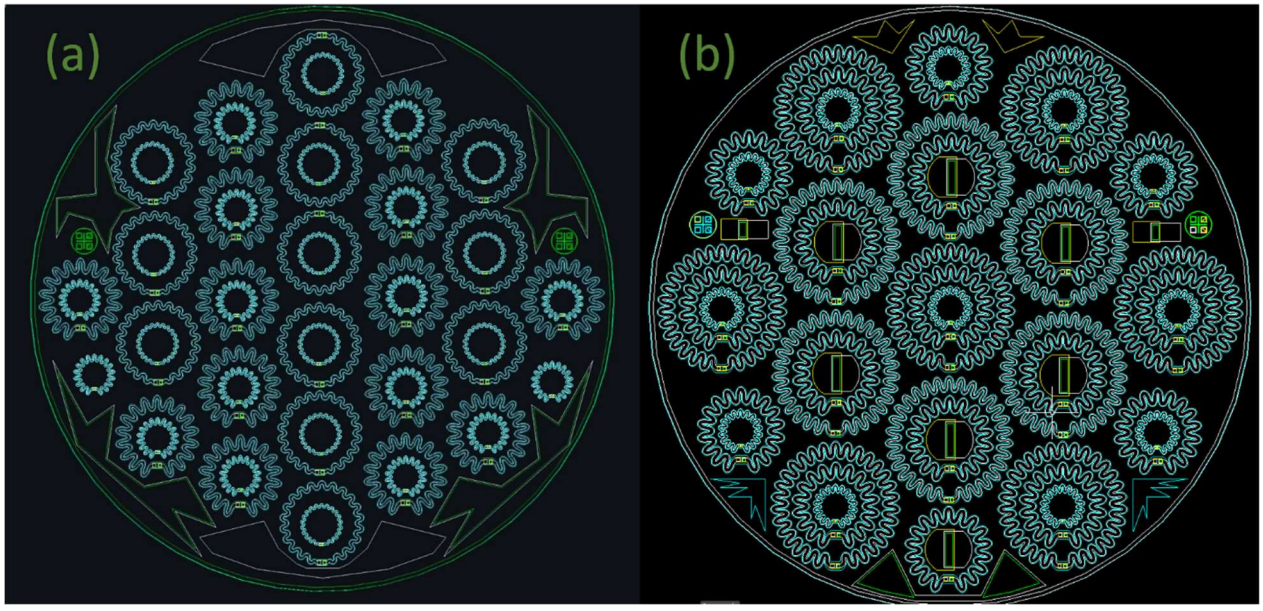

Figure 14. Mask design of the single-turn sensors consisting of four separate masks each. a) Design E: Previous design that was made, tested, and presented on the dog eye. b) Design F: Larger devices with bigger coils for further testing.

Also, from photos taken continuously from enucleated pig eyes, it is observed from the eye's mechanical behavior that change in IOP mostly shifts the central tip of cornea outwards and the radius of curvature in fact decreases with higher IOP. Therefore, most of the mechanical strain takes place in the form of vertical displacement peaking at the central part of cornea. Even though the corneoscleral junction is where the change in the angle of the cornea with respect to the sclera happens, however, a more complex conformal network of strain sensing mesh spread all over the cornea could potentially increase the sensitivity by orders of magnitude. Using more complex mesh designs of strain harvesting geometries it may also be possible to achieve higher self-inductances that may also potentially increase the telemetry range significantly.

Previously, some of these multi-turn designs were microfabricated and tested on some enucleated eyes. Unfortunately, the flat design made out of surface micromachining and lithography of thin films showed the appearance of major wrinkles once the sensors were peeled off the flat substrate and placed on the curved pig eyes. For continuation of these devices, we suggest fabricating the devices using 3-D printing methods on curved surfaces as the substrate. In that case, the devices won't wrinkle when they are placed on eyes and maintain their designed shape and conformity. Fig. 15 shows the mask we used for creating these multi-turn devices and their placement on enucleated pig eyes.

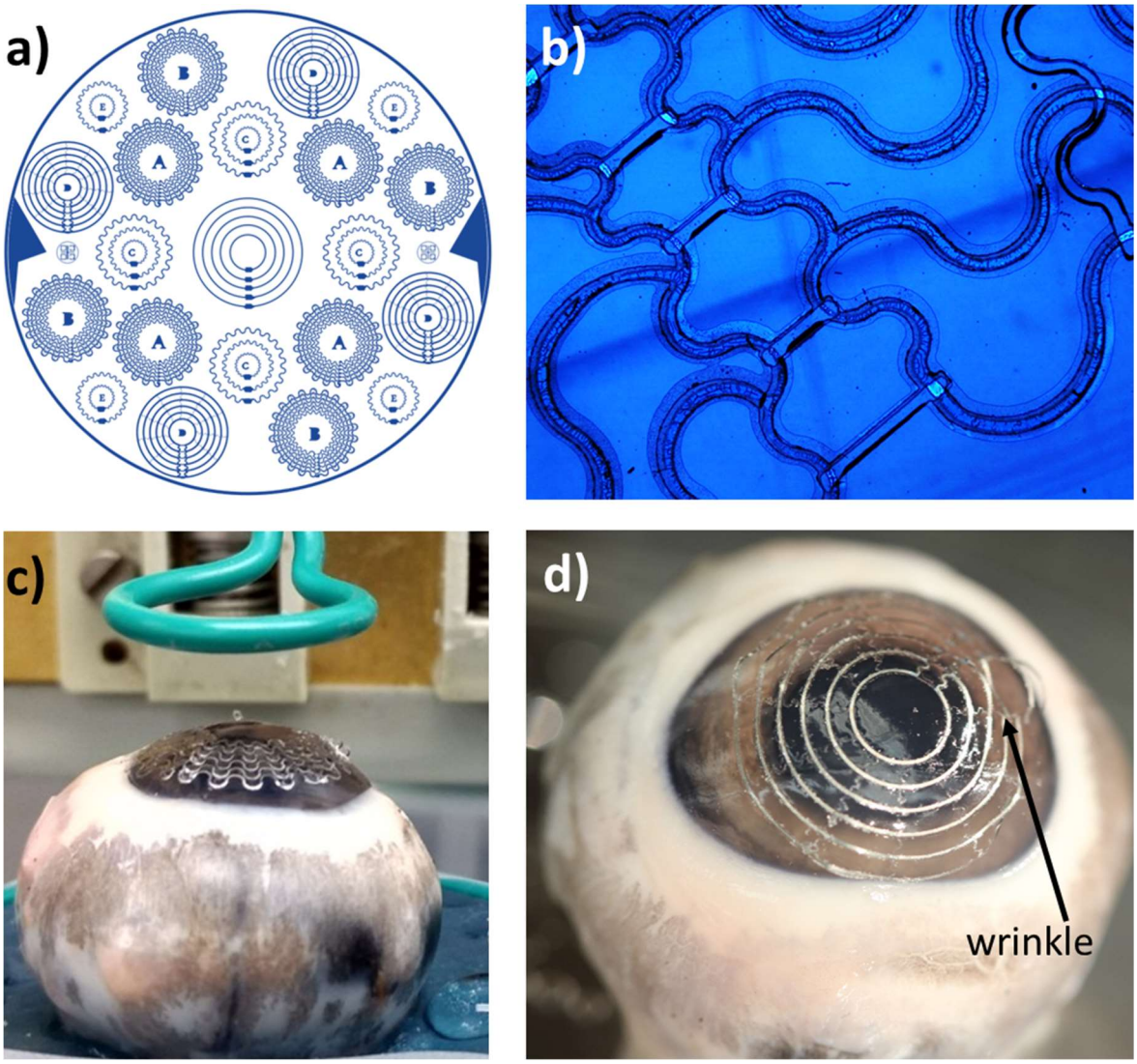

Figure 15. Multi-turn sensors fabricated using thin film micromachining and photolithography. a) The photo mask for lithography of the sensors. b) A micrograph showing a part of a fabricated device. c) A fabricated device (Labeled as A in the photo Mask) placed on a pig-eye. d) Another design (Labeled as D in the photo Mask) fabricated and placed on pig eye.

There are other designs, however, that have suggested geometries that could reduce or eliminate wrinkles. However, due to the variability of each eye and complexity of the 3D shape of cornea wrinkles might be inevitable while a geometry is made in a flat substrate out of brittle materials and is transferred for conforming to 3D domes.

2.2.11 Clover-shaped contact lens

We suspect the full encapsulation of the stretchable wire inside PDMS or HEMA contact lens may limit the responsivity. To test this idea, we designed special molds that yield to contact lenses that look like a clover leave (See Fig. 16) This approach leaves three or four portions of the stretchable wire outside the contact lens such that they are floating in air and when the device is placed on the eye the stretchable wire that is coated with Parylene-C and sits outside the PDMS contact lens directly contacts the eye tissue and responds.

The idea is that the extended clover arms of the lens would move outwards when the curvature of the cornea increases and the floating parts in between the arms would stretch easier and faster than the parts that are inside the arms. This may allow the overall diameter of the device increase easier with higher responsivity. To put this idea in tests we created those special molds that yield clover-shaped lenses (Fig. 17-b) while the relatively thin PDMS is poured on top of a device that is placed on the mold. These mold would have three or four stoppers in the interior side of the device so that when PDMS is poured the parts of the device that is placed behind the stoppers would not have any PDMS on them so that they release in air when the lens that is dried out is released from the mold.

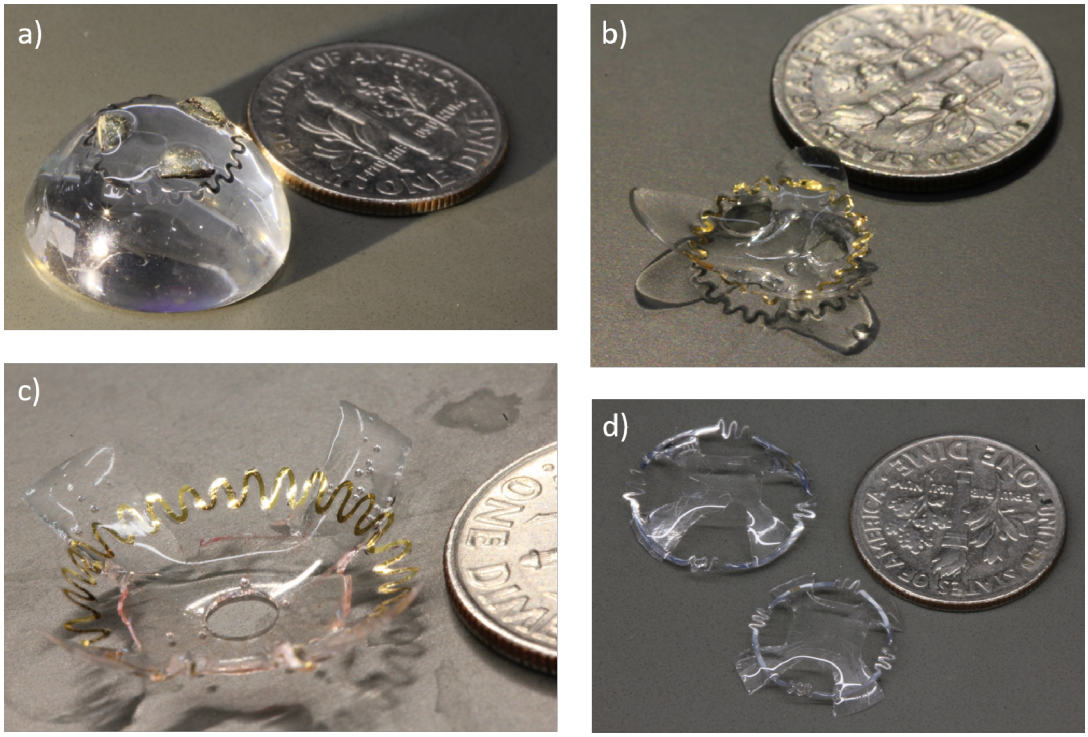

Figure 16. The clover-shaped contact lenses made using pour-over molds. a) The glass half-sphere bead that is modified with drops of epoxy to act as stopper for pour-over process. b) A clover contact lens device with three arms. c) A clover contact lens with four arms and a large device with full stretchability. d) The clover contact lenses with four clover arms and devices that have partial straight parts where device gets encapsulated.

To better advance and take advantage of this design feature, we also fabricated devices that are not stretchable in certain parts that get encapsulated inside the extended arms of the clover contact lenses. It is projected that this can help the device to better conform to the eye and the strains applied by the change in the pressure better be transferred to the stretchable areas of the device that are also outside PDMS.

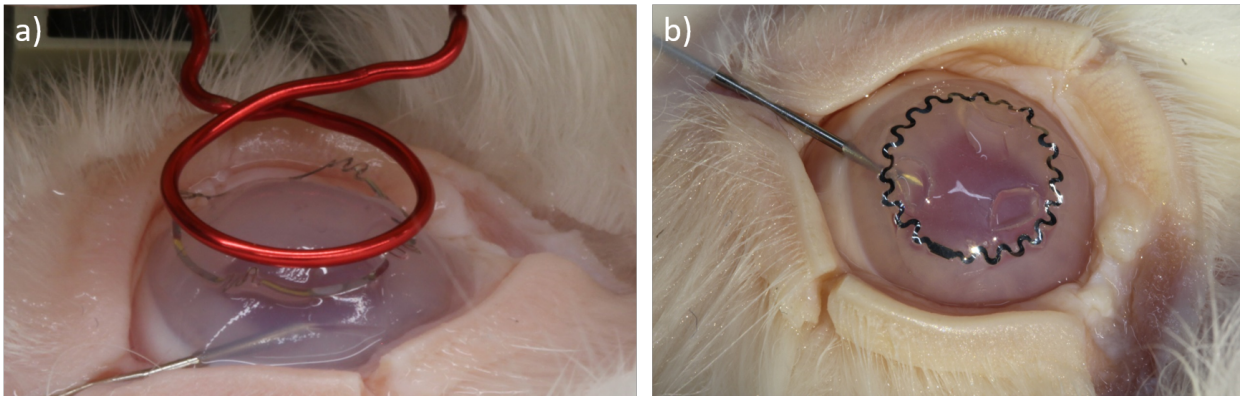

Figure 17. The clover contact lenses placed on post-mortem decapitated rabbit eyes for ex vivo testing. a) A partially stretchable device inside a four-arm clover contact lens. b) A fully stretchable device inside a three-arm clover contact lens.

Fig. 18 shows the placement of the clover-shaped contact lenses with devices integrated with them. Due to the stress profile of the thin film devices we observed that partially floating devices (Fig. 17-a) do not conform uniformly to a point that testing experiments yielded no reliable pressure reading with the current arrangement. Neither the fully stretchable device inside the clover lens showed any promising pressure reading response with the current arrangement and device dimensions (Fig. 17-b). The mold for pouring the PDMS over the device to create the clover-shaped devices were initially made out of a commercial contact lens case with parts that were cut out so the PDMS would not reach the device. This plastic mold (Fig. 18) was used to create the devices that are shown in Fig. 16-c and Fig. 16-d.

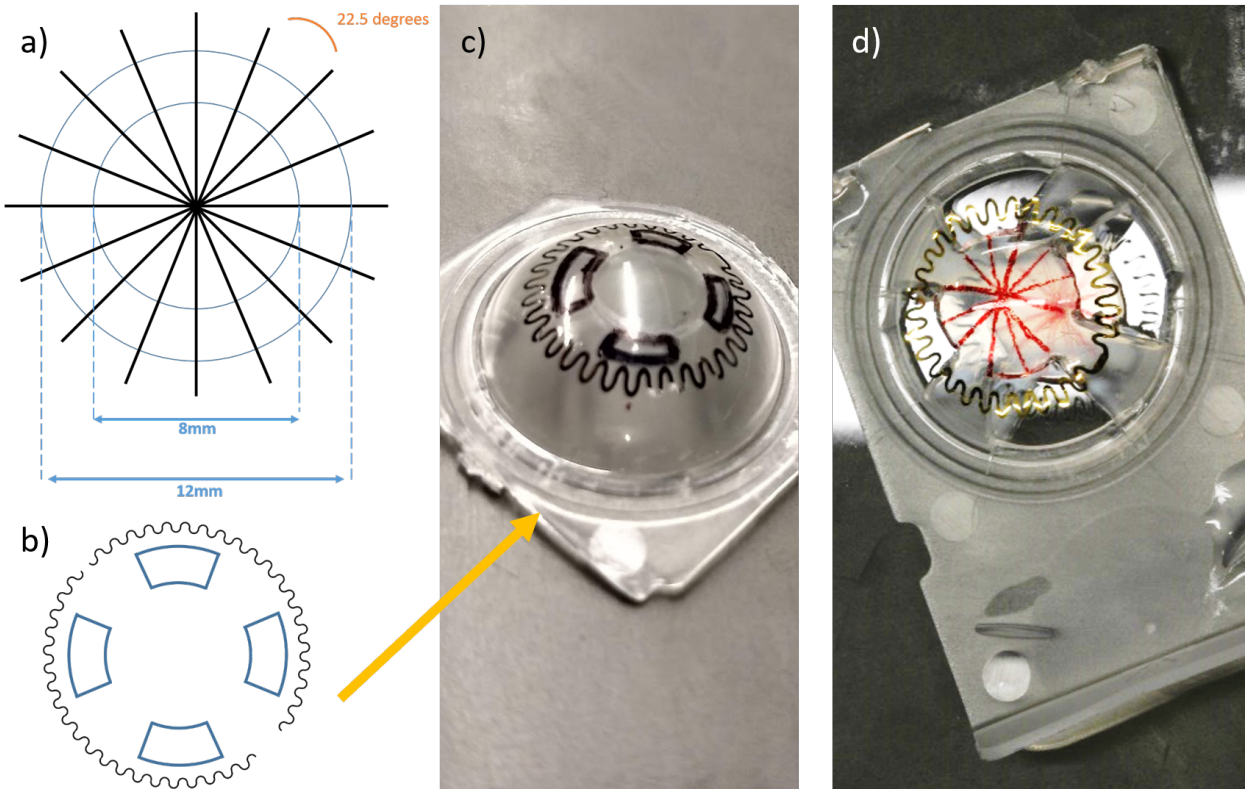

Figure 18. The plastic mold used for creating clover-shaped contact lens devices. a) The symmetrical slicing of the mold into double-sections of 45 degrees as parts that are cut into the plastic mold for creating devices with the partial floating stretchable wire. b) The final spacing of the hollow parts cut into the plastic mold. c) The marking of the plastic mold as designed. d) The produced mold with hollow parts and the placing of the device before the PDMS is poured onto it.

2.2.12 Electrical resistance

It took our design several iteration to come together as optimum dimensions and geometry for the length of the stretchable wire and its on-chip capacitor. Most importantly, while designing the stretchable wire it is vital to keep the overall electrical resistance of the wire lower than a certain amount depending on the electrical inductance and electrical capacitance of the total RLC circuit that is created with the device. The equation we used for modelling the electrical resistance (Eq. IV) of the stretchable wire depends on the

conductivity of the material and the dimensions of the wire. If the resistance is low enough it doesn't really play a big role in defining the resonance frequency.

2.2.13 Computer aided simulation

The mechanical behavior of the eye in response to IOP elevation has not been precisely modeled yet. The prior crude assumption of modeling an eye as a symmetrical and spherical balloon filled with liquid consisting only one or two layers of elastic shell obviously does not offer an accurate model that a highly-responsive strain sensor could be designed for. Therefore, it can be significantly beneficial if a computer aided model is generated with biological specifics associated with various tissues and organelles inside the eye and the effect of IOP and its resulting mechanical strain is simulated. A 2D model would perhaps be the first logical step towards that line of modeling. Next, it might be possible to run simulation on a model of the eye in 3D with higher complexity using a super computer, possibly the one at the Cyber-Enabled Research (iCER) center at Michigan State University. In regular settings COMSOL would be the software of choice in these simulations. However, these simulations might not be feasible given the complexity of the eye and the limited functionality and sophistication of COMSOL running on regular servers with limited memory. Even though, this attempt may not be fully realized in this dissertation, it will be considered as a potentially desirable task and initial steps will be taken towards it.

Previously, two simulations were conducted. First, in order to find the mechanically weak points of the stretchable serpentine thin metal film and enhance the design to compensate

for those weak points. Based on the results, the inner bending parts of the wavy serpentine wire is shown to be the weakest points which can reduce the electrical conductivity significantly. Therefore, to address this effect, we increased the width of the wire by 50 percent in locations where the wire bends by 180 degrees. That enhancement worked very well and showed significant improvement in fabricated devices which their electrical conductivity was tested and measured after a few stretches and no significant loss or mechanical failure was observed. The results are shown in Fig. 19.

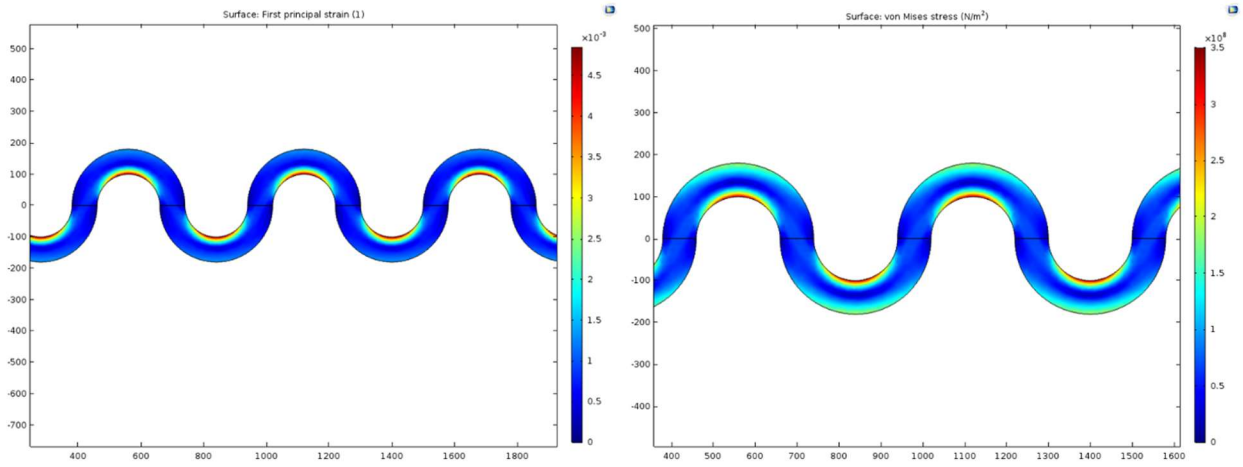

Figure 19. Surface Stress Profile on Serpentine Wire Simulated in COMSOL. Left: First principal stress. Right: Von Mises Stress.

Also some qualitative electromagnetic simulations were previously conducted to come up with an approximation for the value of the inductors and the shape and form of the electromagnetic flux density of the reader coil. The results are shown in the Fig. 20. The inductor values obtained from COMSOL helped to confirm the compliance of measured values of resonance frequency with theoretical equations.

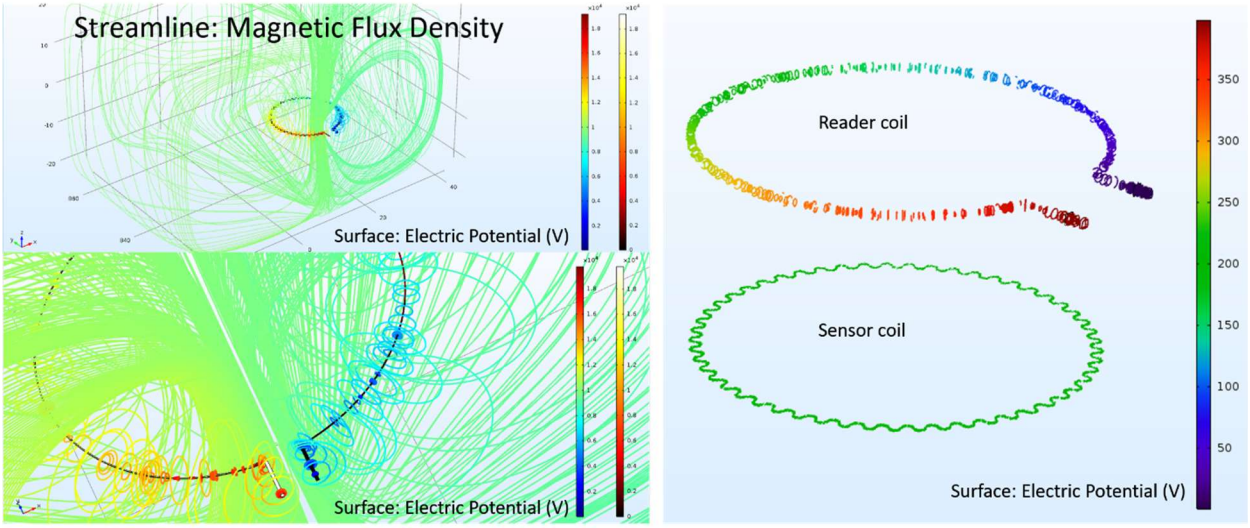

Figure 20. COMSOL simulations for reader and sensor coils. Left: Magnetic Flux density after applying an electric voltage to the terminals of the reader coil. Right: Reader coil and sensor coil in proximity.

Furthermore, electromagnetic simulations could be helpful in finding out the exact change of the inductance to simply verify with the experimental results obtained from PDMS membrane tests. So, a sensor coil would be ideally simulated in COMSOL in different stages of stretch with each having a specific area. These simulations are shown in Table 2 corresponding to their inductance values. As expected, it is observed that the larger the total diameter of the coil the larger the value of their inductance.

2.2.14 Automation of data collection and analysis

The previous procedure in collecting data from the sensor and its analysis is partially manual. We used a desktop impedance analyzer called HP 4191A. This machine obtained the impedance of a reader coil, selectively, in terms of magnitude and phase. The software controlled the impedance analyzer so that it swept the frequency at which impedance was measured at within a desirable window in which resonance frequency occurred. One file was generated as the outcome of that frequency sweep which was associated with a certain eye pressure. That eye pressure was read by the operator visually from the display of a hand-held pressure sensing device called Traceable® Pressure Meter by a company called Control Company. Then a few minutes later the eye pressure was inflated by infusing saline into the eye through the needle injected into the anterior chamber. Once the pressure was inflated and stabilized after a while, another set of measurement was triggered by the software and subsequently another file was generated.

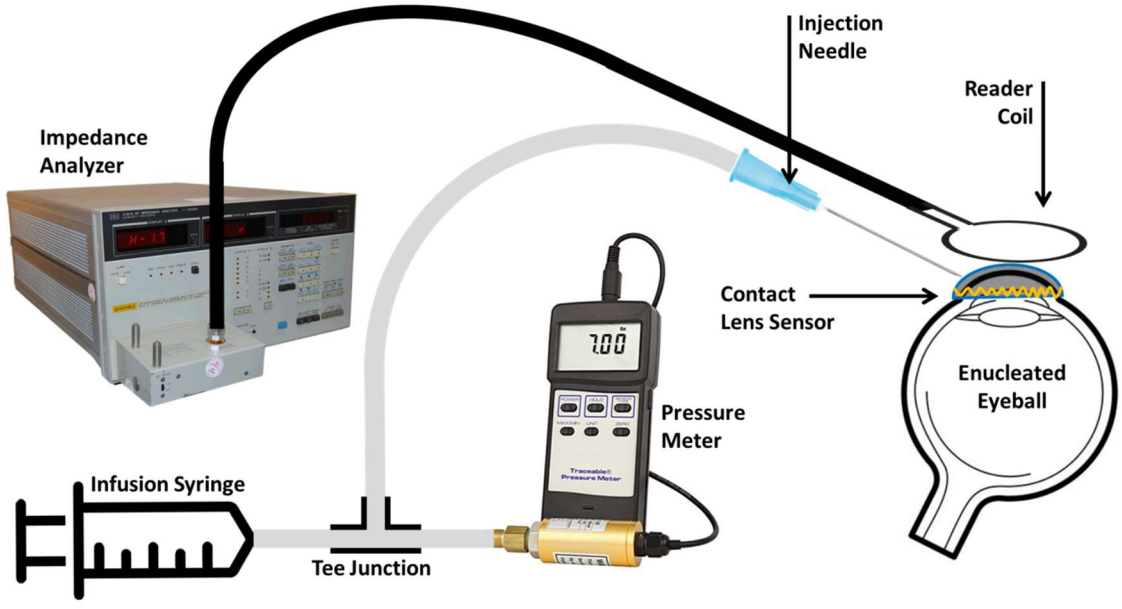

Figure 21. Characterization Setup Components- in vitro testing end.

A handful of these individual files were generated by changing the pressure of the eye for a handful number of times. Then these files were manually processed so that each of them suggested a minimum phase value at the peak of phase dip. That minimum phase value at the peak corresponded to a resonance frequency. The exact value of the phase was irrelevant, however, it was the frequency at which resonance occurred that offered relevant information. The number of data points at which phase was measured in a window of frequency cannot be too many because it takes a while for the machine to conduct one single set of measurement. Therefore, usually 60 to a 100 number of data points were taken with a typical step size of 5MHz. However, we needed much smaller step sizes in finding the subtle shifts in resonance frequency caused by IOP change. Therefore, either a curve fitting process or tracing interpolation was required to come up with those smaller step sizes. Previously, those mathematical processes were applied using a program called Origin Pro and frequency data was plotted versus pressure data. The resulting curve was what characterized the sensor, eventually, relating a shift in resonance frequency with change in IOP. The components of the characterization setup used in our experiments are shown in Fig. 21.

Figure 22. Characterization Setup Components: user-interface-end with the currently being used excel application.

2.2.15 Fully automated data collection: interfacing Microsoft Excel with Matlab

As part of this thesis, we also wrote a program to automate the above procedure a bit further in the same platform (in Excel) and integrate it with Matlab for the automatic mathematical processing of the data. This process has made the characterization process closer to a plug-and-play process that can automatically measure the phase dip and resonance frequency at each of the pressure points with a certain setting that operator can set with the software interface as an input emphasizing how many times they want the measurement run with their desired amount of delay in between. Eventually, this software can also be used for automatic measurement of eye pressure through a handheld reader device or miniaturized chip inside a pair of glasses and have the final data sent to a mobile

display. Fig. 22 shows the reading circuitry connections and their configuration with the software.

An original Matlab code was created while the excel VBA code was slightly modified from the publicly available program that we initially were using. The goal of this program is to retrieve phase and frequency data from the inductively-coupled contact lens sensor at a specific eye pressure while being able to control the number of datasets gathered, along with a customizable delay between the data sets. This data then gets to be analyzed and fitted with a *trendline*, the *trendline* then being used to find the absolute minimum phase and its corresponding resonance frequency at that given eye pressure.

The excel portion takes data from the impedance analyzer and controls the number of datasets and the delay between the datasets. Once each dataset is collected it is published as a .csv file titled with the exact timestamp, and then saved into the designated folder address. Folder address was able to be set by the original code, and only needed to be set to the specifically designated folder that the Matlab code uses. When the collection of the dataset is completed, the Matlab code is to be run.

The Matlab code must be opened manually when all the desired .csv files are generated and stored into a designated folder. Folder location should be in the same location as the Matlab code's .m file. The folder for the .csv files is to be used in the code as the address. This address is default named ***csv*** in the code, but must be renamed to be identical to the .csv

folder name. Once this is complete, the .m file can be run. The code goes through all the csv files present in the .csv folder one by one. Each csv file goes through the following process. The csv is read and stored into a table, the table of frequencies are stored into a vector X, and phases into a vector y. Curve fitting functions from the Matlab "Curve Fitting Toolbox" are employed as the fittest trendline.

Functions used for fitting from this toolbox are in order: Polynomial 7th degree, Fourier 2, Fourier 3, Spline, and Gaussian 2. Each fit uses the X and Y vector, and is then plotted on a generated scatterplot of the X and Y data. The figure holding the plot is titled the name of the csv file for ease of identification. Error information such as Sum of Squares Due to Error, Adjusted R-Squared, and Root Mean Squared are found for each fit type, and this data is labeled and stored in a table called "*ErrorReport*" for reference at the end. Each fit is then sampled on a much higher resolution frequency vector called HFV. HFV is created based on the original frequency data's minimum and maximum value, expanded to 1000 times resolution. The smallest phase value is identified from the sampled fit, and its index is used to find the associated frequency in HFV. The frequency from each fit is then stored into a final table called "*MinPhaseFreqsMHz*". This table has 5 rows, each row being a different fit function used, in the order of the functions stated above. All data in each row is generated using that row's labeled fit. Each column is a different csv, and is in the order of file number. The first file will be the top file in the csv folder, the second file the second file from the top, and so on. The table is then displayed, and after the error reference table is displayed, having the same structural rules as the first. The code returns to the address

specified at the end, which should be the original location of the .m file. The Matlab code is shared in Appendix-1.

The new Matlab code along with the modified excel file accomplish the task of retrieving a vector of frequencies associated with the minimum-phases (resonance frequencies), each associated with a dataset. Any number of datasets can be used, but larger quantities take longer to compute. Multiple curve-fitting equations are used with error indicators stored to be compared, offering the option of determining the most accurate fitting method to select the most accurate resulting frequency. Currently, the order is based on the order of the csv files in the designated folder, and each frequency column in the table is labeled to the file number, 1 being the first .csv file in the csv folder. One would need to know the order of the csv files in the folder to determine the order of the frequencies, but as file storage into the csv folder is set to be time-ordered, frequency columns should be time-ordered as well. The program goes through all files in the folder and will not delete any at any time, meaning if a certain time range is desired, the folder must be ordered to only have that time range by removing all other files. Further work to be done could be an error-weighting system, to identify automatically the approximate best fitting method for producing the most accurate frequency. Fig. 23 shows a screenshot from the newly modified excel program. The orange, blue, and yellow boxes along with the gray box showing 'RUN' are the new features that allow automatic collection of multiple datasets with certain number of recording points and certain values for the delay between each dataset.

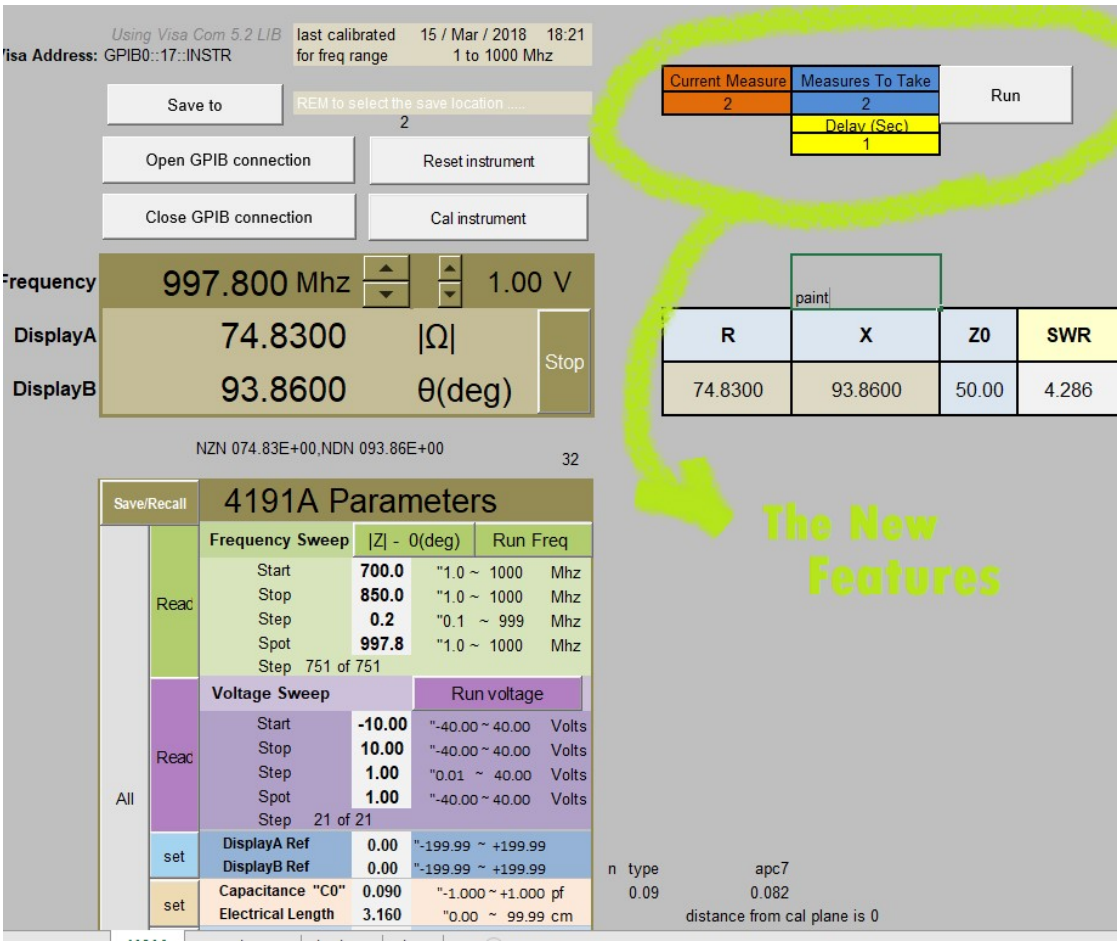

Figure 23. The new outlook of the modified Excel code that runs on the PC that the impedance analyzer is connected to.

2.2.16 Handheld reader electronics: design and implementation

As part of this dissertation an attempt in designing a mobile or miniaturized impedance analyzer is at place. The motivation is to replace the giant HP 4191a with a smaller handheld or miniaturized chip to be placed in a pair of glasses. This attempt may not be fully realized and/or be physically implemented during this dissertation; however, a preliminary literature research and design suggestions will pave the way for future investigators.

According to an article published by researchers in China [82], the impedance analysis methods vary in their settings, more importantly, in their signal-to-noise ratio (SNR). They compare their proposed method called Differential Method with two main standard methods called I-V Method and Auto-Balancing Method. We plan on simulating these methods in ADS (Advanced Design Software) and be able to tweak the values to achieve higher frequencies and reach our desired range (500 MHz) and employ this method in our impedance analyzer circuit. These methods are applied on the transduction circuit, where device under test (DUT) is being read with reference to a reference impedance.

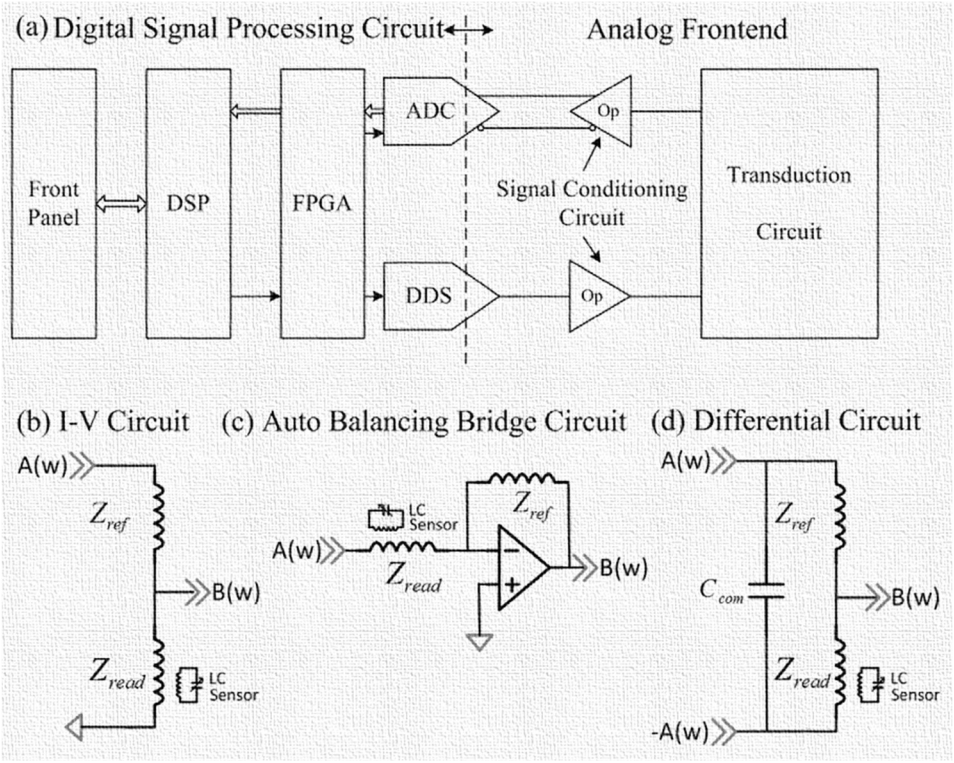

Figure 24. a) Schematic of the readout circuit and digital signal processing circuit. b) I-V circuit, c) Auto balancing bridge circuit, d) Differential circuit [82].

In their DSP portion they use a TMS320VC5509A for their DSP chip, a Spartan 6 XC6SLX9 for FPGA (field-programmable gate array), an AD5930 for DDS (Direct Digital Synthesis), and AD9266 for their ADC (Analog to Digital Converter). These products of choice are good for the working frequency of 130 kHz as the central resonance frequency. However, for our application we need to work in much higher frequencies in the range of 500MHz. That would require to follow similar modular design as discussed above, but, perhaps with alternative individual chips that could exceed the frequency limitations that might be posed by the chips used in [82]. Fig. 24 shows the schematic diagram of some of the fundamental readout circuit models.

One major attempt in progress is to understand what limits the frequency most. Is it the natural limitation of controlling units and their internal sub-chip elements, or external clocks, interconnects or a combination of all? From there we can start to overcome those limitations and eventually reach a handheld and ideally miniaturized high frequency impedance analyzer.

As part of this project we outsourced the development of a handheld impedance analyzer so that the pressure sensor contact lenses can be tested on animal subjects. Previously we have been testing enucleated ways on bench-top equipment using an enormous HP 4191a impedance analyzer that cannot be easily moved or handled in animal experiment settings. Therefore, this is an imperative step before the contact lenses could be tested in live animal

experiments. The only hardware design inputs of the handheld impedance analyzer provided by us to in2being is the dimensions of the reader coil we use in reading the mutual inductance between the contact lens devices and the reader coil. As shown in Fig. 25, the dimensions of the reader coil we have been mostly using especially for the contact lens sensor that is 11mm in diameter, are 8cm in length of the wire and also 11mm in diameter. That is so because it is most effective when the reader coil and the contact lens sensor have the same diameter. A prototype version of the handheld impedance analyzer made by in2being Inc. which is made out of discrete, off-the-shelf, and commercially-available components is shown in Fig. 26. The dimensions of this device is about 7x4.5x2 inches.

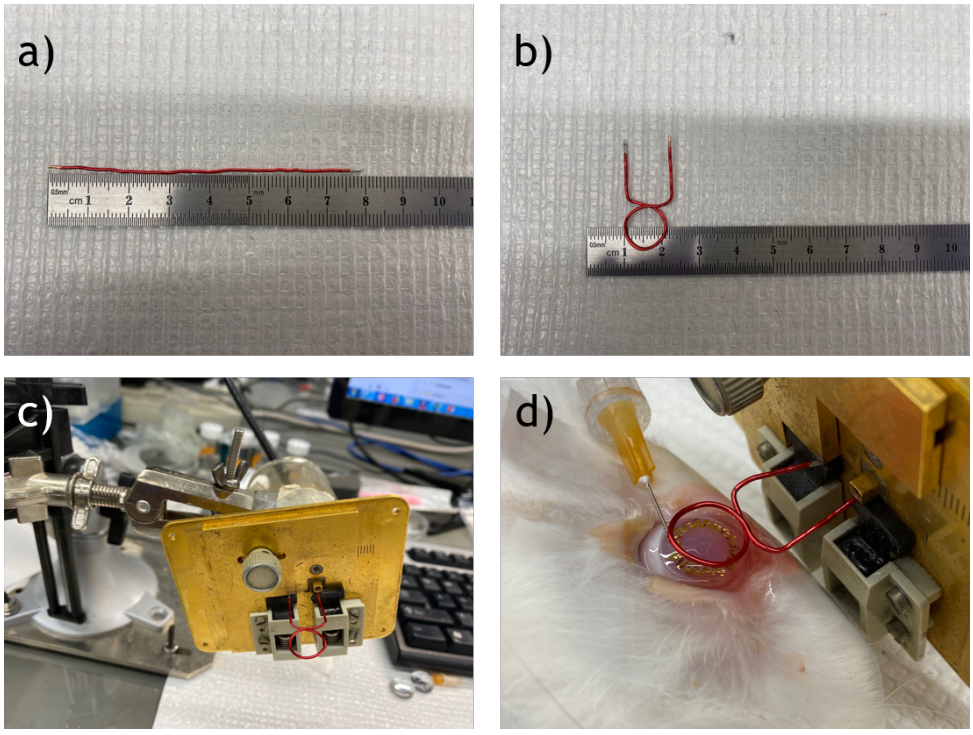

Figure 25. The dimensions of the reader coil used for our contact lenses with the diameter of 11mm. a) The length of the entire wire is 8cm. b) The diameter of the reader coil itself is shaped into 11mm to follow the same diameter of the contact lens sensor. c) The terminal pad of the bench-top impedance analyzer. d) The arrangement of the reader coil while being used to pick-up the resonance frequency of the contact lens sensor.

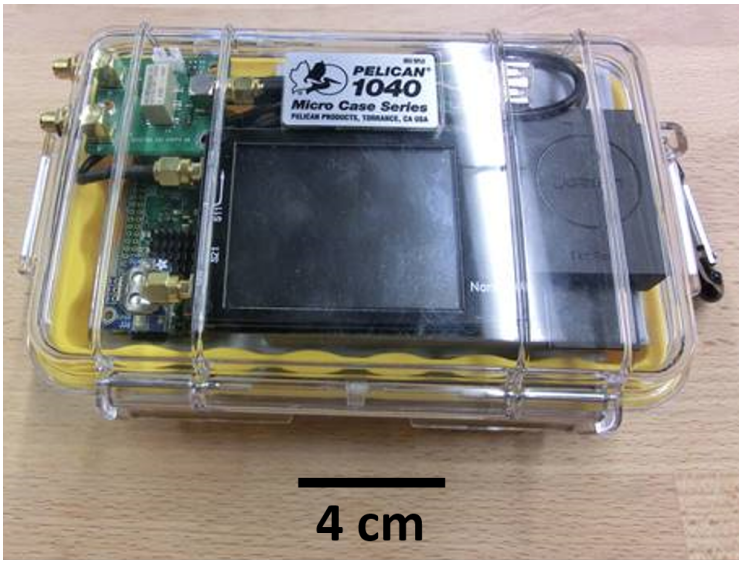

Figure 26. A semi-final view of the prototype handheld impedance analyzer created by in2being Inc. made out of off-the-shelf discrete and commercially available components to be used for live animal experiments and testing IOP sensors *in vivo*. The dimensions of this device is about 7x4.5x2 inches.

2.2.17 Three-dimensional printing and biomaterials

In this thesis we have relied on microfabrication for making the pressure sensors. Even though our design significantly simplifies the fabrication process, microfabrication is not the most-cost effective especially when market demands precision custom-made dimensions that may be hard to scale using conventional microfabrication processes. Therefore, with the motivation of increasing the mechanical robustness and simplifying the fabrication it may be worth investigating strategies for fabrication of sensors using printable conductive inks utilizing nozzle-based techniques on pre-fabricated dome-shaped contact lenses made out of either PDMS or HEMA. The conventional conductive inks are usually based on volatile solutions containing either metallic nanorods, conducting

polymer nanoparticles, graphene, or carbon nanotubes CNTs. These inks can sometimes be cytotoxic. That might necessitate careful packaging strategies to avoid their contact with the eye tissue.

Also, efforts in designing biologically-friendly conductive inks have been taken by some researchers. Formation and characterization of a specific bioactive electrically conductive ink is investigated by researchers at University of California in Los Angeles. They claimed in a recent report [90] that their proposed ink possesses cell-binding sites that allow easy interfacing with living tissues and organisms. Their ink is a hybrid of CNTs and deoxyribonucleic acid (DNA) as a natural surfactant and some other biomaterials. They present an enhanced cellular biocompatibility and bioactivity. Also these inks can be processed in low temperatures which enables the use of flexible and stretchable polymer substrates.

2.3 Results

Devices were microfabricated and integrated with custom-made contact lens as shown in Fig. 27. Fig. 27-a is a micrograph of the planar constant capacitor and junction point of the adjacent ends of the serpentine wire obtained using a polarizing microscope (Eclipse LV100, Nikon). Fig. 27-b is a photomicrograph of a capacitor being tested under the high voltage voltammogram. Fig. 27-c shows the sensor with a slight variation in the geometry encapsulated in the flexible doughnut-shaped contact lens made of PDMS next to a Roosevelt dime. Fig. 27-d shows a similar device with the original geometry. Fig. 27-e shows

a doughnut-shaped contact lens being stretched and carried in a user's hand. Fig. 27-f shows the device being tested on the canine eye. A needle is inserted into the eye's anterior chamber which infuses saline for pressure control. The green reader coil measures the frequency response from the sensor's resonance circuit.

The stretchable inductor wire has an average length of 65.4 mm, a thickness of 500 nm, and a minimum width of 245 μm, resulting in an overall theoretical DC resistance of 13 Ω (Eq. V). The DC resistance of five devices are measured and averaged at 14.2 Ω which is in good agreement with the theoretical value. With a plate area of 700 × 880 μm2, the capacitance of the microfabricated capacitor is measured to be around 4.3 pF, which is close to the theoretical value of 4 pF (Eq. III). Notably, the 2-μm-thick Parylene dielectric is able to withstand voltages up to 1000 V without breaking down. The Inductance of the coil at rest is theoretically calculated at 27.4 nH (Eq. IV) which is in good agreement with the value obtained from COMSOL simulation: 26.7 nH. Fig. 28-f demonstrates that the contact lens sensor can be placed conformally on the cornea of the canine eye and coupled to an external reader coil (in green).

2.3.1 In vitro canine eye and PDMS membrane experiments

The results from the bench-top characterizations of the sensor response to strain are reported in Table 2 and depicted in Fig. 28. During the measurements, a syringe infuses 5

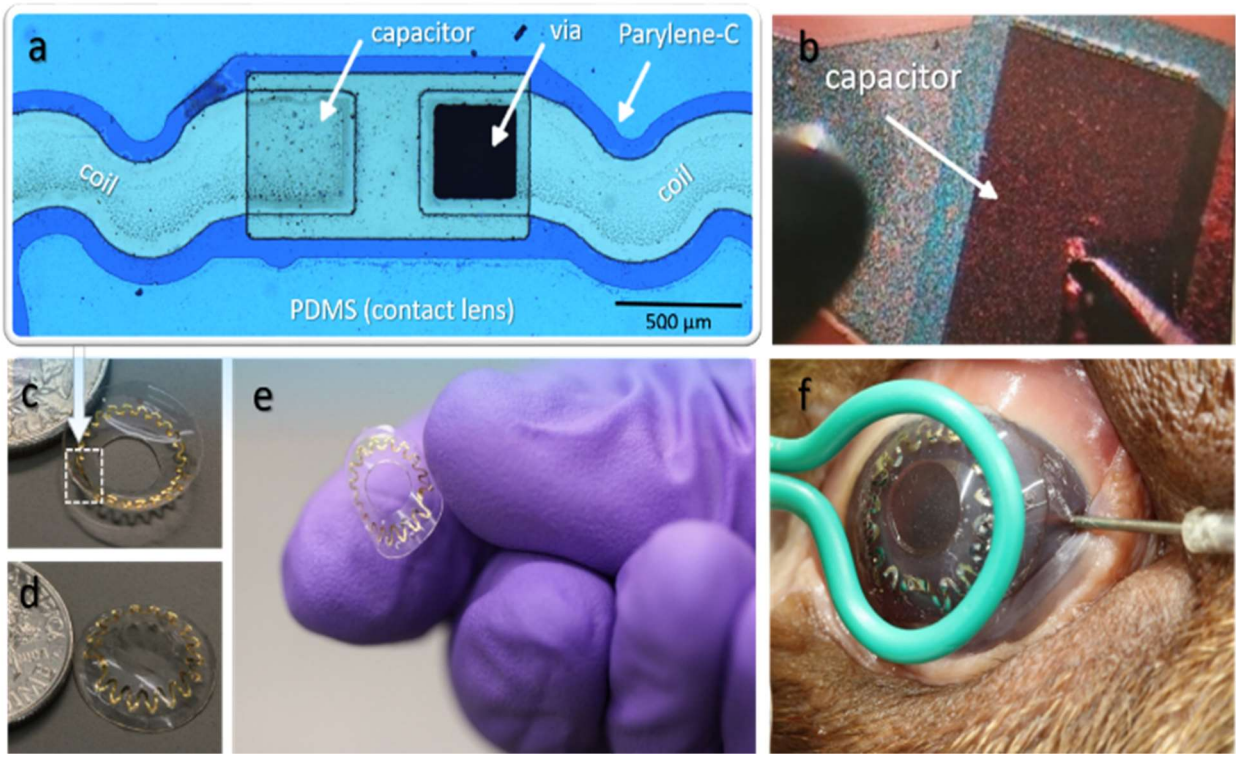

Figure 27. Fabricated devices. a) A microscopic image from the sensor's capacitor junction where the two ends of the coil meet and overlap. b) A microscopic view at the microfabricated capacitor while being tested under the high voltage cyclic voltammogram. c) The contact lens next to a Roosevelt dime (bottom-view) d) The contact lens next to a Roosevelt dime (top-view) e) The contact lens sensor held and flexed in a hand f) a look at the conformal placement of the contact lens sensor on the cornea of the canine eye.

ml of air into the chamber at each step and does that for three times, creating 4 different pressure points: 4.5 (no infusion), 13.5, 19.5, and 25.5 mmHg. The pressure increases in a nonlinear fashion since the PDMS membrane responds to the pressure in a nonlinear fashion. The radius curvature of the PDMS membrane at each step and the corresponded coil area are obtained using post-processing of the top-view images of Table 2 (first row) and complementary side-view images as illustrated in Fig. 28-a. The area of the coil loop increases proportionally with each step in pressure, illustrating the almost linear relationship between them, as presented in Fig. 28-b. A responsivity of 853 kHz per 1 mm change of the central radius of curvature is achieved on the PDMS membrane as shown in

Fig. 28-c. Using the four data points depicted in Table 2, we observed 34.4% of strain across a range of 18 MHz frequency shift. This relationship is almost linear with R-squared value

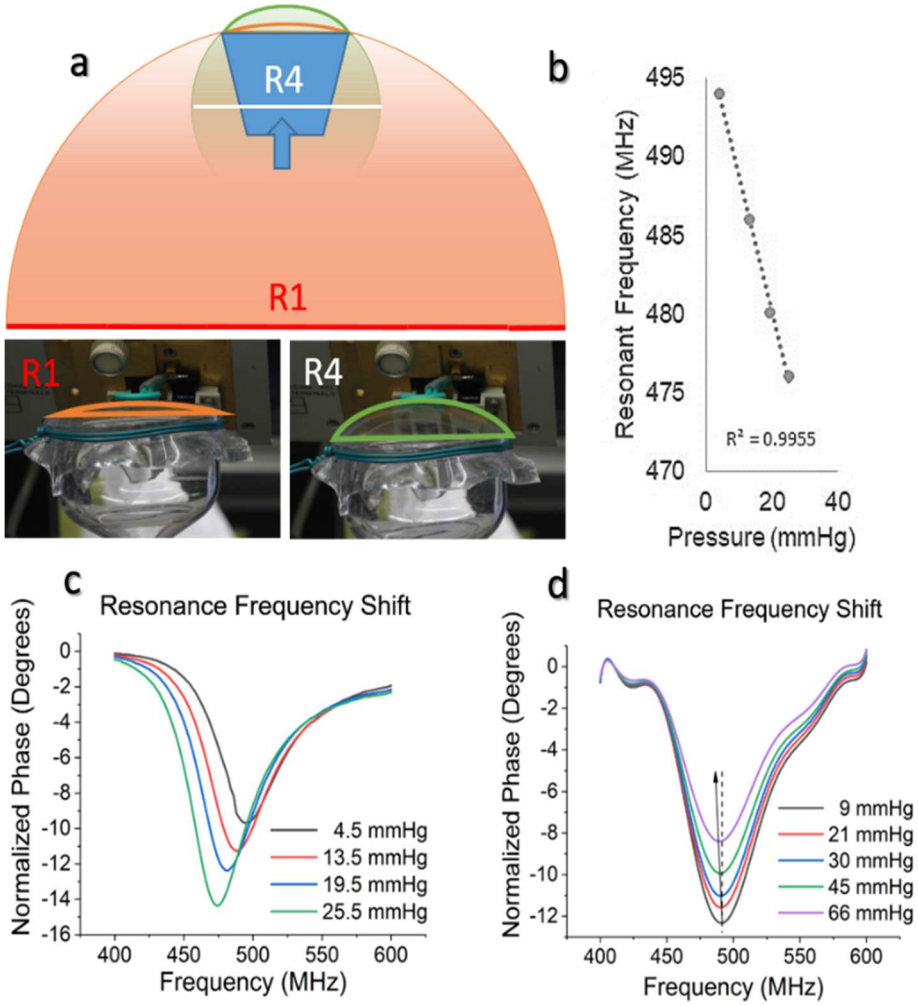

Figure 28. Bench-top and in vitro IOP measurements. a) The PDMS membrane testing apparatus: The radius of curvature (RC) changes from R1 to R4 when the rise in pressure deflects the membrane and lowers the RC. b) The linear relationship between the change in pressure and frequency response. c) The frequency response to the change of the central radius of curvature on the PDMS membrane. d) The resonance frequency shift caused by the induced change in the canine IOP in vitro.

of 0.9887. Using that linear relationship we calculate a final value of 523 kHz frequency shift per 1% of axial strain on the cornea.

Table 2. Results from bench-top measurements using the air chamber and the PDMS membrane setup.

State # (Experiment) ⇨	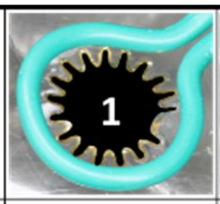	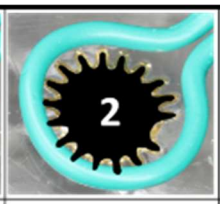	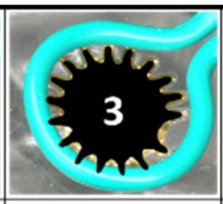	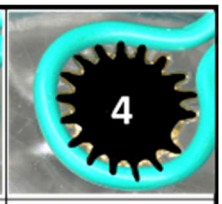
Coil's Inner Area (mm^2)	55.4	60.25	68.56	76.82
Resonance Frequency (MHz)	494	486	480	476
Applied Pressure (mmHg)	4.5	13.5	19.5	25.5
Radius of Curvature (mm)	82.3	73.3	64.5	61.2
Simulated Inductance (nH)	26.7	27.7	29.2	30.6
State # (Simulation) ⇨	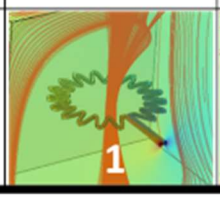	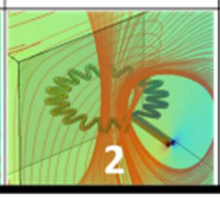	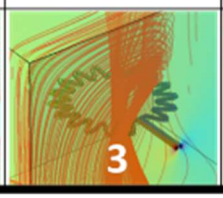	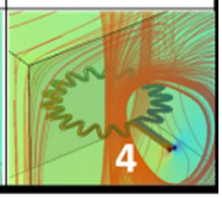

Fig. 28-d shows the in vitro measurement of the sensor responses, where a total downshift of 2 MHz in frequency is detected with a 59 mmHg increase in pressure. This leads to a responsivity of 44 kHz/mmHg for the doughnut-shaped PDMS lens sensor. It is important to note the limitations of our current testing results. First, the eye of the isolated canine head (in vitro) used in our trial was frozen for weeks and thawed right before the experiment. That could affect the cellular matrices of the tissue, weaken the resistivity of the tissue to stress, and amplify the successive strain. Second, the ocular rigidity and subsequently the biomechanical responsivity of the corneal and scleral tissue to IOP fluctuations differs significantly from in vitro to in vivo tissues [91]. Third, a previous study [92] showed that excised human eyes show a lower corneal hysteresis (therefore, higher responsivity to IOP) compared with intact living human eyes, which is important to

consider when comparing results from enucleated eyes versus intact eyes. Fourth, in another study [93], human corneas were shown to be significantly stiffer than porcine corneas, which could perhaps be the case if the porcine corneas are not necessarily much different from the canine. Our current design is specifically tailored to canine eyes. Different device geometries and materials are under investigation to accommodate individual eyes across diverse animal models and eventually various human patients.

2.3.2 The balloon experiment

Prior to the PDMS membrane experiment though, we conducted an experiment by placing a pressure sensor on an inflating balloon and then we poured PDMS on it so it sticks to the surface of the balloon and follows the curvature of the inflating surface closely and carefully. Fig. 29 shows the setup and the results. We obtained a 20MHz shift by changing the pressure in the balloon from 80 to 124 mmHg (a total of 44 mmHg pressure gradient). This experiment presented a device responsivity of 455 kHz/mmHg which is almost half the amount we obtained in the PDMS experiment. These two experiments were done on the same type of pressure sensing device with exactly the same geometry and dimensions. This shows how much the incorporation of the device has effect on the responsivity of the device, its method of utilization, its conformity to the surface, and most of all the pressure responsivity of the membrane itself which follows the stiffness of the material and its curvature of radius.

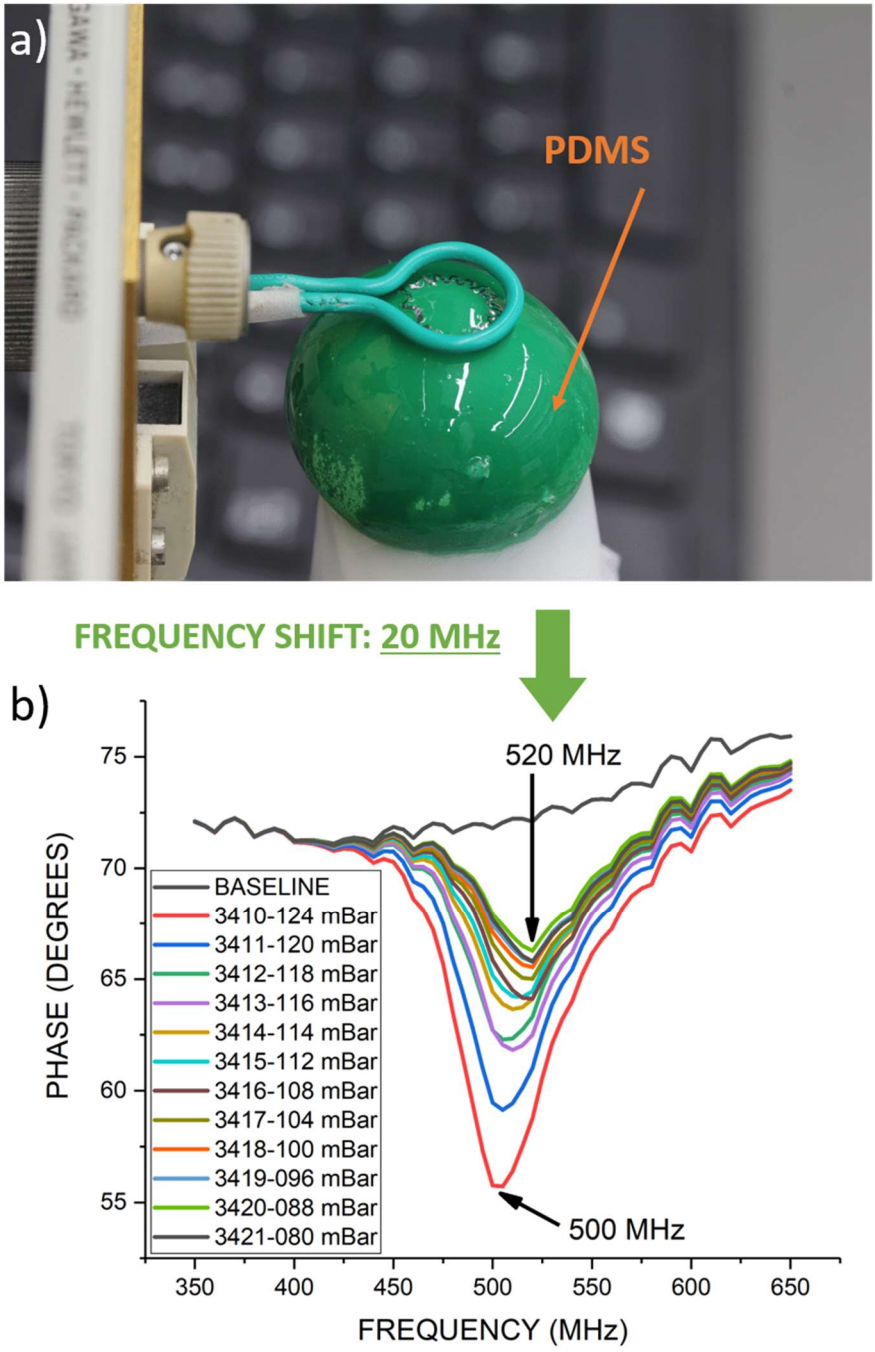

Figure 29. The balloon experiment. a) The setup showing the device placed on the inflated balloon and fixture to its surface using pour-over PDMS. b) The results showing the obtained shift due to change in pressure in the balloon and its effect on resonance-peak in terms of phase.

2.3.3 Large devices

Larger eyes ask for larger devices. Therefore, to see the effect and validate the feasibility and functionality of larger eyes we fabricated larger devices and tested on PDMS membranes. When devices get larger their stretchable wire gets longer therefore to keep the electrical resistance low enough, we also designed a large device that is thicker than usual so that we obtain sharper peaks with higher signal-to-noise ratio (SNR). Fig. 30 shows the fabricated devices on 3-inch wafer and their integration with thin PDMS contact lens.

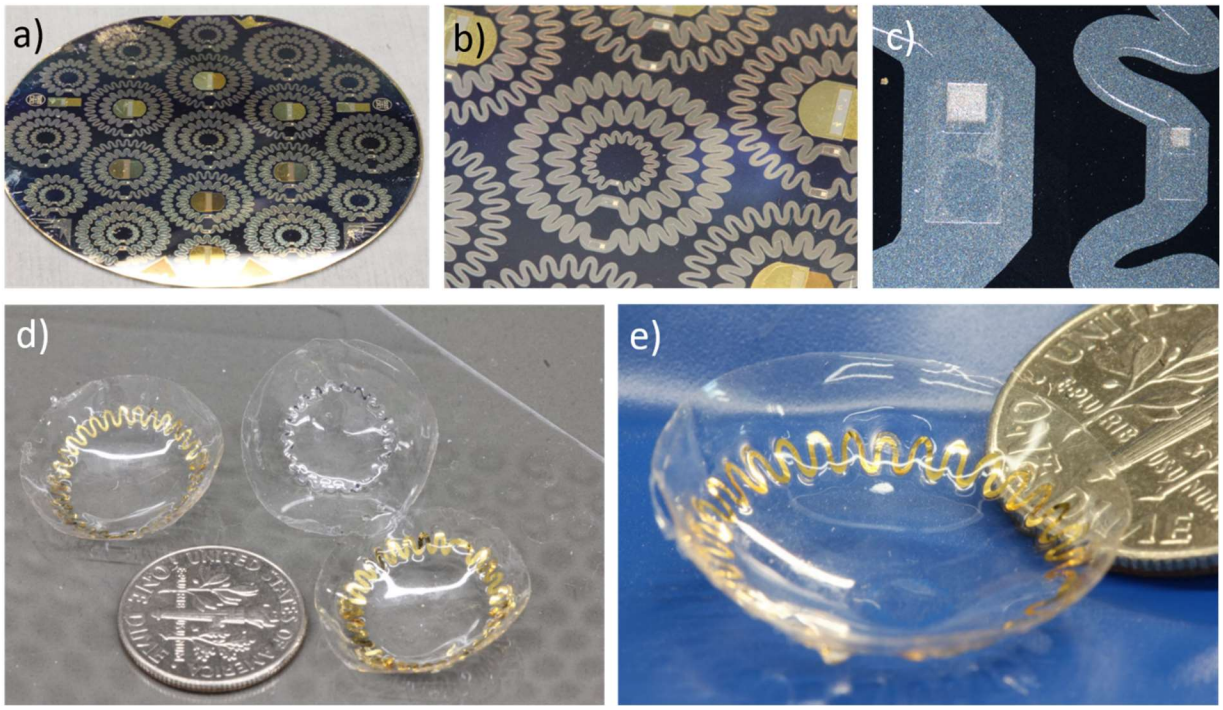

Figure 30. The fabricated large devices with two different width. a) The large devices fabricated on a 30inch silicon wafer. b) A closer view at the devices after they were fabricated. c) A microscopic view of the fabricated devices shows the capacitive junction with the aluminum mask on top for the final reactive ion etching of the Parylene-C. d) The fabricated devices after they were integrated with thin PDMS contact lens devices. The image shows to smaller device which was previously made and tested next to the large devices with original width (left) and the wider width (right). e) A closer view of the integrated device inside thin PDMS contact lens. This is a large device with the original width.

Fig. 31 shows the setup and the placement of the device from top-view (original width) and side-view (wider width) in three different pressure points.

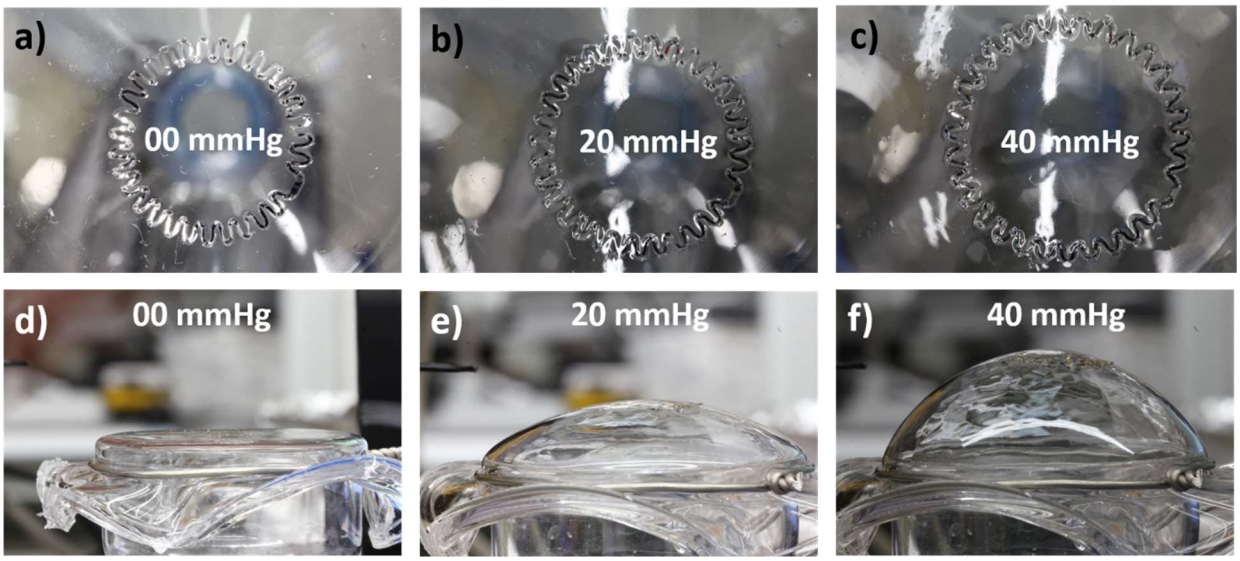

Figure 31. Three states of the PDMS membrane holding the pressure sensor devices inside. a) Top-view of the sensor at 0mmHg. b) Top-view of the sensor at 20mmHg. c) Top-view of the sensor at 40mmHg. d) Side-view of the PDMS membrane at 0mmHg. e) Side-view of the sensor at 20mmHg. f) Side-view of the sensor at 40 mmHg.

2.3.4 Miscellaneous effects

Fig. 32 shows the shift in the devices' resonance frequency responding to the shift in pressure of the chamber with PDMS membrane. The wider width clearly shows sharper peaks and higher SNR. Under the conditions of this experiment, the large device with original width yields to a pressure responsivity of 857 kHz/mmHg (Fig. 32-a). On the other hand, the large device with the wider width yields to a pressure responsivity of 919 kHz/mmHg (Fig. 32-b).

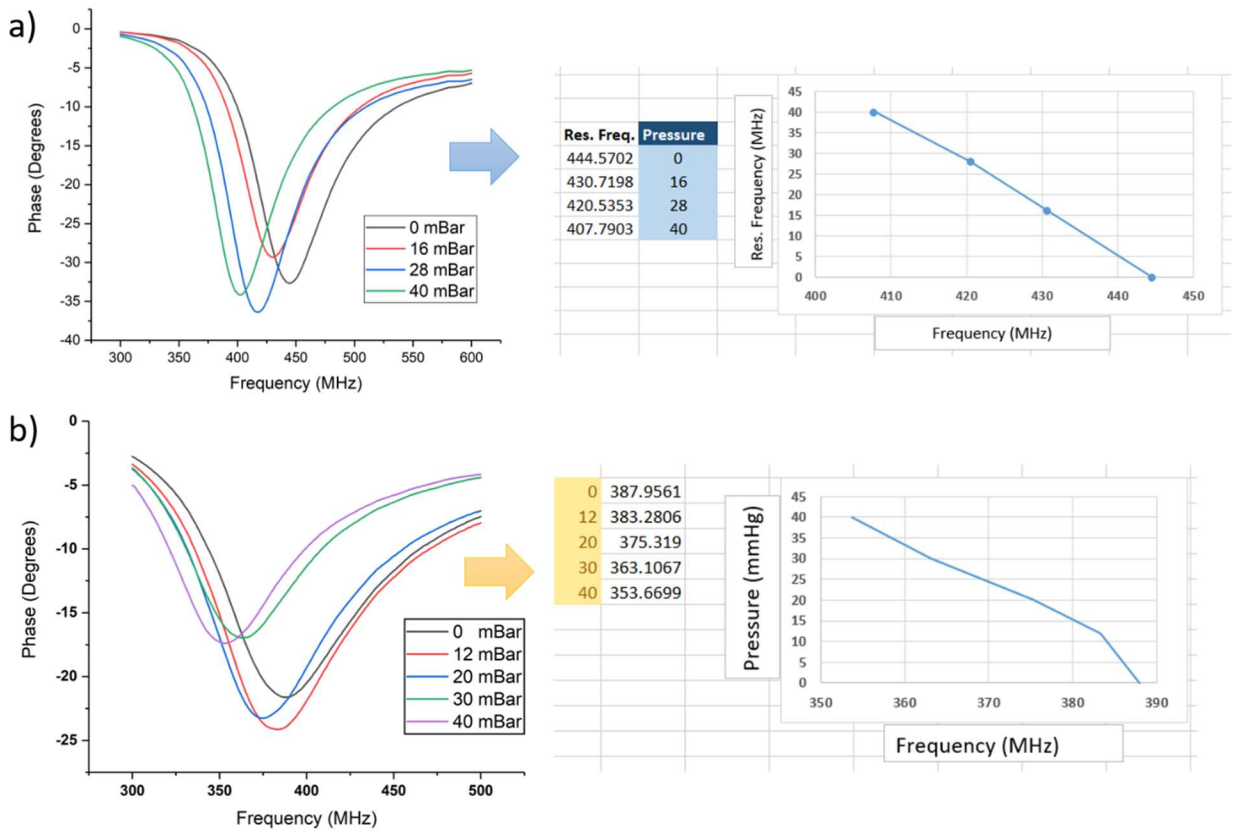

Figure 32. The pressure responsivity of devices inside PDMS membrane. a) The shift in resonance frequency of a large sensor with wider width responding to the change in chamber's pressure. b) The shift in resonance frequency of a large sensor with original width responding to the change in chamber's pressure.

The effect of the planar angle between the reader and sensor coils on the sensing performance was tested under 4 different angles, and the results are shown in Fig. 33-a. The data show that the angular misalignment does not cause any shift in the resonant frequency of the sensor, and the signal is still detectable up to an extreme angle of 60°. Additional testing shows in Fig. 33-b that differences in distance between the reader and sensor coils does not change the frequency of the resonant peak. These results suggest that eye movements would not produce significant errors in pressure reading, but rather a

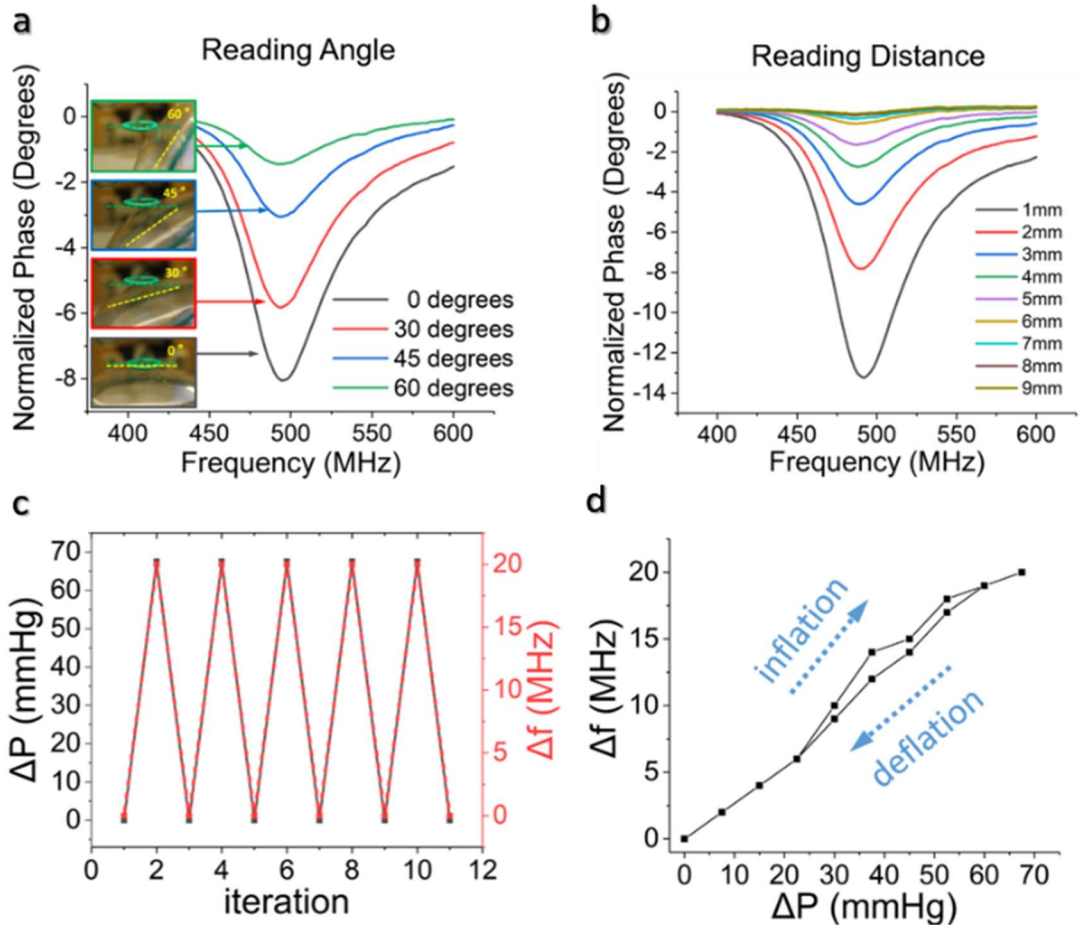

Figure 33. a) Frequency responses of the sensor under different planar angles between the reader and sensor coils. b) Frequency responses of the sensor under different distances between the reader and the sensor coils. c) Repeatability test results of the pressure response in five periods of inflation and deflation. d) Frequency shift in one cycle of inflation and deflation with finer pressure steps uncovering the negligible value of hysteresis.

reduction in the signal strength. The maximal reading distance of the current design is about 9 mm, which can be improved in the future by refining the sensor coil geometries (e.g. number of the loops, diameter, and thickness) and/or increasing power in the reader coil. The reproducibility of the sensor undergoing repeated inflations and deflations was tested under 10 cycles of iteration. Fig. 33-c shows that repeated stretching and relaxation of the sensor loop does not affect the baseline resonant frequency, demonstrating the stability of the sensor. Within one cycle, an overall frequency shift of 20 MHz is detected when ΔP changes from 0 to 68 mmHg. The deflation response exhibits a negligible hysteresis effect as compared to the inflation response, as shown in Fig. 33-d.

We studied the effects of environmental parameters (humidity and temperature) on the sensing performance of the device. The contact lens with the embedded sensor was placed inside a beaker next to a commercially available sensor (Temperature and Humidity

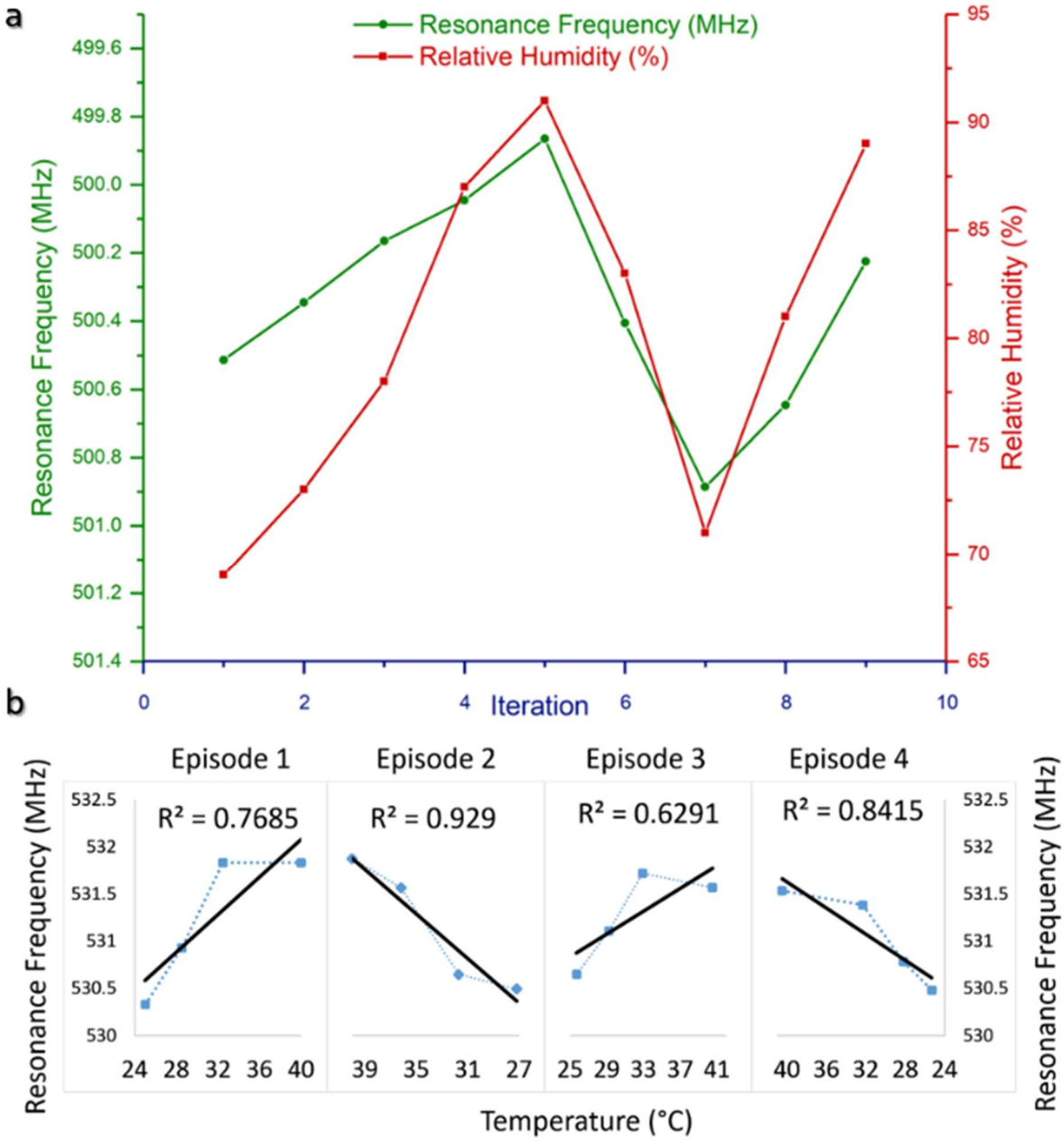

Figure 34. The change in the resonant frequency follows the trend of ARH change- repeated in three episodes. b) The change of the resonant frequency follows the trend of temperature change- repeated in four episodes.

Monitor- TP-50, ThermoPro) and the entire beaker was covered with plastic wrap. Using this apparatus the humidity is adjusted (when the beaker is uncovered) fast enough that the desired dynamic range for humidity is attainable without a significant change in temperature (<2°C). Therefore, we could isolate the effect of change in humidity on the contact lens from the effects of temperature fluctuations. In a separate apparatus, the contact lens with the embedded sensor was placed on top of a hot plate covered with aluminum foil and the temperature varied while being monitored by an infrared thermometer (Infrared Thermometer-IRT0421, Kintrex). In this setup, even though the temperature on the contact lens sensor varied over a high dynamic range, humidity remained essentially unchanged due to the free flow of the surrounding air.

Fig. 34-a depicts the resonant frequencies of the sensor under different ambient relative humidity (ARH) values of 69% to 91%. Within one and a half cycle of the ARH change, it is found that the resonant frequency of the sensor follows the trend of the ARH change. There is a downshift in the resonant frequency with an increase in ARH. This is caused by the swelling of the PDMS contact lens when ARH increases [94], resulting in an expansion of the coil curvature. When ARH reduces to its original value, the PDMS contact lens shrinks and the resonance frequency upshifts. The third half-cycle shows a similar trend. Additional experiments are conducted to analyze the effect of ambient temperature (AT), during which the sensor undergoes repeated heating and cooling and the device frequency response is measured in a temperature range of 25°C to 40°C that encompasses the AT change of the cornea. Fig. 34-b shows the four episodes of measurements that each presents

half a cycle. When the AT increases from 25°C to 40°C, the PDMS contact lens shrinks, and therefore the resonant peak of the sensor upshifts to the higher frequency range. When the AT drops to 25°C, the resonant peak returns to its original frequency with a repeatable profile. These results suggest that the effects of AT and ARH on the sensor performance can be predicted, calibrated, and cancelled by the design of the future, measurement unit with built-in humidity and temperature sensors.

2.4 Discussion

This report presents a wireless, passive, sensor inside a doughnut-shaped contact lens that enables continuous monitoring of the change in the curvature of the cornea induced by IOP variation. This sensor consists of a stretchable coil and a micro-fabricated capacitor that is made of gold and titanium thin films sandwiched between multilayer Parylene C for extra biocompatibility. The sensor is completely encapsulated inside a doughnut-shaped contact lens made of PDMS which is soft, biocompatible, and permeable to moisture and gas. The strain sensor is tested separately in a PDMS membrane, showing a responsivity of 523 kHz of frequency shift per 1% axial strength. In vitro measurements on a canine eye demonstrate a responsivity of 44 kHz shift per 1 mmHg of pressure change. While consistent and measurable, the responsivity of the doughnut-shaped contact lens sensor is less on the canine eye compared with measurements of the device alone. This may be due to the quality of the corneas from the isolated eye, or imperfect conformity, and thus adhesion, of the lens to the test eye. Additional testing demonstrated that differences in

the planar angle between the IOP sensor and external reading coil reduced the signal strength, but not the resonant frequency response of the sensor, thus indicating that eye movement does not produce significant errors. Repeated stretching and relaxation of the sensor ring also does not affect the baseline resonant frequency. Ambient relative humidity and temperature can cause shifts in resonant frequency, but these too track back to baseline when each factor returns to its starting point.

2.5 Conclusion

This part of the thesis reports a wireless, passive, sensor inside a hollow contact lens that enables continuous monitoring of the change in the curvature of the cornea induced by the IOP variation. This sensor consists of a stretchable coil and a micro-fabricated capacitor that are made of gold and titanium thin films sandwiched between multilayer Parylene C for extra biocompatibility. The sensor is completely encapsulated inside a hollow contact lens made of PDMS which is soft, biocompatible, and permeable to moisture and gas.

The strain sensor is separately tested in a PDMS membrane, showing a responsivity of 523 kHz of frequency shift per 1% axial strength. In vitro measurements on a canine eye demonstrate a responsivity of 44 kHz shift per 1 mmHg of pressure change. While consistent and measureable, the responsivity of the hollow contact lens sensor is less on the canine eye compared with measurements of the device alone. This may be due to the

quality of the corneas from the isolated eye, or an imperfect conformity, and thus adhesion, of the lens to the test eye.

Additional testing demonstrated that differences in the planar angle between the IOP sensor and external reading coil reduced the signal strength, but not the resonant frequency response of the sensor, thus indicating that eye movements does not produce significant errors. Repeated stretching and relaxation of the sensor ring also does not affect the baseline resonant frequency. Ambient relative humidity and temperature did cause shifts in resonant frequency, but these too track back to baseline when each factor returned to its starting point.

2.6 Future Directions

While the in vitro studies in this thesis show promising horizon for the efficacy of the CLS with acceptable pressure sensitivity, there are necessary in vivo studies scheduled to be conducted on rabbits as this project continues forward. Those studies require small portable reader device (impedance analyzer) that is being developed by a local company called in2being. The portability of that device allows the laboratory-based behavioral studies of these freely moving rabbits with contact lenses on their eye and the reader coils placed inside a pair of goggles they wear. Those studies are next milestone before the devices are fine-tuned to be tested on human subject, eventually and move forward towards obtaining an FDA approval.

CHAPTER 3

Wireless, Smartphone-Controlled, Battery-Powered, and Head-Mounted Light Delivery System for Optogenetic Stimulation

3.1 Introduction

This chapter reports the design, fabrication and characterization of a head-mounted, flexible, and ultralight optogenetic system that enables wireless delivery of light into the brains of awake and freely behaving animals. The project is focused on miniaturized design, light weight (2.7g), small volume, low cost (< 25 USD) and simple fabrication for research studies on animal brains and learning the effects of optometric stimulation on cellular mechanisms. The chip, the substrate material, the battery, and the micro light emitting diode (μLED) are commercially available. The device implementation consists of one step photolithography, soldering, and packaging along with Arduino programming. In vivo study is carried out where the battery-powered μLED stimulates the visual cortex of a rat with parameters that can be controlled wirelessly via a smart-phone user interface application. The efficacy of optical stimulation is validated using c-Fos as a report of light-evoked neuronal activity.

3.2 Materials and Components

Fig. 35 illustrates the design concept of the presented wireless optical stimulator, which consists of a single μLED for optical stimulation, a programmable Bluetooth interface (Simblee RFD 77101, DigiKey), and a CR1632 coin-cell battery inserted between two pin clips. As the key component in this device, the Simblee RFD77101 module contains two main function blocks: A 32-bit ARM Cortex-M0 processor (with 128KB of Flash and 24KB of RAM - running at 16MHz) for programming and data storage as well as a Bluetooth Smart Radio for wireless communication with a smart-phone user interface. The chip has a compact size of 10×7×2.2 mm^3, suitable for implantation in the brains of small animal subjects, such as rats and mice. The circuit board that carries the chip is made of a copper cladded polyimide thin film with desired mechanical flexibility and biocompatibility. The entire device is completely encapsulated with Parylene-C as biocompatible packaging that insulates the entire system against biodegradation. The device is powered using a CR1632 coin cell battery with 137 mAh capacity, weighing 2.09 grams, capable of driving a μLED continuously several hours. During operation, the battery stays outside and can be easily replaced between trials, while the chip and circuit board can be implanted under the skin, on top of the animal's skull.

Figure 35. The conceptual diagram of the fully implantable system. The phone application helps to select the duty cycle and the frequency of the stimulating signal to the microcontroller (μCon) using Bluetooth technology.

The device has a total weight of 2.7 grams including the battery (2.1g), which is 0.2 grams lower than the one reported in [90]. Our devices is battery powered which enables long range within several meters, however, the device in [90] is wirelessly powered which limits the range to few centimeters. Our system can source maximum output power of 45 mW (3 channels simultaneously: each 15 mW) which is 10 times more than reported in [89].

3.2.1 Fabrication method

Procedures for device fabrication and assembly are illustrated in Fig. 36. For the circuit board, a commercially available, double-sided 9-μm-thick (each side) copper cladded polyimide film is used as the substrate (Step 1). Photoresist is spun on the substrate and patterned using ultraviolet (UV) lithography as a mask for patterning copper (Steps 2 & 3). Unwanted copper is chemically etched to form interconnection wires and pads for chip and μLED assembly (Step 4). The photoresist mask is removed with acetone followed by isopropanol alcohol and deionized (DI) water rinse (Step 5). Commercial surface-mounted blue μLEDs (270μm × 220μm × 50μm, peak wavelength at 460 nm, Cree TR2227TM) are bonded on the corresponding pads by applying low-melting-point (LMP) solder (melting point at ~ 62 °C, 144 ALLOY Field's Metal, Rotometals, Inc.) [95] (Step 6). The adhesion between Polyimide and Parylene was not investigated in this study; however, some methods such as treatment with A-174 followed by annealing can increase the adhesion [96].

After the circuit board is fabricated, the electrical, optical and thermal properties of the assembled LED are tested. Once confirming the functionality of the LED, the Simblee chip is assembled onto the circuit board with silver epoxy. Then the chip connections can be tested using the programmer to verify whether the chip can be successfully powered and recognized by the computer. After that, the pin clips for holding the battery are soldered onto the same circuit board. Finally, the assembled device is coated with 10μm Parylene-C, a polymer with proven biocompatibility (ISO 10993 & USP Class VI), mechanical flexibility (< 200% elongation-to-break), optical transparency (<70% transmittance after 300nm),

chemical inertness, and low permeability (water vapor transmission rate: 0.08 g.mm/m^2. day) [97].

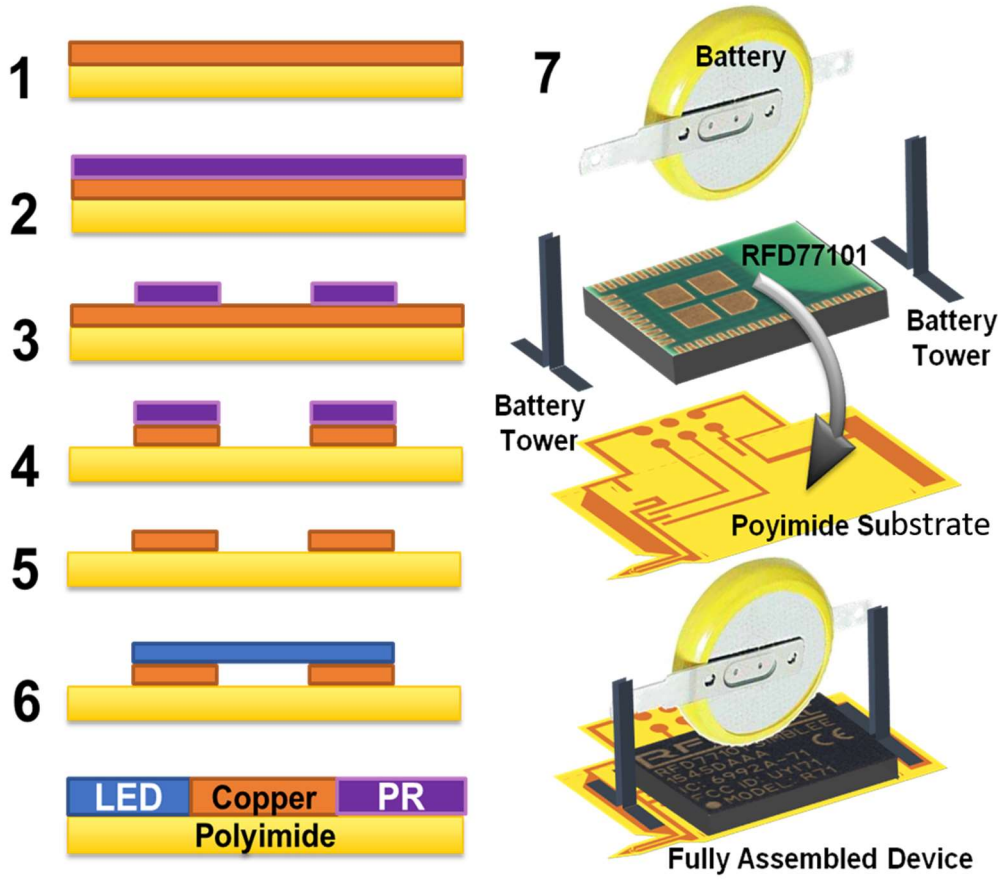

Figure 36. Process flow of the device microfabrication and the assembly.

3.2.2 Programming and smart-phone interface

Pre-programming the assembled Simblee chip is conducted by connecting the programming pads (PD) on the circuit board to a USB shield (1x RFduino) via a 6-pin cable (TC2030-MCP-NL) (Fig. 37) before the encapsulation with Parylene-C. Three pins are used to program the chip which are called RESET, TX and RX and they are for transmitting and receiving the data. The VDD and GND are both driven by the battery and the programming

cable (while being programmed). After being programmed, only the battery powers the system. Overall, 5 pins out of 6 are used from the 6-pin cable. The programming pads on the device are designed on a smallest possible area to reduce the overall footprint. The programming pads can be cut off once the code is uploaded to the chip to further reduce the device size.

Three output pins are used to drive one LED. Each output can drive up to 5 mA electrical current at 2.9 Vp-p. So, three pins are used to be able to drive 9 mA electrical current to one LED. There are 30 I/O ports in Simblee that 27 of them can be used for driving LED channels. It can simultaneously drive up to 3 channels (@5mA max. each).

The Simblee chip uses an Arduino based technology and it can be programmed using Python language. Simblee provides a technology called SimbleeForMobile that allows the user to create and interact with an iOS or Android interface all from Simblee. Using only one app, it enables interaction with any Simblee device, no matter the application. SimbleeForMobile is a header file that is included in the beginning of the code. The main code consists of four viod functions. First, the serial communication is set up along with the process command in a function called *setup*. Then, a function called *loop* awaits for a command directed from the *event* function. Before *event* function there is a function called *ui* which is where the user interface is constructed.

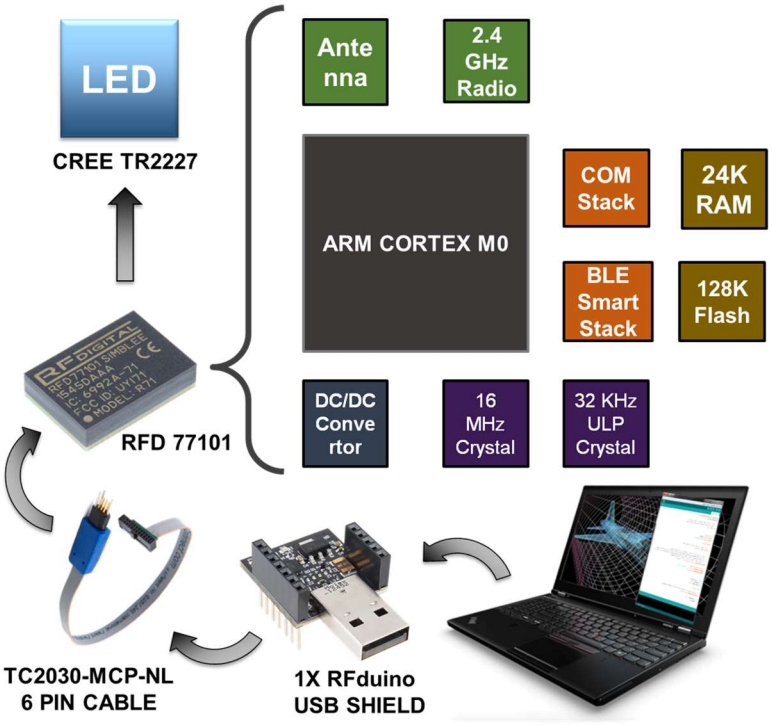

Figure 37. Block Diagram of the Simblee chip along with the process flow of the programming. The Simblee has an ARM Cortex Mo in its heart. 24K RAM and 128K Flash. A 2.4 GHz radio plus an internal antenna. A DC/DC convertor and two crystals. The laptop sends the programming data to the simblee through the 1xRFDuino USB shield and the 6-PIN cable. The Simblee chip drives current for the µLED.

Lastly, the *event* function reads and runs the requested stimulation parameter. Certain parameters such as duty cycle, frequency and the intensity (light intensity is not controlled in the current design – but it is available in the next design) of µLED light are controlled in this function and executed in *loop* function Refer to the Simblee guide-book [98] for more information about programming.

3.2.3 In vivo experiment

Acute *in vivo* experiment is conducted on one adult Sprague Dawley rat (female, 300-350 g) to verify the surgical and functional applicability of the prototype wireless opto-electro

neural interface system. The animal protocols used in this study are approved by the Institutional Animal Care and Use Committee (IACUC) at Michigan State University. Prior to device implantation, the rat receives virus injection (AAV-hSyn-hChR2 (H134R)-mCherry; 10^{12}~10^{13} genome/ml; UNC Vector Core) in the primary visual cortex (V1) to express neurons with light-sensitive channelrhodopsin-2 (ChR2). For virus injection, the subject is isoflurane-anesthetized and placed on a stereotaxic apparatus.

Using sterile surgical procedures, a 3~4 cm incision is made in the skin overlying the skull and a small region of bone is removed to expose V1. Using a Hamilton syringe, the AAV virus is injected in both left and right V1 cortices, with 3 equidistant locations on each V1 and 1.0 µL per side. The cortex is covered with Gelfoam and the skin overlying the skull is sutured closed. Two weeks post-injection, the transfected rat is re-anesthetized and the stereotaxic surgery is performed for device evaluation. The µLED is surgically implanted on the right V1 and the µLED cable is firmly attached onto the skull using dental cement that prevents device movement during optical stimulation. The left V1 of the same animal is used as a control for comparison. Then the skin is sutured closed, leaving the circuit board and battery outside of the brain.

During the experiment, the right V1 is optically stimulated with continuous light pulses of 1 Hz frequency and 5% duty cycle for 45 minutes. The µLED is driven by 2.9 Vp-p (9 mA) that is the maximal voltage/current output supplied by the Simblee in the current design.

Table 3. Device dimensions of the two versions.

	Max. Depth at µCon	Length tower-to-tower	Width without PD area	Tower Height	Probe Length	Weight without Battery
β	2.35 mm	25 mm	10 mm	14 mm	6.2 mm	0.83 g
α	2.35 mm	15 mm	8.1 mm	8.8 mm	2.4 mm	0.62 g

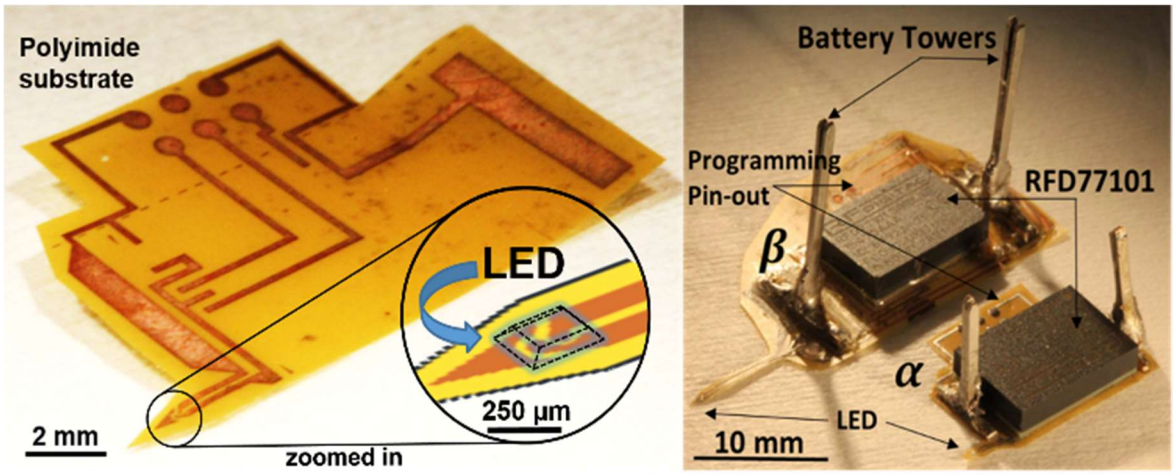

Figure 38. The flexible substrate for the implantable light delivery system. Right) Two versions of the complete device: Beta is the first design which is head-mounted, tested, and reported here. Alpha is the smaller design which is fully implantable.

After stimulating the right V1 lobe and leaving left V1 lobe unstimulated as negative control, the rat is given a 75 min survival period, prior to perfusing with chilled saline and 4% paraformaldehyde and post-fixing brain tissues overnight at 4°C in the same solution. Tissue sections with a thickness of 50 µm are cut in chilled 0.1 M phosphate buffer and stored in 24 well tissue culture dishes for post immunohistology chemical processing. After that, the processed sections are mounted on microscope glass slides and covered by coverslips with an anti-fade solution for c-Fos expression imaging under a fluorescent microscope with 10x and 20x magnifications.

3.3 Results

Fig. 38 (Left) shows a fabricated flexible circuit board and the assembled devices. There are two designs of the device with minor differences in the size and routing of the substrate (Fig. 38-Right). Having a feedback from the animal's head dimensions, a second version is designed with smaller dimensions and the same components (Fig. 38- Right). The dimensions of both versions are shown in Table 3. The Parylene coating adds a 10 micrometer thickness on devices.

The temperature profile of the μLED is characterized using FLIR infra-red camera. Fig. 39 shows the rise in temperature near the μLED measured in air (which is a worse scenario than saline or animal tissue), under different current inputs. The temperature has a sudden rise in the first 10 secs immediately after the μLED is turned on, and then stabilizes with an overall fluctuation of less than 1 °C. At the low current of 4mA, the temperature rise is within a recommended safety limit of 2 °C that will not harm the nerve cells in the brain [99]. Fig. 40-A shows the I-V characteristics of the μLED. Fig. 40-B shows the light intensity measured with various electrical currents showing that 3 mA gives enough light intensities above the threshold for ChR2 activation (~1mW/mm^2) [100]. Particularly, the parameters used in the animal study are 1 Hz, 5% duty cycle, 9 mA, and 2.9 Vp-p.

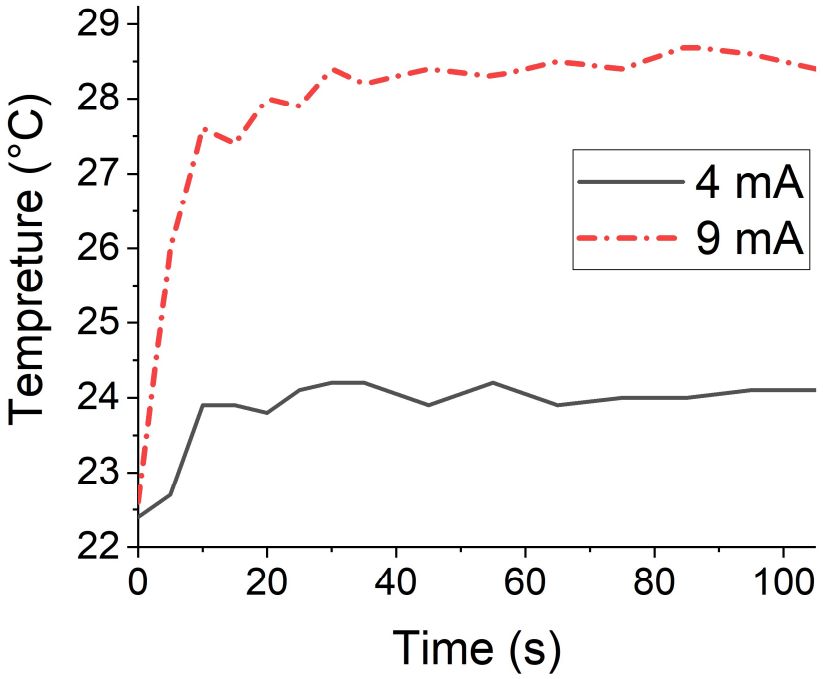

Fig. 39. Temperature versus time, measured in the vicinity of the micro μLED after it is electrically driven by two different currents (4mA and 9mA, DC current).

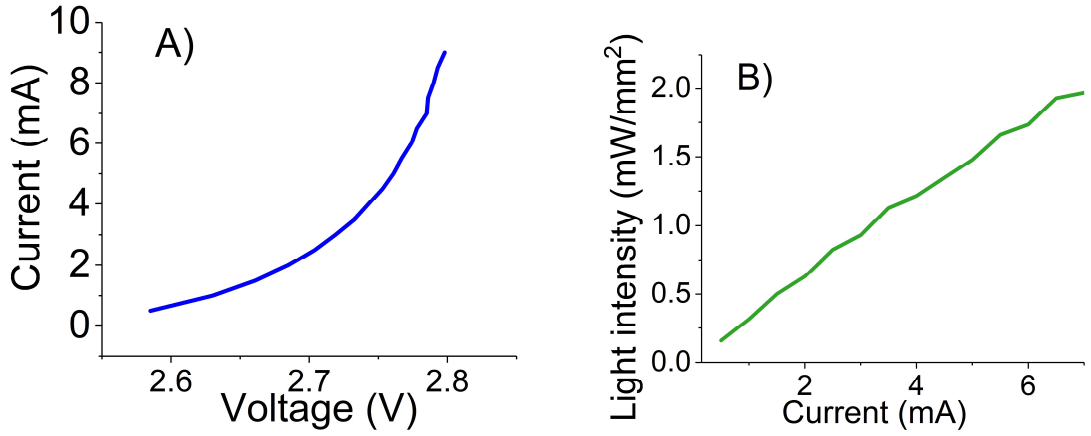

Fig. 40. A) I-V characteristics of the μLED measured using a series resistor with the μLED. B) Light intensity versus current.

Fig. 41 (a) shows the placement of the larger device on the rat's head. Fig. 41 (b)-(e) show the c-Fos results, where the green fluorescence indicates cells expressing the c-Fos reporter. There is a significant up-regulation of the c-Fos expression in the stimulated V1 lobe (Fig. 41-c&e), demonstrating that the optical stimulation resulted in an increase in neuronal activity. In contrast, the control section (the left V1) in Fig. 41 (b) and 39 (d) showed only a mild increase in the c-Fos immunostaining of soma bodies. This increase in the c-Fos expression of the control is partially attributed to the mechanical compression of the soft cortical tissue when opening the craniotomy window and also the fact that this is the visual system and there probably was natural visual input from the eyes, as well.

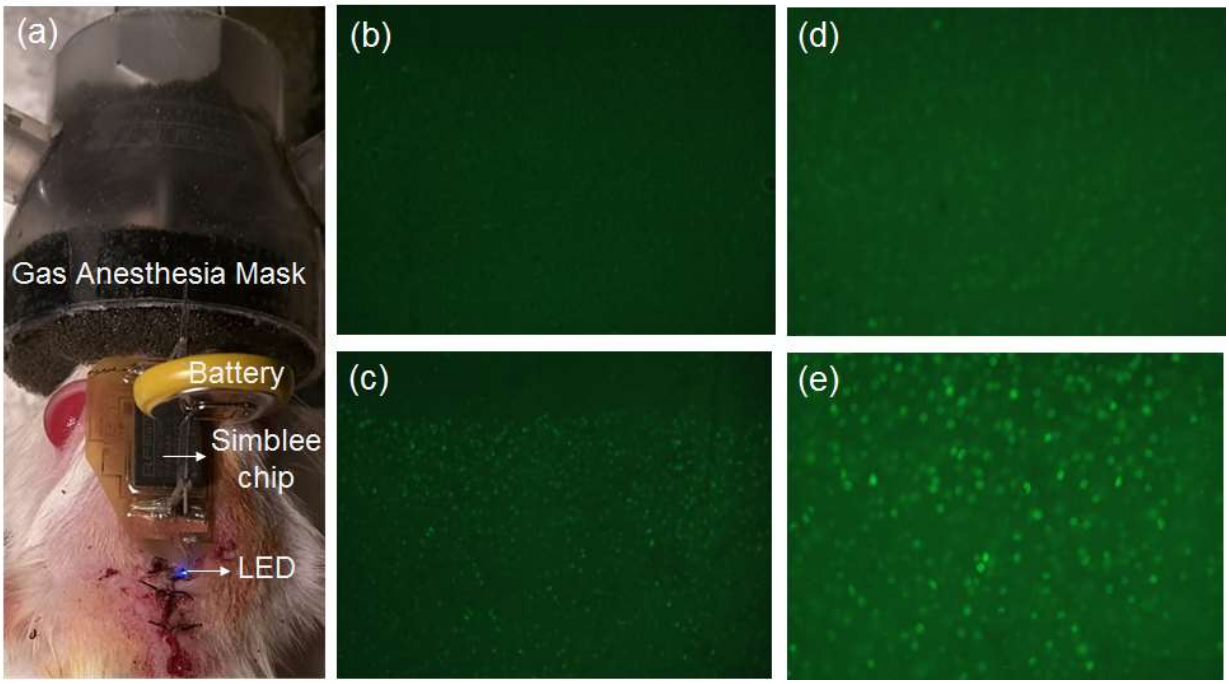

Fig. 41. Optical stimulation setup and results from c-Fos section. a) Testing stimulation on a Sprague Dawley rat anesthetized by gas mask, b) 10x – c-Fos - unstimulated, c) 10x – c-Fos - stimulated, d) 20x – c-Fos - unstimulated, e) 20x – c-Fos – stimulated.

3.4 Conclusion

We present the design, fabrication and characterization of head-mounted, flexible, and ultralight optical delivery system that enables wireless delivery of light into the brains of awake and freely behaving small animals. The entire fabrication can be completed in one day using affordable, off-the-shelf and commercially-available components and the device can be used permanently with interchangeable coin-cell batteries. Since the Simblee phone application is able to control multiple chips at the same time, using our system, optogenetic experiments can be performed on multiple animals at the same time.

Each system is potentially able to source up to 27 channels (3 channels, simultaneously). Therefore, 27 LEDs can be implanted using one system and they can all interchangeably stimulate the neurons in the animal's brain with 3 LEDs at the same time. The chip is also able to record temperature using one of its analog inputs. This can be used to monitor the temperature near the stimulation area and shown on the smartphone application for extra control if desired. Following this work, we are going to implant the system into the head of a living Sprague Dawley rat and at the same time record the corresponding stimulated neural activity.

3.5 Future Directions

The chip used in this project (Simblee RFD 77101) is now discontinued and not available for further iteration of device assembly and tests. Therefore, another micro BLE chip is identified called BMD-350 that uses ARM architecture (nrf52832). This BLE chip has been under studies as the continuation of this project and it's been successfully programmed on a development board called BMD-300 EVAL. We have successfully customized the program in NRF studio and adjusted a PWM code to our needs as described earlier. Those PWM signals are tested to work properly on an LED that was connected to the evaluation board. It is also tested to work nicely using an Android application to control the PWM parameters wirelessly through the app connected to the chip using Bluetooth. All that is left before the next step is to program an external BMD350 chip through the J-Link that is wired off the evaluation board as the main programmer. Once that external chip is fully programmed and soldered on the flexible polyimide substrate it will be ready to be implanted on the brain of the mice while being controlled by the Android application. The battery is also envisioned to be carried in a small backpack on the back of the rat while it is wired under the ski towards the device that is also fully and surgically hidden under the skin on top of the brain of rat.

CHAPTER 4

Hybrid Chemomechanical Promotion of PEDOT Adhesion on Microelectrode Arrays for Chronic Neural Stimulation

4.1 Introduction

Advances in neural prosthetic technologies demand ever increasing novelty in material composition to enhance the mechanical and electrochemical properties of the existing microelectrode arrays. The standard approach for increasing the density of electrodes is decreasing the size of individual electrode sites so that more can be placed on a given size of epicortical or penetrating electrode arrays. The challenge in doing so is enhancing the electrical charge storage capacity (CSC) of ultra-small electrode sites (<50μm). The key approach is enhancing CSC using inorganic coating technologies. Even though there are multiple approaches to enhance CSC of the existing inorganic coating technologies [101-104], conductive polymers promise significantly better cellular agreement [105-107] while they maintain superior CSC, high flexibility, and lasting biocompatibility [108]. Among them, Poly3,4-ethylenedioxythiophene (PEDOT) stands out as the most established and investigated in literature to date. PEDOT's physical advantage over solid state materials is allowing the transportation of ionic charge across its entire bulk as well as transporting electrons in an ohmic fashion. This inherent advantage proudly presents itself in form of increased charge storage capacity, larger interfacial capacitance, and lower electrical resistance. PEDOT's typical injectable charge into the surrounding tissue can be maximized to more than 15 mC/cm2 [109] that is 100x better than platinum [110] and 15x better than iridium oxide [111] and titanium nitride [112].

Another advantage of PEDOT in neural interface coating is its customizability while accepting various electrical dopants or immunosuppressant drugs during its electrodeposition [113]. N. Kim et al. [114] showcase this advantage by studying and comparing more than ten secondary dopant molecules such as polystyrene sulfonate (PSS), Perchlorate (CLO_4), and hexafluorophosphate (PF6) integrated into PEDOT as counter ions under a diverse range of chemical reactions. While each of these molecules and reactions solve different problems and offer unique capabilities for diverse applications, in this work, tetrafluorborate (BF_4) is incorporated as the secondary dopant material while electropolymerizing PEDOT. As reported by Bodart et al. [115] PEDOT:BF_4 is durable and offers favorable electrical properties. Though, long-term and in-depth biocompatibility of PEDOT with any of these variations remain unknown. One of the main obstacles in adopting PEDOT for chronic neural stimulation is its instability and poor adhesion to inorganic electrodes surfaces. Even though some researchers have reported electrochemical attempts [116-117] to solve this problem and some others suggest reducing thin film shear stress [100], the extension of long-term durability of these delicate thin films remains a challenge. Diazonium salt has been shown capable [119] in establishing decently strong covalent bonds between the PEDOT thin films and their underlying metallic base material. In fact, this technique was initially tested using scotch tape and it was observed that it was impossible to remove the PEDOT coatings on platinum whereas without diazonium salt, PEDOT thin films were easily peeled-off from Pt sites.

4.2 Materials and Methods

Electrode arrays were designed, manufactured and provided by SSMP. The versions that were used in this work are epiretinal and epi-cortical electrode arrays comprising 60 channels circular/planar sites with diameters of either 100μm or 200μm, respectively. They are both fabricated using single-layer sputtered platinum insulated by spin-coated polyimide that are shaped by standard photolithography using photoresist and ultra-violet light. Also, patented by SSMP the platinum electrode sites are coated with typically 8 μm of platinum grey that enhances the microporosity, effective surface area and charge storage capacity above the minimum stimulation thresholds that evoke phosphenes and cause visual percepts. The specific settings for electroplating platinum grey coating is intellectual property of SSMP and are not publicly available.

Electrografting diazonium salt on electrode surfaces was carried out based on a recipe originally reported by D. Chhin *et al.* [108]. Tetrafluoroboric acid, (4-thien-2-yl) aniline, diethyl ether, sodium nitrite, and lithium perchlorate were purchased from Milipore Sigma. Tetrafluoroboric acid 50% (124 μL, 1 mmol) was mixed with (4-thien-2-yl) aniline (175 mg, 1 mmol) with dropwise addition of acetonitrile until dissolution. The mix was then cooled to –10◦C by placing the beaker inside a mixture of deionized ice-water and acetone. An aqueous solution of saturated sodium nitrite (69 mg, 1 mmol) was then added dropwise to the (4-thien2-yl) aniline solution. The resulting suspension was filtered using semi-permeable paper filter and was rinsed with diethyl ether. Eventually, the cyclic

voltammetry was performed on microelectrodes that were placed inside a solution of 5 mM (4-thien-2-yl) diazonium salt dissolved in 100 mM $LiClO_4$ and acetonitrile for 15 consecutive cycles sweeping from –0.5 V to 0.5 V at a step size of 0.1 V/s.

Electropolymerization of PEDOT was performed based on a previously published recipe by C. Bodart *et al.* [115]. Acetonitrile (ACN), polycarbonate (PC) (anhydrous, 99.7%), 3,4-Ethylenedioxythiophene (C_6H_6OS, 97%) and tetraethylammonium tetrafluoroborate ($TEABF_4$, 99%) were purchased from Millipore Sigma. All chemicals were used as received. Electropolymerization was carried out galvanostatically in a 150mL of PC containing 426 mg EDOT monomer (20mM) and 3907 mg $TEABF_4$ (120 mM). Prior to electropolymerization, all solutions were stirred and degassed for 20 minutes using nitrogen and a nitrogen blanket was maintained during the electropolymerization, to limit the oxygen concentration in the solution and prevent unwanted oxidations. Electroplating was carried out in a three-electrode fashion using a Solartron Analytical 1287A potentiostat and galvanostat equipped with a 1252A Frequency Response Analyser. Silver/silver chloride (Ag/AgCl) was used as the reference electrode, a platinum wire as the counter electrode and the platinum and platinum grey electrodes were connected as the working electrodes. The working electrodes were cleaned inside 20% diluted sulphuric acid under cyclic voltammetry, rinsed in deionized water. After electrodeposition, the electrodes were rinsed with deionized water, dried in air, and stored in ambient conditions.

The platinum electrodes with and without platinum grey were tested for long term endurance under continuous round-the-clock electrical stimulation using charge-balanced, current-regulated, symmetric, biphasic pulse pairs at 120Hz and a peak value of 105□A. The long-term stability tests were carried out initially at 37°C in real time for 36 days and then 12.5 days at 67°C plus another 11 days at 87°C for accelerated tests. According to the Arrhenius Equation increasing the solution's temperature by each 10°C accelerates the material aging by a power of two. That means the electrode materials at 67°C age 8x faster than when tested inside the solution at 37°C. Same goes for 87°C at which the electrodes age 32x faster than being at 37°C. After the down conversions, an equivalent total test duration of 88 days for Pt electrodes and 452 days for Pt-Grey electrodes were obtained at 37°C.

4.3 Results

First, a polymer-platinum microelectrode array was selected (Fig. 42- d) and the platinum electrode sites (Fig. 42- e) were coated by PEDOT:BF_4 with/without diazonium salt. Next, a similar microelectrode array (Fig. 42-a) was picked and the Pt/Pt-Grey electrode sites (Fig. 42-f) were coated by PEDOT:BF_4 with/without diazonium salt. A side-view three-dimensional schematic diagram of the proposed hybrid composition is illustrated in Fig. 42-a, which allows the remarkable mechanical integration of PEDOT coating into a maze that is created by the microporous geometry of platinum grey. Fig. 42-b shows the comparable case where PEDOT is directly deposited on bare Pt electrode sites.

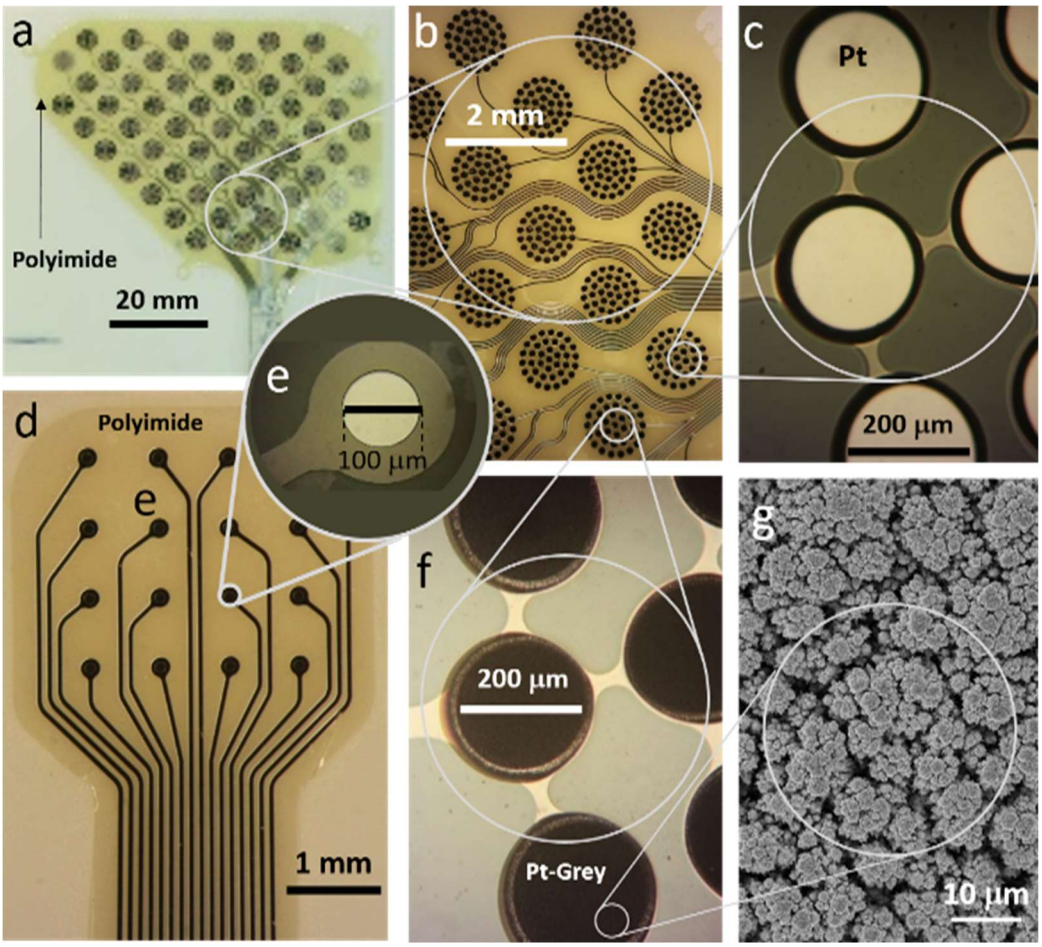

Figure 42. The epiretinal and epicortical electrode arrays used in the first and second experiments, a) The electrode array with 60 channels wired out for external connection. The array is sitting on a ceramic carrier for bench-top handling. b) A closer-view of the same array under optical microscopy. Each cluster consists of 37 sites that are shorted all-together making up for one channel. c) A closer view of the same array showing the circular platinum sites that are shorted together. d) The top-view of the 16-electrode array originally used in The Argus I Device with closer view of one of its electrode sites with bare platinum at a diameter of 100µm. e) A closer view of one of the sites showing the Pt electrode at a diameter of 100 µm. f) A closer view of the same array showing the circular sites that are shorted together but coated with Pt-Grey. g) Top view scanning electron microscopic (SEM) image of platinum grey coating.

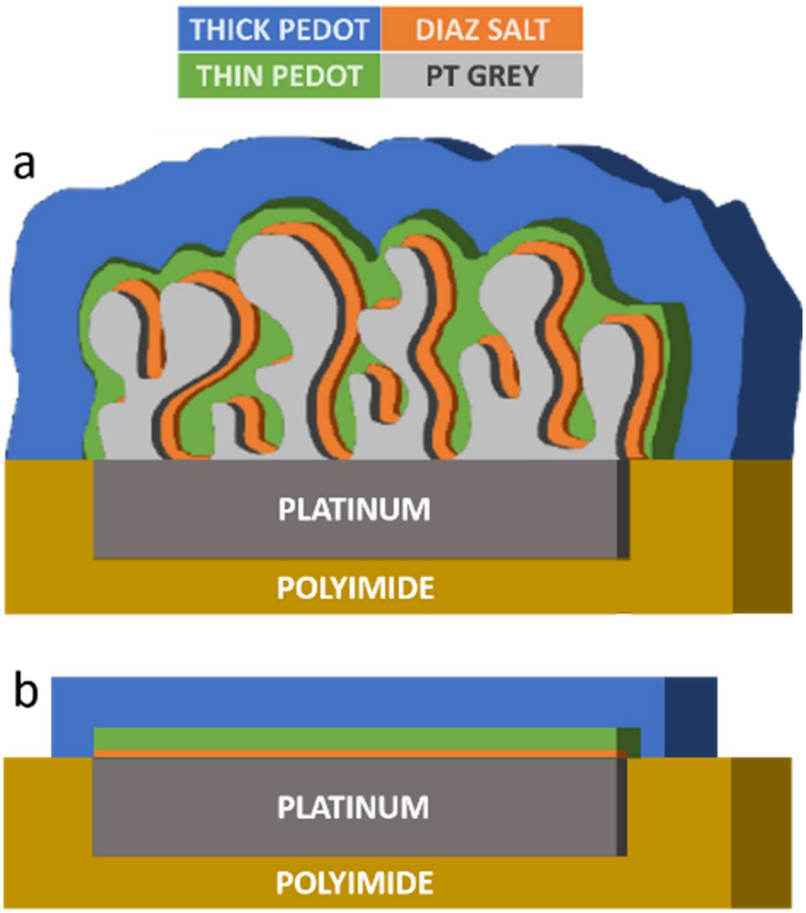

Figure 43. Schematic diagram illustrating the order of thick/thin PEDOT & diazonium salt on a) Pt-Grey coated on platinum, b) Blank platinum electrode sites insulated by polyimide.

We galvanostatically electroplated PEDOT on blank platinum electrodes (d=100um) using different electrochemical currents to identify the optimum current density that creates smooth, thin and uniform PEDOT films. As shown in Table 4 increasing thicknesses of PEDOT are produced by increasing the applied DC current from 37.5nA to 62.5nA and 87.5nA for 2 minutes each. The values in Table 4 are averaged results from 4 electrode sites that were plated simultaneously in parallel.

As shown in Table 4, while the improvement in the interfacial electrical resistance remains similar in all three cases, the electrical capacitance, is enhanced by seven times as the PEDOT thickens by three times. A diameter of 100μm for a circular/planar electrode site and the electrical current of 37.5nA yield optimum quality and correspond to a current density of 0.48 (mA/cm2) which was also employed in the next set of electroplating experiment.

Table 4. Averaged electroplating results from 4 electrode sites in parallel for each case. The images on the first two columns are representative of each group. Varying electroplating current densities result in various thicknesses for PEDOT films on platinum electrode sites. The diameter of the electrode sites in this particular experiment are 100 μm.

Top-View (Initial)	Top-View (+PEDOT)	Applied Charge (μC)	PEDOT Thickness (μm)	ΔR (%) @1kHz	ΔC (%) @1kHz
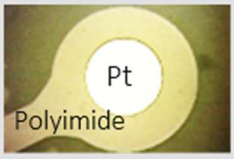		4.5	0.52	-84	+18,600
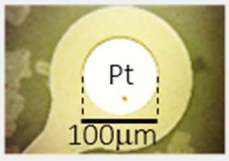		7.5	0.99	-93	+66,800
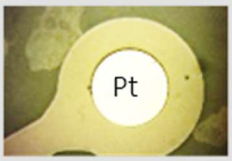		10.5	1.37	-95	+130,800

The cyclic voltammetry (CV) results for the platinum electrode sites before and after PEDOT coatings are illustrated in Fig. 44 at three different electrical currents with similar electroplating time durations. The absolute area of the bottom half of the hysteresis loop in each case represents the amount of charge being stored inside the entire interfacial

coating and transferred to its surrounding solution during each phase. Next, platinum-grey electrode sites were electrografted by diazonium salt electrochemically and then electroplating various thicknesses of PEDOT was conducted on top.

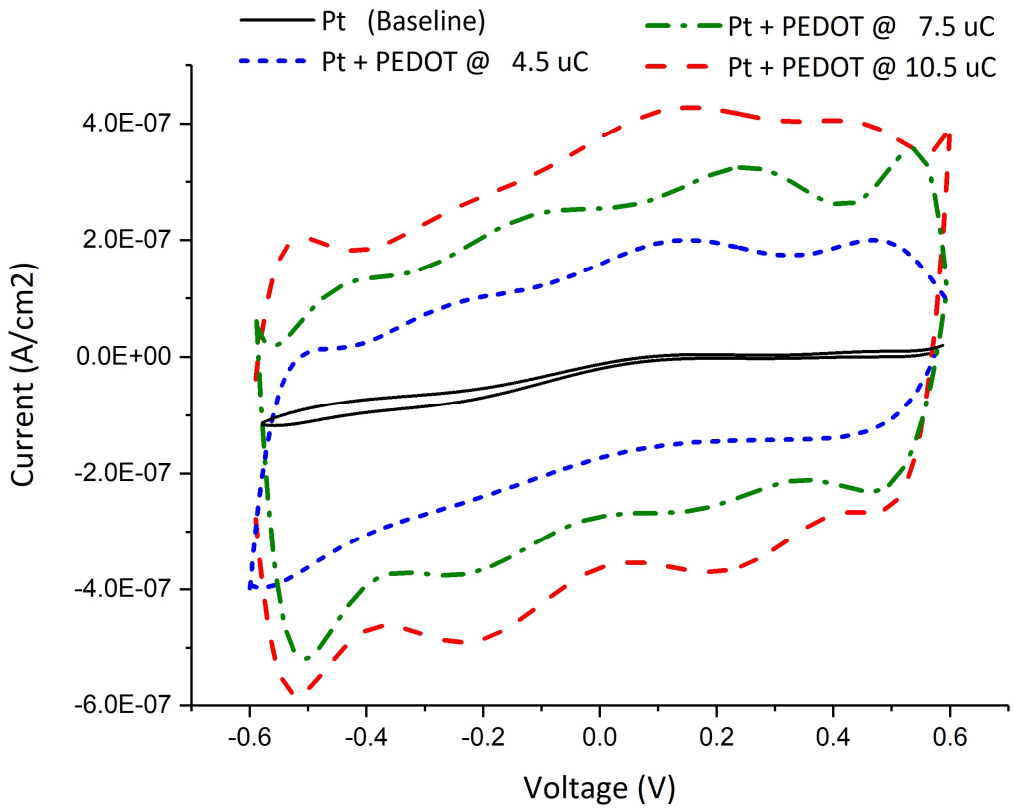

Figure 44. Averaged CV response of the platinum electrode sites before and after electroplating PEDOT thin films at 4.5µC, 7.5µC, and 10.5µC.

Table 5 shows the electrode sites with diameters of 200µm with/without platinum grey coating before/after coating PEDOT atop. From the first experiment the electrical current density of 0.48 (mA/cm2) was found optimum. In the second experiment (Table 5) the electrical current is kept constant at the optimum current density (0.48 mA/cm2) which yields to 150nA for the diameters of 200µm for time durations of 120s, 140s, and 240s, accounting for 18µC, 21µC, and 36µC, respectively.

Table 5. Close view of the platinum electrode sites of the electrode arrays belonging to The Orion Cortical Prosthesis System made by SSMP and used in this work. The first two show PEDOT on Pt electrode sites and the third row show PEDOT on Pt-Grey.

Top-View (Initial)	Top-View (+PEDOT)	Applied Charge (µC)	PEDOT Thickness (µm)	ΔR (%) @1kHz	ΔC (%) @1kHz
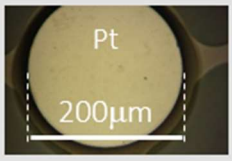		18	0.33	-10	+5,100
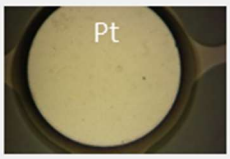		36	0.88	-9	+12,900
		36	0.01	-0.1	+210

Fig. 45 depicts the CV results for the second experiment and compares the effects of coating PEDOT:BF_4 on bare platinum versus platinum-grey. This comparison is carried out from the lens of the CV response at the electrode/electrolyte interface inside 10mM PBS. PEDOT alone on platinum improves the CSC (Fig. 45-blue) more than the amount platinum-grey offers stand-alone (Fig 44-green). Comparing the initial results, it was observed how PEDOT-on-Pt surpasses Pt-Grey-on-Pt by 2.2 times in decreasing the interfacial electrical resistance and 3.7 times in increasing the interfacial electrical capacitance. This finding was key to the motivation behind this study which is to outperform the current Pt-Grey technology developed by SSMP. Eventually, it was demonstrated how the addition of PEDOT on Pt-Grey exceeds the two separate coatings offering maximized enhancement in desirable electrical properties while it presents magnificent bond between the two. The

results in Fig. 45 show that nearly 1μm of PEDOT on platinum benefits the electrochemical performance much better than 8 micrometer of platinum grey does stand-alone. Though, PEDOT films thicker than 1μm do not proportionally increase the positive electrical impacts and indeed the benefits saturate at about 2μm. A few more experiments showed that the PEDOT coatings thicker than 2μm often suffer from mechanical instability and inconsistent quality.

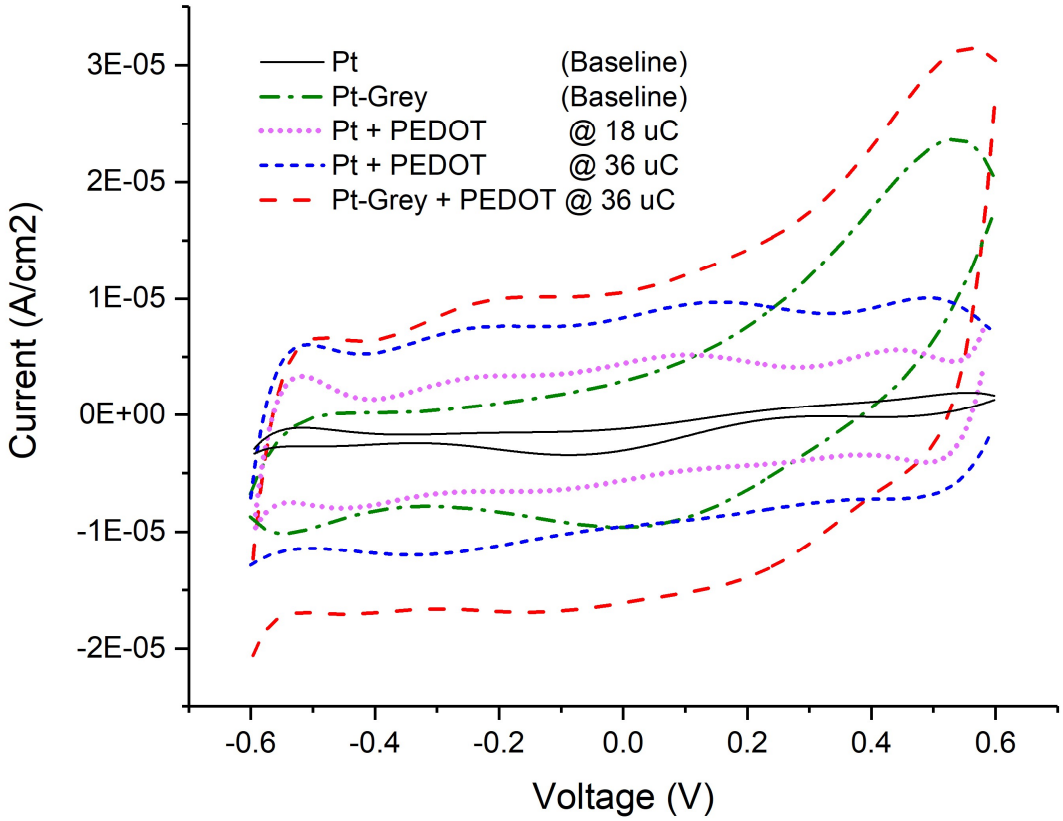

Figure 45. Averaged CV response of the platinum electrode sites with/without platinum-grey before/after electroplating PEDOT thin films at 18uC and 36μC.

Fig. 46 shows the in vitro long-term stability test-setup including the heating and electrical stimulation equipment. The results of that experiment are presented in Fig. 47. In all the cases, the impedance values are averaged from four similar electrodes (with diameters of

200□m) and yet separately electroplated and stimulated in PBS. In all the panels day-1 represents the blank electrodes while day-2 represents the electrodes after they are electroplated with their coatings. The rest of the time the electrodes remain the same in terms of material configuration. The results show that PEDOT coating on Pt electrodes decreases the initial resistive impedance by 3x and increases capacitance by more than 23x. Degradation in performance was observed starting from day 32 (Fig. 47-a&b). The Pt-Grey electrodes were also tested for long periods of time but much longer than Pt electrodes. That's because they are more robust and were tested until degradation was observed. As shown in Fig. 48-a, the presence of PEDOT decreases the electrical resistance by nearly 10% and diazonium salt helps that even further as expected. For nearly 100 days the enhancements remain put and intact until they start showing compromise in their electrical performance. However they remain improved and functional for more than 450 days comparing with no coating (blank Pt-Grey). Fig. 48-b shows the similar favorable impact of PEDOT and diazonium salt on Pt-Grey electrodes in terms of capacitive impedance. Again, after day-2 (applying the coatings) the impressive increase in capacitive impedance is observed for up to 3x with a robust endurance for up to 100 days before the degradation in the capacitive enhancement is observed. Though, the coatings still show some enhancement (10% resistive and 2x capacitive) even after 450 days.

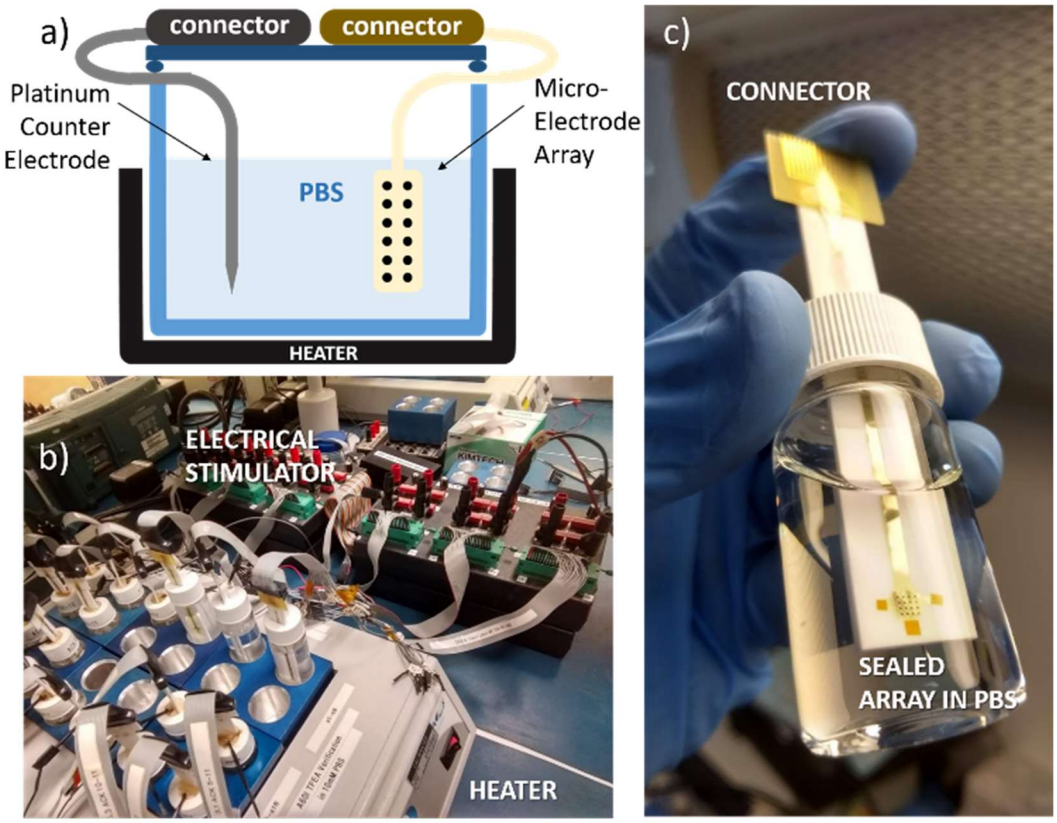

Figure 46. Long term *in vitro* stability test setup for the platinum electrode arrays, a) The schematic diagram shows the main components of the endurance test setup, b) The heating and stimulation units that provide electrical current and heat to the samples inside their PBS tubes while they are probed by oscilloscope for monitoring their biphasic waveforms, c) Close view of one of the samples inside their tube filled with 10mM PBS and sealed with silicone and wired out for connection.

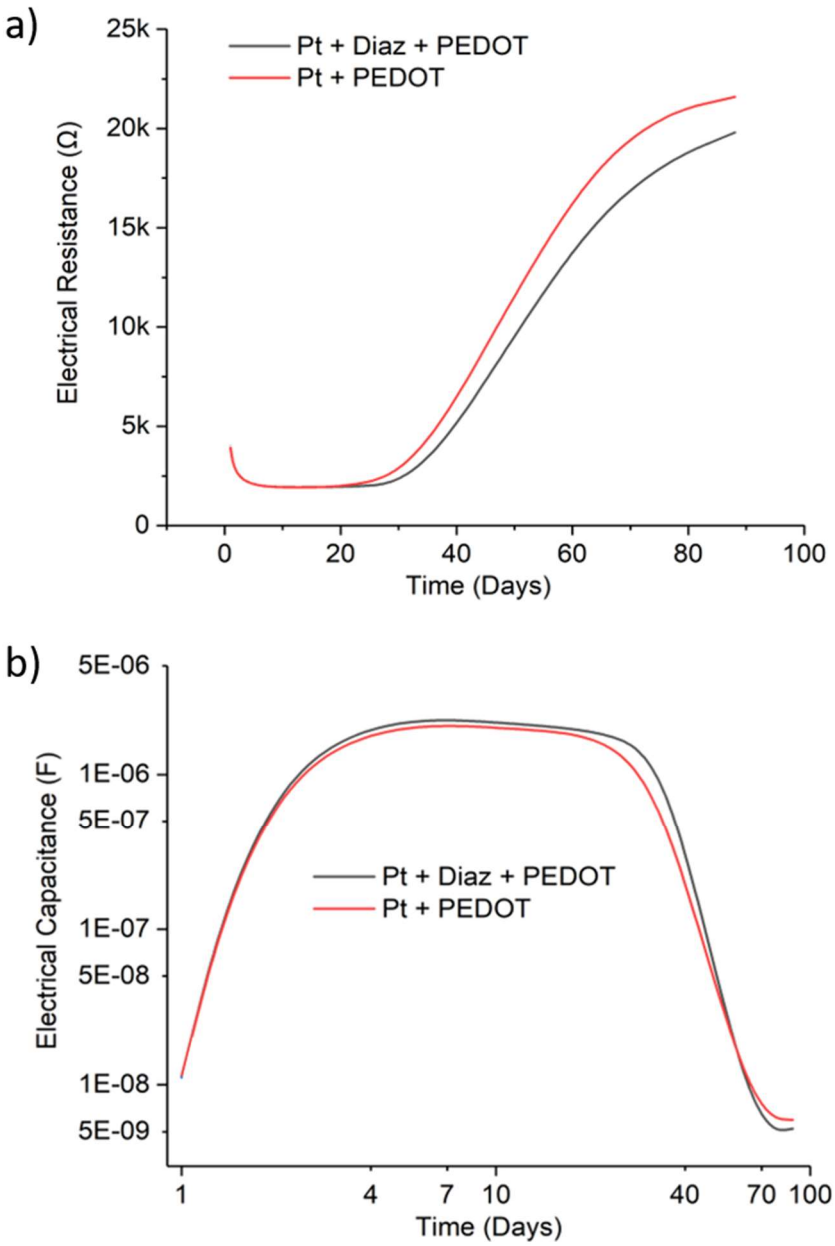

Figure 47. Long term *in vitro* stability test results for the platinum electrode arrays at 37°C. a) 88 days of continuous electrical stimulation on Pt electrodes with PEDOT with/without diazonium salt and its effect on electrical resistance profile over this period b) 88 days of continuous electrical stimulation on Pt electrodes with PEDOT with/without diazonium salt and its effect on electrical capacitance over this period.

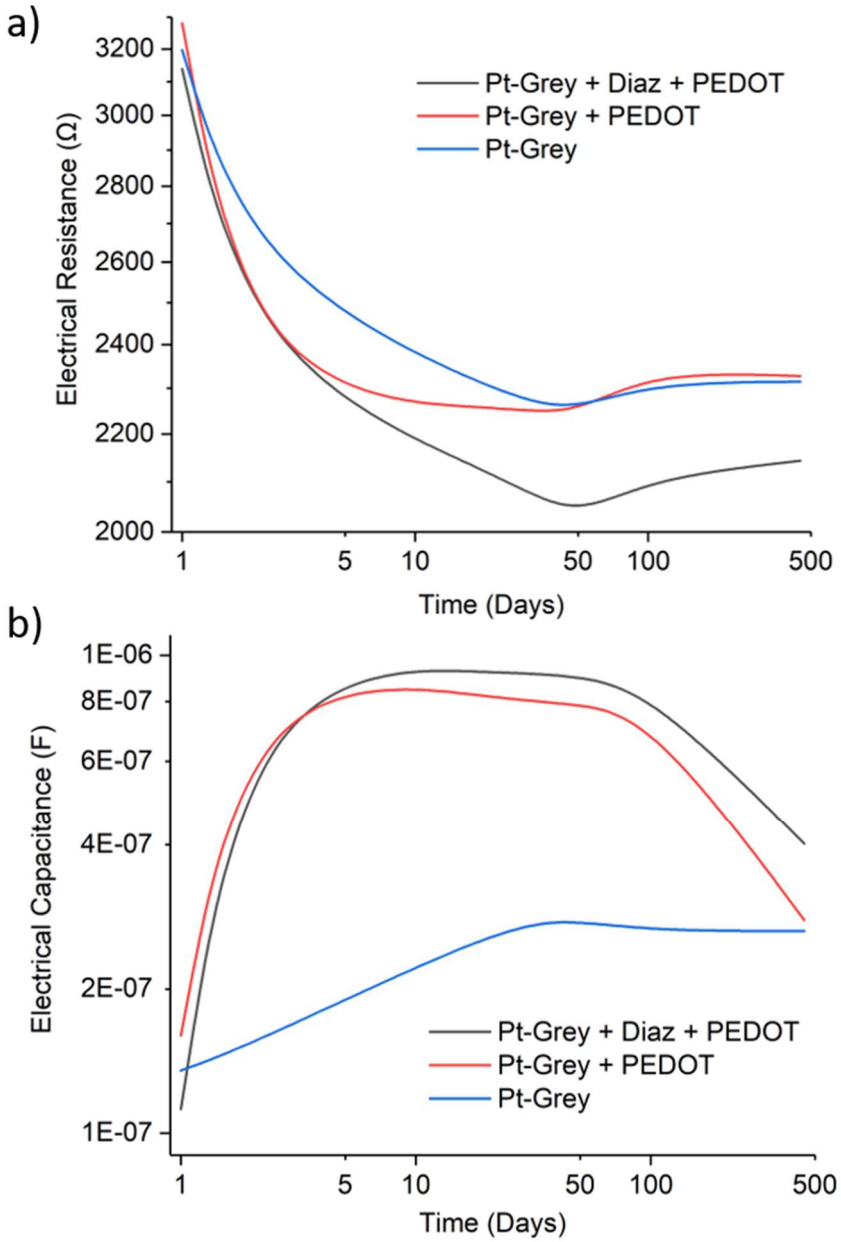

Figure 48. Long term *in vitro* stability test results for the platinum-grey electrode arrays at 37°C. a) 452 days of continuous electrical stimulation on Pt-Grey electrodes with/without PEDOT or diazonium salt and its effect on electrical resistance over this period. b) 452 days of continuous electrical stimulation on Pt-Grey electrodes with/without PEDOT or diazonium salt and its effect on electrical capacitance over this period.

4.4 Discussion

Electrode arrays were designed, manufactured and provided by SSMP. They are flexible and long-lasting electrodes that have been used in Argus II retinal implant and implanted in the eyes of hundreds of human subjects for more than a decade and evoking action potential producing significant visual percepts. [116]. With small variations in geometry, they have also been used for The Orion Cortical Prosthesis implanted in the brains of six human patients delivering bionic vision directly to the visual cortex [121]. This study was designed to enhance the electrical properties of SSMP's existing interfacing electrodes.

As expected, electroplating PEDOT:BF_4 on platinum impressively enhances the electrical characteristics of the electrode sites decreasing the interfacial electrical resistance across and increase the electrical capacitance formed at the electrode/electrolyte interface. The endurance of platinum grey is much more satisfactory, especially at higher thicknesses which cannot be surpassed by current state of the art conductive polymers. Therefore, PEDOT alone cannot replace the benefits of platinum-grey coatings entirely but can be added to it. To take advantage of the impressive electrochemical and biological benefits of PEDOT and the outstanding electrochemical and mechanical endurance of platinum grey the two films were stacked and together with diazonium salt created a hybrid coating that combines the best of both worlds. The complex intertwined porosity of platinum grey entraps and houses the PEDOT molecules that are coated into its microporous geometry.

This mechanical bond was strengthened by electrografting a chemical adhesion promoter called diazonium salt.

If the applied charge during electroplating of PEDOT on a given platinum electrode site with a diameter of 200μm is near the amount necessary to coat 1μm PEDOT, but instead applied on a site previously coated with 8μm Pt-Grey, no noticeable thickness is added to the overall coating composition. That is due to the integration of PEDOT molecules inside the vacancies of microporous geometry of Pt-Grey (See Fig. 43-a). If the amount of charge being electroplated is more than this vacant volume of the given platinum-grey film the overall PEDOT film starts to elevate above the surface of platinum grey and increase the overall thickness of the composite.

Finally, we hypothesize that implanting visual cortical prosthetic devices in to the brains of patients that are going through degenerative loss of sight (before they go completely blind) may help them in preventing the progression of their blindness while they can still adapt to their bionic eye with the remaining vision they may still have before they go completely blind. This approach if shown promising can create a new path in the utilization and adoption of visual prosthetic devices.

4.5 Conclusion

In this chapter, we introduce a novel thin film composition that takes advantage of two promising technologies and introduces the best of two worlds for enhancing microelectrode arrays used in chronic neural stimulation. One is the most investigated and known conductive polymer known as PEDOT adhesion promoter called diazonium salt and the other is platinum grey which is the key coating material used in The Argus and Orion devices. PEDOT not only enhances the cellular agreement, promotes their growth and can carry various immunosuppressant drugs but can also enhance electrical properties that surpass some of the best conventional inorganic coatings. However, their polymeric molecules do not stick well to their underlying substrates and this causes immense bottleneck in their long-term endurance. Few investigators have reported chemical approaches and partially improved PEDOT adhesion on some inorganic materials (Reference?). This report shows that if PEDOT is electroplated on platinum grey that were previously treated in diazonium salt it can endure 24/7 continuous electrical stimulation in PBS for more than 100 days without showing noticeable decline in its improved electrical properties (>2X better than Pt-Grey-alone). These upgrades are critical in designing the next generation of ultra-small and highly dense electrode arrays comprising hundreds or thousands of channels.

4.6 Future Directions

The increase in charge storage capacity with supreme adhesion using PEDOT and Pt-Grey is indeed imperative in taking the delivery of bionic vision using flexible microelectrodes to the next level. However there are numerous challenges ahead that must be taken into account while thinking to resolve the issues surrounding the introduction of external implantable electrodes to the brain. Those include immune responses by the tissue that could be regulated and inhibited using various pharmaceutical approaches integrated with more sophisticated material composition on the electrode site to make them less and less invasive and agreeable with their surrounding brain tissue.

Also, as the electrodes become softer and thinner with higher densities it is a challenge to insert such electrodes into the brain while they have lower stiffness than the brain tissue itself. Many strategies are yet to get fine-tuned before these insertion strategies and surgical techniques become conventional and bullet-proof.

APPENDIX

APPENDIX

The Matlab code that was written originally in this thesis to take multiple datasets of impedance values of the reader coil corresponding to distinct eye pressures named as '*Eye_Graphing.m*'.

```
clc
clear all
close all

%>Go to csv folder --Need to make sure in same folder as .m file
    cd csv
%>Save all .csv into struct
    files = dir('*.csv');
%>Gets the length of the struct
    numfiles = length(files);
%>Creating an empty array for the for loop
    myfiles = cell(1,numfiles);
%>Creating a table for storing the min frequencies for each fit-method
    sample = zeros(6,(numfiles));
    rowNames =
    {'Poly7(Row1)','Fourier2(Row2)','Fourier3(Row3)','Spline(Row4)','Gaussian2(Row5)','Be
    stRowForFile'};
    fitsdata = [1 2 3 4 5];
    fits = num2cell(fitsdata);
    C = strings(1,numfiles);
    for g = [1:numfiles]
        C(1,g) = sprintf('File%d',g);
    end
    colNames = cellstr(C);
    MinPhaseFreqsMHz = array2table(sample,'RowNames',rowNames,'VariableNames',colNames);

%>Creating a table for storing error info for each fit-method
    rowNames =
    {'Poly7Error','Fourier2Error','Fourier3Error','SplineError','GaussianError'};
    C = strings(1,numfiles);
    V = strings(1,numfiles);
    for g = [1:numfiles]
        C(1,g) = sprintf('File%d',g);
        V(1,g) = 'string';
    end
    colNames = cellstr(C);
    vartype = cellstr(V);
    ErrorReport = table('size',[5
    numfiles],'VariableTypes',vartype,'RowNames',rowNames,'VariableNames',colNames);

    %>The for loop for creating all phase plots vs frequencies
for k = 1:numfiles
%Setup Data Table
    %>String to store file name from struct
    myfilename = sprintf(files(k).name);
    %>Retrieves file data from selected csv
    opts = detectImportOptions(myfilename);
    %>Stores data into table
    T = readtable(myfilename,opts);

%>Creating the graph of frequency vs phase (ignores amplitude)
    %>Setting up the data
    X = T{:,1}; %Frequency in Mhz
    Y = T{:,3}; %Phase in degrees

    %>High res vector for final freq identification
    HFV = min(X):.0001:max(X);

    %>Using the polonimal trace fit
    [poly,gofPol] = fit(X,Y,'poly7');

    %>Using Fourier
    [fourier2,gofF2] = fit(X,Y,'fourier2');
    [fourier3,gofF3] = fit(X,Y,'fourier3');

    %>Smoothing Spline (Can set SmoothingParam anywhere between 1-0, lower
```

```
63      %# is smoother)
64      [spline,gofSpl] = fit(X,Y,'smoothingspline','SmoothingParam',0.001);
65
66      %>Gaussian
67      [Gauss,gofG] = fit(X,Y,'gauss2');
68
69  %>Creating the scatter plot and trendline for this file,
70      F1 = figure('rend','painters','pos',[10 10 900 600]);
71      scatter(X,Y);
72      hold on
73
74      plot(poly,'b'); %Plotting Polyfit-Trendline
75      plot(fourier2,'r'); %Plotting Fourier2
76      plot(fourier3,'k'); %Plotting Fourier3
77      plot(spline,'m'); %Plotting Spline
78      plot(Gauss,'g'); %plotting Gaussian
79
80      hold off
81      L = legend('Phase Points','Poly 7 fit','Fourier 2','Fourier 3','Spline','Gaussian');
82      %>Beautification (labeling axis and titles and such)
83      xticks([min(X):35:max(X)]);
84      yticks([(min(Y)-10):0.25:(max(Y)+10)]) %Y-val for trendline
85      %yticks([(min(dPE)-10):0.25:(max(dPE)+10)]) %Y-val for derivative
86      grid on
87      %>Titles it the csv file's name
88      set(F1, 'NumberTitle', 'off','Name', sprintf('Date: %s', myfilename));
89      title('Phase Vs Frequency');
90      xlabel("Frequency(MHz)");
91      ylabel("Phase(Degrees)");
92
93  %>For Error Comparison
94      %>Sum of Squares Due to Error, we want to be close to 0
95      a = [gofPol.sse gofF2.sse gofF3.sse gofSpl.sse gofG.sse];
96      index = a==min(a);
97      bestfit1 = fits(index);
98      %>Adjusted R-Squared, uses R-squared with degree of freedom for more accuracy, want
        to be close to 1 [between 0-1]
99      b = [gofPol.adjrsquare gofF2.adjrsquare gofF3.adjrsquare gofSpl.adjrsquare
        gofG.adjrsquare];
100     index = b==max(b);
101     bestfit2 = fits(index);
102     %>Root Mean Squared, want to be 0
103     c = [gofPol.rmse gofF2.rmse gofF3.rmse gofSpl.rmse gofG.rmse];
104     index = c==min(c);
105     bestfit3 = fits(index);
106
107     if isequal(bestfit1, bestfit2) || isequal(bestfit3, bestfit2)
108         MinPhaseFreqsMHz(6,k) = {bestfit2{1}};
109     elseif isequal(bestfit1, bestfit3)
110         MinPhaseFreqsMHz(6,k) = {bestfit1{1}};
111     else
112         result = strcat(num2str(bestfit1{1}),num2str(bestfit2{1}),num2str(bestfit3{1}));
113         result = str2num(result);
114         MinPhaseFreqsMHz(6,k) = {result};
115     end
116
117     ErrorReport(1,k) = {sprintf('SSE:%.4d;ARS:%.4d;RMS:%.4d',a(1),b(1),c(1))};
118     ErrorReport(2,k) = {sprintf('SSE:%.4d;ARS:%.4d;RMS:%.4d',a(2),b(2),c(2))};
119     ErrorReport(3,k) = {sprintf('SSE:%.4d;ARS:%.4d;RMS:%.4d',a(3),b(3),c(3))};
120     ErrorReport(4,k) = {sprintf('SSE:%.4d;ARS:%.4d;RMS:%.4d',a(4),b(4),c(4))};
121     ErrorReport(5,k) = {sprintf('SSE:%.4d;ARS:%.4d;RMS:%.4d',a(5),b(5),c(5))};
122
123 %>Getting the frequency of the min phase
124     %poly
125     y = feval(poly,HFV);
126     index = y==min(y);
```

```
127         MinPhaseFreqsMHz(1,k) = {HFV(index)};
128         %fourier2
129         y = feval(fourier2,HFV);
130         index = y==min(y);
131         MinPhaseFreqsMHz(2,k) = {HFV(index)};
132         %fourier3
133         y = feval(fourier3,HFV);
134         index = y==min(y);
135         MinPhaseFreqsMHz(3,k) = {HFV(index)};
136         %spline
137         y = feval(spline,HFV);
138         index = y==min(y);
139         MinPhaseFreqsMHz(4,k) = {HFV(index)};
140         %gauss
141         y = feval(Gauss,HFV);
142         index = y==min(y);
143         MinPhaseFreqsMHz(5,k) = {HFV(index)};
144
145     %return %Uncomment to only run once
146     end
147     %>Displays the phase min associated frequencies
148         MinPhaseFreqsMHz
149         ErrorReport
150
151     %Return address --where .m file was before jumping into csv file
152     cd 'C:\Users\ryant\Desktop\Classes and Clubs\Profesional\uTech_Lab\Eye Impedance
        Project\Functional'
153
154
```

BIBLIOGRAPHY

BIBLIOGRAPHY

[1] Scott AW, Bressler NM, Ffolkes S, Wittenborn JS, Jorkasky J. Public attitudes about eye and vision health. JAMA ophthalmology. 2016 Oct 1;134(10):1111-8.

[2] Merepa SS, et al. Socioeconomic Influence of Glaucoma on Patients. EC Ophthalmology 9.1. 2018: 03-09

[3] Bourne RR, Flaxman SR, Braithwaite T, Cicinelli MV, Das A, Jonas JB, Keeffe J, Kempen JH, Leasher J, Limburg H, Naidoo K. Magnitude, temporal trends, and projections of the global prevalence of blindness and distance and near vision impairment: a systematic review and meta-analysis. The Lancet Global Health. 2017 Sep 1;5(9):e888-97.

[4] World Health Organization. Catalogue of key eye health indicators in the African Region, 2017.

[5] Hommer A. Managing Primary Open-angle Glaucoma–Ocular Tolerability, Compliance, Persistence and Patient Outcomes. Eur Ophthalmic Rev. 2009;3:19-22.

[6] Kass MA, Heuer DK, Higginbotham EJ, Johnson CA, Keltner JL, Miller JP, Parrish RK, Wilson MR, Gordon MO. The Ocular Hypertension Treatment Study: a randomized trial determines that topical ocular hypotensive medication delays or prevents the onset of primary open-angle glaucoma. Archives of ophthalmology. 2002 Jun 1;120(6):701-13.

[7] Samples JR, Knepper PA, editors. Glaucoma Research and Clinical Advances: 2018 to 2020. Kugler Publications; 2018 Apr 24.

[8] Overby DR, Stamer WD, Johnson M. The changing paradigm of outflow resistance generation: towards synergistic models of the JCT and inner wall endothelium. Experimental eye research. 2009 Apr 30;88(4):656-70.

[9] Vranka JA, Kelley MJ, Acott TS, Keller KE. Extracellular matrix in the trabecular meshwork: Intraocular pressure regulation and dysregulation in glaucoma.

[10] Van Buskirk EM. Trabeculotomy in the immature, enucleated human eye. Invest Ophthalmol Vis Sci 1977;16(1):63-66.

[11] Minckler DS, Baerveldt G, Alfaro MR, Francis BA. Clinical results with the trabectome for treatment of open-angle glaucoma. Ophthalmology 2005;112(6):962-967.

[12] Tamm S, Tamm E, Rohen JW. Age-related changes of the human ciliary muscle. A quantitative morphometric study. Mech Ageing Dev 1992;62(2):209-221.

[13] Gabelt BT, Gottanka J, Lütjen-Drecoll E, Kaufman PL. Aqueous humor dynamics and trabecular meshwork and anterior ciliary muscle morphologic changes with age in rhesus monkeys. Invest Ophthalmol Vis Sci 2003;44(5):2118-2125.

[14] Bill A. Effects of atropine and pilocarpine on aqueous humour dynamics in cynomolgus monkeys (macaca irus). Exp Eye Res 1967;6(2):120-125.

[15] https://emedicine.medscape.com/article/1207470-overview

[16] Hommer A. Managing Primary Open-angle Glaucoma–Ocular Tolerability, Compliance, Persistence and Patient Outcomes. Eur Ophthalmic Rev. 2009;3:19-22.
[17] Maier PC, Funk J, Schwarzer G, Antes G, Falck-Ytter YT. Treatment of ocular hypertension and open angle glaucoma: meta-analysis of randomised controlled trials. bmj. 2005 Jul 14;331(7509):134.

[18] Kass MA, Heuer DK, Higginbotham EJ, Johnson CA, Keltner JL, Miller JP, Parrish RK, Wilson MR, Gordon MO. The Ocular Hypertension Treatment Study: a randomized trial determines that topical ocular hypotensive medication delays or prevents the onset of primary open-angle glaucoma. Archives of ophthalmology. 2002 Jun 1;120(6):701-13.

[19] https://nei.nih.gov/content/nei-funded-researchers-identify-133-genetic-variants-predict-glaucoma-risk

[20] https://villa-medica.com/glaucoma-sneak-thief-sight/

[21] https://ghr.nlm.nih.gov/gene/MYOC#normalfunction

[22] Souzeau E, Burdon KP, Dubowsky A, Grist S, Usher B, Fitzgerald JT, Crawford A, Hewitt AW, Goldberg I, Mills RA, Ruddle JB. Higher prevalence of myocilin mutations in advanced glaucoma in comparison with less advanced disease in an Australasian disease registry. Ophthalmology. 2013 Jun 1;120(6):1135-43.

[23] http://www.stoneoakeyes.com/

[24] Goldmann HA, Schmidt TH. Über applanationstonometrie. Ophthalmologica. 1957;134(4):221-42.

[25] https://www.glaucoma.org/glaucoma/the-importance-of-corneal-thickness.php

[26] https://santafazsalud.com/project/tonometria

[27] Voskanyan L, García-Feijoó J, Belda JI, Fea A, Jünemann A, Baudouin C. Prospective, unmasked evaluation of the iStent® inject system for open-angle glaucoma: synergy trial. Advances in therapy. 2014 Feb 1;31(2):189-201.

[28] Bäcklund Y, Rosengren L, Hök B, Svedbergh B. Passive silicon transensor intended for biomedical, remote pressure monitoring. Sensors and Actuators A: Physical. 1990 Feb 1;21(1-3):58-61.

[29] Stangel K, Kolnsberg S, Hammerschmidt D, Hosticka BJ, Trieu HK, Mokwa W. A programmable intraocular CMOS pressure sensor system implant. IEEE Journal of Solid-State Circuits. 2001 Jul;36(7):1094-100.

[30] Chen PJ, Rodger DC, Agrawal R, Saati S, Meng E, Varma R, Humayun MS, Tai YC. Implantable micromechanical parylene-based pressure sensors for unpowered intraocular pressure sensing. Journal of Micromechanics and Microengineering. 2007 Aug 31;17(10):1931.

[31] Lee JO, Park H, Chen O, Balakrishna A, Du J, Sretavan DW, Choo H. Achieving clinically viable 12-CM readout distance from micromachined implantable intraocular pressure sensor using a standard clinical slit lamp. InMicro Electro Mechanical Systems (MEMS), 2016 IEEE 29th International Conference on 2016 Jan 24 (pp. 210-213). IEEE.

[32] Croft MA, Heatley G, McDonald JP, Katz A, Kaufman PL. Accommodative movements of the lens/capsule and the strand that extends between the posterior vitreous zonule insertion zone & the lens equator, in relation to the vitreous face and aging. Ophthalmic and Physiological Optics. 2016 Jan;36(1):21-32.

[33] Fernandes J, Kwon YH, Kim JJ, Liu H, Jiang H. High Contrast Grating Based Strain Sensor for Intraocular Applications. Journal of Microelectromechanical Systems. 2018 May 18.

[34] Chen PJ, Rodger DC, Saati S, Humayun MS, Tai YC. Microfabricated implantable parylene-based wireless passive intraocular pressure sensors. Journal of Microelectromechanical Systems. 2008 Dec;17(6):1342-51.

[35] Chen PJ, Saati S, Varma R, Humayun MS, Tai YC. Wireless intraocular pressure sensing using microfabricated minimally invasive flexible-coiled LC sensor implant. Journal of Microelectromechanical Systems. 2010 Aug;19(4):721-34.

[36] Chen G, Ghaed H, Haque RU, Wieckowski M, Kim Y, Kim G, Fick D, Kim D, Seok M, Wise K, Blaauw D. A cubic-millimeter energy-autonomous wireless intraocular pressure monitor. InSolid-State Circuits Conference Digest of Technical Papers (ISSCC), 2011 IEEE International 2011 Feb 20 (pp. 310-312). IEEE.

[37] Ha D, de Vries WN, John SW, Irazoqui PP, Chappell WJ. Polymer-based miniature flexible capacitive pressure sensor for intraocular pressure (IOP) monitoring inside a rat eye. Biomedical microdevices. 2012 Feb 1;14(1):207-15.

[38] Crum B, Li W. Parylene-based fold-and-bond wireless pressure sensor. InNano/Micro Engineered and Molecular Systems (NEMS), 2013 8th IEEE International Conference on 2013 Apr 7 (pp. 1155-1158). IEEE.

[39] Varel Ç, Shih YC, Otis BP, Shen TS, Böhringer KF. A wireless intraocular pressure monitoring device with a solder-filled microchannel antenna. Journal of Micromechanics and Microengineering. 2014 Mar 13;24(4):045012.

[40] Chitnis G, Maleki T, Samuels B, Cantor LB, Ziaie B. A minimally invasive implantable wireless pressure sensor for continuous IOP monitoring. IEEE Transactions on Biomedical Engineering. 2013 Jan;60(1):250-6.

[41] Agarwal A, Shapero A, Rodger D, Humayun M, Tai YC, Emami A. A wireless, low-drift, implantable intraocular pressure sensor with parylene-on-oil encapsulation. InCustom Integrated Circuits Conference (CICC), 2018 IEEE 2018 Apr 8 (pp. 1-4). IEEE.

[42] Koutsonas A, Walter P, Roessler G, Plange N. Implantation of a novel telemetric intraocular pressure sensor in patients with glaucoma (ARGOS study): 1-year results. Investigative ophthalmology & visual science. 2015 Feb 1;56(2):1063-9.

[43] Greene ME, Gilman BG. Intraocular pressure measurement with instrumented contact lenses. Investigative ophthalmology & visual science. 1974 Apr 1;13(4):299-302.

[44] Laukhin V, Sánchez I, Moya A, Laukhina E, Martin R, Ussa F, Rovira C, Guimera A, Villa R, Aguiló J, Pastor JC. Non-invasive intraocular pressure monitoring with a contact lens engineered with a nanostructured polymeric sensing film. Sensors and Actuators A: Physical. 2011 Nov 1;170(1-2):36-43.

[45] Tseng CK, Huang YC, Tsai SW, Yeh GT, Chang CH, Chiou JC. Design and fabricate a contact lens sensor with a micro-inductor embedded for intraocular pressure monitoring. InSensors, 2012 IEEE 2012 Oct 28 (pp. 1-4). IEEE.

[46] Chiou JC, Hsu SH, Huang YC, Yeh GT, Liou WT, Kuei CK. A wirelessly powered smart contact lens with reconfigurable wide range and tunable sensitivity sensor readout circuitry. Sensors. 2017 Jan 7;17(1):108.

[47] Vitish-Sharma P, Acheson AG, Stead R, Sharp J, Abbas A, Hovan M, Maxwell-Armstrong C, Guo B, King AJ. Can the SENSIMED Triggerfish® lens data be used as an accurate measure of intraocular pressure?. Acta ophthalmologica. 2018 Mar;96(2):e242-6.

[48] Madi F. Neuroprotective Effect of Intraocular BDNF and Optogenetic Stimulation of Visual Cortex on Retinal Ganglion Cell Survival and Function in the Rat following Optic Nerve Injury. Michigan State University; 2018.

[49] G. Nagel, T. Szellas, W. Huhn, S. Kateriya, N. Adeishvili, P. Berthold, D. Ollig, P. Hegemann and E. Bamberg, "Channelrhodopsin-2, a directly light-gated cation-selective membrane channel," in *Proceedings of the National Academy of Sciences*, 2003, vol. 100, no. 24, pp. 13940-13945.

[50] B. Schobert, J. K. Lanyi, "Halorhodopsin is a light-driven chloride pump," in *Journal of Biological Chemistry*, 1982, vol. 257, no. 17, pp. 10306-10313.

[51] B. Y. Chow, X. Han, A. S Dobry, X. Qian, A. S. Chuong, M. Li, M. A. Henninger, G. M. Belfort, Y. Lin, P. E. Monahan, E. S. Boyden, "High-performance genetically targetable optical neural silencing by light-driven proton pumps," in *Nature*, 2010, vol. 463, no. 7277, pp. 98.

[52] E. S. Boyden, F. Zhang, E. Bamberg, G. Nagel, K. Deisseroth, "Millisecond-timescale, genetically targeted optical control of neural activity", in *Nature Neuroscience*, 2005, vol. 8, no. 9, pp. 1263-1268.

[53] F. Zhang, L. P. Wang, S. S. Boyden, K. Deisseroth, "Channelrhodopsin-2 and optical control of excitable cells," in *Nature Methods*, 2006, vol. 3, no. 10, pp. 785-792.

[54] X. Han, E. S. Boyden, "Multiple-color optical activation, silencing, and desynchronization of neural activity, with single-spike temporal resolution," in *PLOS ONE*, 2007, vol. 2, no. 3 pp. e299.

[55] J. G. Mccall, R. Qazi, G. Shin, S. Li, M. H. Ikram, K. I. Jang, Y. Liu, R. Al-Hasani, M. R. Bruchas, J. W. Jeong, J. A. Rogers, "Preparation and implementation of optofluidic neural probes for in vivo wireless pharmacology and optogenetics," in *Nature Protocol,* 2017, vol. 12, no. 2, pp. 219-237.

[56] M. Yuan, S. Yue, Y. Zhang, S. Wang "Wirelessly controlled optical stimulator for optogenetics application," in *International Conference on Biomedical Image and Signal Processing*, 2015, Beijing, China.

[57] C. T. Wentz, J. G. Bernstein, P. Monahan, A. Guerra, A. Rodriguez, E. S. Boyden, "A wirelessly powered and controlled device for optical neural control of freely-behaving animals", in *Journal of Neural Engineering*, 2011, vol. 8, no. 4, pp. 046021.

[58] M. A. Rossi, V. Go, T. Murphy, Q. Fu, J. Morizio, H. H. Yin "A wirelessly controlled implantable LED system for deep brain optogenetic stimulation," in *Frontiers in Integrative Neuroscience* 2015, vol. 9, pp. 8.

[59] K. I. Song, S. E. Park, M. S. Kim, C. Joo, Y. J. Kim, J. K. F. Su, I. Youn, "An implantable wireless optogenetic stimulation system for peripheral nerve control," in *Engineering in Medicine and Biology Society*, 2015 37th Annual International Conference of the IEEE, pp. 1033-1036.

[60] K. L. Montgomery, A. J. Yeh, J. S. Ho, V. Tsao, S. M. Lyer, L. Grosenick, E. A. Ferenczi, Y. Tanabe, K. Deisseroth, S. L. Delp, A. S. Poon "Wirelessly Powered, fully internal optogenetics for brain, spinal and peripheral circuits in mice," in *Nature Methods*, 2015, vol. 12, no. 10, pp. 969-974.

[61] D. I. McRee, H. Watchtel, 'Pulse Microwave effects on nerve vitality," in *Radiation Research*, 1982, vol. 91, no. 1, pp. 212-218.

[62] F. Wu, E. Stark, P. C. Ku, K. D. Wise, G. Buzsaki, E. Yoon, "Monolithically integrated μLEDs on silicon neural probes for high-resolution optogenetic studies in behaving animals," in *Neuron*, Dec. 2015, vol. 88, no. 6, pp. 1136-1148.

[63] Hartong DT, Berson EL, Dryja TP. Retinitis pigmentosa. The Lancet. 2006 Nov 18;368(9549):1795-809.

[64] da Cruz L, Dorn JD, Humayun MS, Dagnelie G, Handa J, Barale PO, Sahel JA, Stanga PE, Hafezi F, Safran AB, Salzmann J. Five-year safety and performance results from the Argus II retinal prosthesis system clinical trial. Ophthalmology. 2016 Oct 1;123(10):2248-54.

[65] https://www.retina-implant.de/en/

[66] Edwards TL, Cottriall CL, Xue K, Simunovic MP, Ramsden JD, Zrenner E, MacLaren RE. Assessment of the Electronic Retinal Implant Alpha AMS in Restoring Vision to Blind Patients with End-Stage Retinitis Pigmentosa. Ophthalmology. 2018 Mar 1;125(3):432-43.

[67] Lorach H, Goetz G, Mandel Y, Lei X, Kamins TI, Mathieson K, Huie P, Dalal R, Harris JS, Palanker D. Performance of photovoltaic arrays in-vivo and characteristics of prosthetic vision in animals with retinal degeneration. Vision research. 2015 Jun 1;111:142-8.

[68] Shannon RV. A model of safe levels for electrical stimulation. IEEE Transactions on Biomedical Engineering. 1992 Apr;39(4):424-6.

[69] Ayton LN, Blamey PJ, Guymer RH, Luu CD, Nayagam DA, Sinclair NC, Shivdasani MN, Yeoh J, McCombe MF, Briggs RJ, Opie NL. First-in-human trial of a novel suprachoroidal retinal prosthesis. PloS one. 2014 Dec 18;9(12):e115239.

[70] Fujikado T, Kamei M, Sakaguchi H, Kanda H, Endo T, Hirota M, Morimoto T, Nishida K, Kishima H, Terasawa Y, Oosawa K. One-year outcome of 49-channel suprachoroidal–transretinal stimulation prosthesis in patients with advanced retinitis pigmentosa. Investigative ophthalmology & visual science. 2016 Nov 1;57(14):6147-57.

[71] Gidon A, Zolnik TA, Fidzinski P, Bolduan F, Papoutsi A, Poirazi P, Holtkamp M, Vida I, Larkum ME. Dendritic action potentials and computation in human layer 2/3 cortical neurons. Science. 2020 Jan 3;367(6473):83-7.

[72] Chhin D, Polcari D, Bodart-Le Guen C, Tomasello G, Cicoira F, Schougaard SB. Diazonium-Based Anchoring of PEDOT on Pt/Ir Electrodes via Diazonium Chemistry. Journal of The Electrochemical Society. 2018 Jan 1;165(12):G3066-70.

[73] Zeng W, Zheng F, Li R, Zhan Y, Li Y, Liu J. Template synthesis of SnO 2/α-Fe 2 O 3 nanotube array for 3D lithium ion battery anode with large areal capacity. Nanoscale. 2012;4(8):2760-5.

[74] Jiang S, Shi T, Gao Y, Long H, Xi S, Tang Z. Fabrication of a 3D micro/nano dual-scale carbon array and its demonstration as the microelectrodes for supercapacitors. Journal of Micromechanics and Microengineering. 2014 Mar 10;24(4):045001.

[75] Hussain G, O'Mullane AP, Silvester DS. Modification of microelectrode arrays with high surface area dendritic platinum 3D structures: enhanced sensitivity for oxygen detection in ionic liquids. Nanomaterials. 2018 Sep;8(9):735.

[76] Hussain G, Aldous L, Silvester DS. Preparation of platinum-based'cauliflower microarrays' for enhanced ammonia gas sensing. Analytica Chimica Acta. 2019 Feb 7;1048:12-21.

[77] Hay CE, Lee J, Silvester DS. Formation of 3-dimensional gold, copper and palladium microelectrode arrays for enhanced electrochemical sensing applications. Nanomaterials. 2019 Aug;9(8):1170.

[78] Silvester DS. New innovations in ionic liquid–based miniaturised amperometric gas sensors. Current Opinion in Electrochemistry. 2019 Jun 1;15:7-17.

[79] Yu L, Liu J, Yin W, Yu J, Chen R, Song D, Liu Q, Li R, Wang J. Ionic liquid combined with NiCo2O4/rGO enhances electrochemical oxygen sensing. Talanta. 2020 Mar 1;209:120515.

[80] Kouhani MH, Weber A, Li W. Wireless intraocular pressure sensor using stretchable variable inductor. In MEMS, 2017 IEEE 30th International Conference on 2017 Jan 22 (pp. 557-560). IEEE.

[81] Núñez CG, Manjakkal L, Dahiya R. Energy autonomous electronic skin. npj Flexible Electronics. 2019 Jan 4;3(1):1.

[82] Chen PY, Sakhdari M, Hajizadegan M, Cui Q, Cheng MM, El-Ganainy R, Alù A. Generalized parity–time symmetry condition for enhanced sensor telemetry. Nature Electronics. 2018 May;1(5):297.

[83] Kim J, Kim M, Lee MS, Kim K, Ji S, Kim YT, Park J, Na K, Bae KH, Kim HK, Bien F. Wearable smart sensor systems integrated on soft contact lenses for wireless ocular diagnostics. Nature communications. 2017 Apr 27;8:14997.

[84] Chen LY, Tee BC, Chortos AL, Schwartz G, Tse V, Lipomi DJ, Wong HS, McConnell MV, Bao Z. Continuous wireless pressure monitoring and mapping with ultra-small passive sensors for health monitoring and critical care. Nature communications. 2014 Oct 6;5:5028.

[85] Cao H, Weber RJ, Hamouche NG. A passive intraocular pressure sensor and a wireless sensing technique using an intermediate LC resonator. InLife Science Systems and Applications Workshop (LiSSA), 2011 IEEE/NIH 2011 Apr 7 (pp. 5-8). IEEE.

[86] Rosa EB, Grover FW. Formulas and tables for the calculation of mutual and self inductance.(Revised.). Journal of the Washington Academy of Sciences. 1911 Jul 19;1(1/2):14-6.

[87] https://www.doitpoms.ac.uk/tlplib/beam_bending/bend_moments.php [Accessed: 15-Mar-2019].

[88] Parylene.com, 'Para Tech Parylene Properties.' Available: https://goo.gl/qb7gvR [Accessed: 23-Jan- 2019].

[89] Shin SR, Farzad R, Tamayol A, Manoharan V, Mostafalu P, Zhang YS, Akbari M, Jung SM, Kim D, Comotto M, Annabi N. A Bioactive Carbon Nanotube-Based Ink for Printing 2D and 3D Flexible Electronics. Advanced Materials. 2016 May;28(17):3280-9.

[90] Bao K, Chen D, Shi Q, Liu L, Chen J, Li J, Wang J. A readout circuit for wireless passive LC sensors and its application for gastrointestinal monitoring. Measurement Science and Technology. 2014 Jul 8;25(8):085104.

[91] Pallikaris IG, Dastiridou AI, Tsilimbaris MK, Karyotakis NG, Ginis HS. Ocular rigidity. Expert Review of Ophthalmology. 2010 Jun 1;5(3):343-51.

[92] Alhamad TA, Meek KM. Comparison of factors that influence the measurement of corneal hysteresis in vivo and in vitro. Acta ophthalmologica. 2011 Aug;89(5):e443-50.

[93] Elsheikh A, Alhasso D, Rama P. Biomechanical properties of human and porcine corneas. Experimental eye research. 2008 May 1;86(5):783-90.

[94] Achyuthan KE, Sawyer PS, Mata G, Ii GV, Bernstein R. Parylene C aging studies. no. September. 2014 Sep 1.

[95] K. Y. Kwon, B. Sirowatka, A. Weber, W. Li, "A hybrid neural interface with transparent μECoG electrode array and integrated LEDs for optogenetics." in *IEEE transactions on biomedical circuits and systems,* 2013, vol. 7, no. 5, pp. 593-600.

[96] C. Hassler, R.P. von Metzen, P. Ruther, T. Stieglitz, "Characterization of parylene C as an encapsulation material for implanted neural prostheses" in *Biomedical Materials Research Part B: Applied Biomaterial,* 2010, vol. 93, no. 1, pp. 266-274.

[97] Scscoatings.com, 'SCS Parylene Properties.' Available: http://goo.gl/NNihZx [Accessed: 17-Apr- 2018].

[98] Simblee.com, 'Simblee_Quickstart_Guide_v1.0' Available: goo.gl/iGgDor [Accessed: 15- Feb- 2018].

[99] P. D. Wolf, "Thermal considerations for the design of an implanted cortical brain–machine interface (BMI)," in *Indwelling Neural Implants: Strategies for Contending with the In Vivo Environment,* 2008, pp. 33-38.

[100] A. M. Aravanis, L. P. Wang, F. Zhang, L. A. Meltzer, M. Z. Mogri, M. B. Schneider, K. Deisseroth, "An optical neural interface: in vivo control of rodent motor cortex with integrated fiberoptic and optogenetic technology," in *Journal of neural engineering*, 2007, vol. 4, no. 3, pp. S143.

[101] Negi, Sandeep, Rajmohan Bhandari, and Florian Solzbacher. "A novel technique for increasing charge injection capacity of neural electrodes for efficacious and safe neural stimulation." 2012 Annual International Conference of the IEEE Engineering in Medicine and Biology Society. IEEE, 2012.

[102] Weremfo, Alexander, et al. "Investigating the interfacial properties of electrochemically roughened platinum electrodes for neural stimulation." Langmuir 31.8 (2015): 2593-2599.

[103] Leber, M., et al. "Long term performance of porous platinum coated neural electrodes." Biomedical microdevices 19.3 (2017): 62.

[104] Puttaswamy, Srinivasu Valagerahally, et al. "Nanowire Electrodes Integrated on Tip of Microwire for Peripheral Nerve Stimulation." Journal of Microelectromechanical Systems 26.4 (2017): 921-925.

[105] Richardson-Burns, Sarah M., et al. "Polymerization of the conducting polymer poly (3, 4-ethylenedioxythiophene)(PEDOT) around living neural cells." Biomaterials 28.8 (2007): 1539-1552.

[106] Kung TA, Langhals NB, Martin DC, Johnson PJ, Cederna PS, Urbanchek MG. Regenerative peripheral nerve interface viability and signal transduction with an implanted electrode. Plastic and reconstructive surgery. 2014 Jun 1;133(6):1380-94.

[107] Cui XT, Zhou DD. Poly (3, 4-ethylenedioxythiophene) for chronic neural stimulation. IEEE Transactions on Neural Systems and Rehabilitation Engineering. 2007 Dec 12;15(4):502-8.

[108] Khodagholy D, Doublet T, Quilichini P, Gurfinkel M, Leleux P, Ghestem A, Ismailova E, Hervé T, Sanaur S, Bernard C, Malliaras GG. In vivo recordings of brain activity using organic transistors. Nature communications. 2013 Mar 12;4(1):1-7.

[109] Cogan SF, Peramunage D, Smirnov A, Ehrlich J, Mccreery DB, Manoonkitiwongsa PS. Polyethylenedioxythiophene (PEDOT) coatings for neural stimulation and recording electrodes. Mater Res Soc Meet,(Abstr. QQ2. 7). 2007 Nov 26.

[110] Rose TL, Robblee LS. Electrical stimulation with Pt electrodes. VIII. Electrochemically safe charge injection limits with 0.2 ms pulses (neuronal application). IEEE Transactions on Biomedical Engineering. 1990 Nov;37(11):1118-20.

[111] Robblee LS, Mangaudis MJ, Lasinsky ED, Kimball AG, Brummer SB. Charge injection properties of thermally-prepared iridium oxide films. MRS Online Proceedings Library Archive. 1985;55.

[112] Weiland JD, Anderson DJ, Humayun MS. In vitro electrical properties for iridium oxide versus titanium nitride stimulating electrodes. IEEE transactions on biomedical engineering. 2002 Dec;49(12):1574-9.

[113] De la Oliva, Natàlia, Xavier Navarro, and Jaume del Valle. "Dexamethasone reduces the foreign body reaction to intraneural electrode implants in the peripheral nerve of the rat." The Anatomical Record 301.10 (2018): 1722-1733.

[114] Kim N, Petsagkourakis I, Chen S, Berggren M, Crispin X, Jonsson MP, Zozoulenko I. Electric Transport Properties in PEDOT Thin Films. Conjugated Polymers: Properties, Processing, and Applications. 2019 Mar 25.

[115] Bodart C, Rossetti N, Hagler JE, Chevreau P, Chhin D, Soavi F, Schougaard SB, Amzica F, Cicoira F. Electropolymerized Poly (3, 4-ethylenedioxythiophene)(PEDOT) Coatings for Implantable Deep-Brain-Stimulating Microelectrodes. ACS applied materials & interfaces. 2019 Apr 12;11(19):17226-33.

[116] Ouyang L, Wei B, Kuo CC, Pathak S, Farrell B, Martin DC. Enhanced PEDOT adhesion on solid substrates with electrografted P (EDOT-NH2). Science advances. 2017 Mar 1;3(3):e1600448.

[117] Villemin E, Lemarque B, Vũ TT, Nguyen VQ, Trippé-Allard G, Martin P, Lacaze PC, Lacroix JC. Improved adhesion of poly (3, 4-ethylenedioxythiophene)(PEDOT) thin film to solid substrates using electrografted promoters and application to efficient nanoplasmonic devices. Synthetic Metals. 2019 Feb 1;248:45-52.

[118] Qu J, Garabedian N, Burris DL, Martin DC. Durability of Poly (3, 4-ethylenedioxythiophene)(PEDOT) films on metallic substrates for bioelectronics and the dominant role of relative shear strength. Journal of the mechanical behavior of biomedical materials. 2019 Dec 1;100:103376.

[119] Zhou DD, Dorn JD, Greenberg RJ. The Argus® II retinal prosthesis system: An overview. In2013 IEEE International Conference on Multimedia and Expo Workshops (ICMEW) 2013 Jul 15 (pp. 1-6). IEEE.

[121] Pouratian N, Yoshor D, Niketeghad S, Dornm J, Greenberg R. Early Feasibility Study of a Neurostimulator to Create Artificial Vision. Neurosurgery. 2019 Sep 1;66(Supplement_1):nyz310_146.